Fluorescence-Enabled Electrochemical Microscopy and Nanoscale Electrochemical Analysis

Joshua Pierre Guerrette

A dissertation
submitted in partial fulfillment of the
requirements for the degree of

Doctor of Philosophy

University of Washington
2013

Reading Committee:
Bo Zhang, Chair
Daniel T. Chiu
Frantisek Turecek

Program Authorized to Offer Degree:
Chemistry

University of Washington

Abstract

Fluorescence-Enabled Electrochemical Microscopy
and Nanoscale Electrochemical Analysis

Joshua Pierre Guerrette

Chair of the Supervisory Committee:
Assistant Professor Bo Zhang
Department of Chemistry

This dissertation discusses the fundamental study of several electroanalytical chemistry tools and methods. Unifying factors between the various chapters include the use of nano and microscale materials for electrode fabrication and the extensive use of voltammetric techniques for substrate characterization. Chapter 1 briefly introduces the technique of voltammetry and describes its importance in electrode characterization. This is followed by a short discussion of the methods and tools presented in upcoming chapters. In chapter 2 we highlight the development of fluorescence-enabled electrochemical microscopy (FEEM) and demonstrate an application towards heterogeneous catalyst screening. The FEEM technique uses a closed bipolar electrode (BPE) or arrays of many BPEs to couple the oxidation of an ordinary redox analyte to the fluorogenic reduction of a special reporter

molecule. Optically monitoring the progress of the fluorogenic reaction allows for the indirect monitoring of the current through the BPE.

Due to the importance of closed BPEs in the development of FEEM a detailed fundamental study of these electrodes was conducted. This work, which introduces the theory and experimental description of closed BPEs and discusses the factors to consider when using these electrodes for chemical analysis is presented in chapters 3 and 4. Next in chapter 5 we discuss the fabrication and voltammetric response of gold nanotrench electrodes. This includes the development of an analytical expression to correlate the recess depth to the diffusion-limited electrochemical response of these electrodes. Computational simulations and experimental findings are used to validate the theoretical model. Finally chapter 6 presents the first experimental demonstration of the scan-rate dependence of the non-linear current-voltage response commonly observed in conical quartz nanopores. We explain this behavior in terms of the sluggish redistribution of ions in the vicinity of the nanopore mouth upon voltage changes.

TABLE OF CONTENTS

LIST OF FIGURES

LIST OF TABLES

ACKNOWLEDGEMENTS

I would like to express my gratitude to my research advisor, Dr. Bo Zhang for allowing me the opportunity to work in his group and for his valuable mentorship over the last few years. I am particularly grateful for his ability to keep me focused on the science yet somehow make me feel like I have had the freedom to play around with cool instruments and lasers all day long.

There are several members of the Zhang group who I wish to thank: Stephen Percival for his help on much of the work presented here in this dissertation. Stephen Oja for his assistance with the BPE study and during this time of transition. David Galvan for his work last summer fabricating nanowire arrays. To the past Zhang lab postdocs; Dr. Yongxin Li, Dr. Kelly Adams and Dr. Bikash Jena for your words of wisdom throughout my first year in the group.

I also owe my appreciation to the valuable insight provided by my supervisory committee members: Dr. Daniel Chiu, Dr. Lih Lin, Dr. Bruce Robinson and Dr. Frantisek Turecek. There are several additional faculty members and postdocs here at the University of Washington as well as the University of Hawai`i who have been influential and contributed to my success; most notably Dr. Thomas Hemscheidt and Dr. Benjamin Philmus for providing my first exposure to academic research and guidance throughout that process.

I am also thankful for the generous funding provided by: the American Chemical Society Division of Analytical Chemistry Graduate Fellowship, sponsored by the Society of Analytical Chemists of Pittsburgh; the Mindlin Graduate Student Fellowship and the Basil G. and Gretchen F. Anex Endowed Fellowship in Chemistry.

I would like to thank my parents, Pat and Diane, for their support in so many ways over the years and for teaching me the benefits of hard work. I also need to thank my parents-in-law, Jack and Joyce, for the motivation to not let them down. Now they can say their daughter married a doctor…of philosophy. Most of all I am grateful to my wife Jinger for the years of dedication, support and sacrifice that she has committed to me and my sometimes obsessive goals.

CHAPTER 1
Introduction

1.1 Introduction

Electroanalytical chemistry is a broad collection of analytical methods in which the properties of an analyte (i.e. identity, quantity, thermodynamic, kinetic) can be determined through the measurement of electrical current derived from charge transfer reactions.[1] One of the main classes of electroanalytical methods is voltammetry[2] in which the electric potential between two or more electrodes is controlled while the electrical current through the electrodes is measured. The potential can be held constant and the current recorded over time in the case of constant-potential chronoamperometry. Alternatively, the current can be measured as a function of a variable potential which is pulsed, stepped, continuously swept or cycled. Typically in this latter case the data is represented by a current-voltage (*i*-*V*) curve known as a voltammogram which provides much information about the electrochemical cell.

Introduced in 1942 by Hickling,[3] a potentiostat is the instrument traditionally used to control the voltage between the electrode of interest, called the working electrode and a second electrode with known properties, the reference electrode. When the current passed between two electrodes is high (>10μA) a significant portion of the applied potential may be lost across the solution in what is known as an iR_s drop, where R_s is the solution resistance between the electrodes. If this is the case often times a third (counter) electrode is used to pass the current required to balance the process under investigation at the working electrode. This three-electrode configuration is used to minimize the iR_s drop between the working and reference electrodes and ensure that the potential measured is truly representative for the

process of interest. One major advantage to using micro and nanoelectrodes for analysis is the passage of small currents, thus allowing for the use of the simpler two-electrode cell.[1]

1.2 Surface Characterization by Voltammetry

Voltammetric methods are also frequently utilized for the characterization of electroactive surfaces.[4] This data can be a useful supplement in the determination of working electrode geometries, such as radius of a disc-shaped electrode[5] or depth of electrode recess[6] or in a study of the electrocatalytic activity of modified electrode surfaces.[7] The voltammetric characterization of electrode geometries becomes particularly important with ultramicroelectrodes and nanoelectrodes. Due to the small critical dimension of these electrodes (< 10 μm) it is difficult or impossible to obtain satisfactory optical images using conventional mean. Electron microscopy is often used in such cases however destructive sample preparation processes or the need for characterization of several electrodes, before and after various fabrication/modification steps becomes unfeasible or prohibitively costly. In such cases a quick cyclic voltammetric experiment in a standard solution may provide an acceptable level of characterization. Throughout much of this dissertation data obtained through voltammetry is used in conjunction with analytically derived models and/or computational simulations to characterize electrode surfaces.

1.3 Electrochemical Imaging

Electrochemical imaging techniques have emerged as useful tools for many analytical investigations in the past few decades. The most widely applied of these methods is scanning electrochemical microscopy (SECM) developed in the late 1980s by Bard and coworkers at the University of Texas.[8] With SECM an ultramicroelectrode or nanoelectrode is rastered

over the substrate of interest to obtain conductivity or electrochemical information. Applications of this technique have included probing the reactivity and properties of an electrode,[9] mapping a surface for catalytic activity[10,11] and imaging the functionality of single neuronal cells.[12] Due to the tremendous impact SECM and other electrochemical imaging techniques have had on the field of electroanalysis we believe it is important to continually advance these existing technologies and to develop new ones having valuable and interesting advantages of their own.

In chapter 2 we discuss the use of fluorescence microscopy and closed bipolar electrodes to reveal electrochemical and electrocatalytic activity on large electrochemical arrays. We demonstrate fluorescence-enabled electrochemical microscopy (FEEM) as a new electrochemical approach for imaging transient and heterogeneous electrochemical processes. This method uses a bipolar electrode mechanism to directly couple a conventional oxidation reaction, e.g., the oxidation of ferrocene, to a special fluorogenic reduction reaction. The generation of the fluorescent product on the cathodic pole enables one to directly monitor an electrochemical process with optical microscopy. We demonstrate the use of this method on a large electrochemical array containing thousands or more parallel bipolar microelectrodes to enable spatially and temporally resolved electrochemical imaging. We first image molecular transport of a redox analyte in solution using an array containing roughly 1000 carbon fiber ultramicroelectrodes. We then carry out a simple electrocatalysis experiment to show how FEEM can be used for electrocatalyst screening. This new method could prove useful for imaging transient electrochemical events, such as fast exocytosis events on single and networks of neurons, and for parallel, high throughput screening of new electrocatalysts.

1.4 Bipolar Electrochemistry

A bipolar electrode (BPE) is an electrode in which no direct electrical connection is made between it and the external circuit. Instead a voltage is applied across the length of a solution or two separate solution compartments in order to induce an electron transfer process. Recently BPEs[13,14] have proven to be useful for many analytical sensing[15] and separation applications.[16] The Crooks group has been at the leading edge of this work, developing or refining BPE detection methods such as electrodissolution[17] and electrochemiluminescence[18,19] and applications such as DNA detection and analytical separation. Much of the previous work in bipolar electroanalytical chemistry has focused on the use of an "open" cell with the BPE located in an open microchannel. A closed BPE, on the other hand, has two poles placed in separate compartments and has remained relatively unexplored in this field. Closed BPEs have the ability to couple two reactions that may occur in immiscible solutions or would otherwise be incompatible if were combined in a channel of an open BPE cell. Additionally, due to the lack of the open microfluidic channel and accompanying ionic current, the only electrical connection provided between the two driving electrodes in a closed bipolar cell is the BPE itself. This allows for the direct measurement of the current through the BPE in the external circuit.

Chapter 3 begins our fundamental study into the voltammetric behavior of coupled electrochemical reactions on microelectrodes and nanoelectrodes in a closed bipolar cell. We use steady-state cyclic voltammetry to evaluate and discuss the overall voltammetric response of closed BPEs and understand its dependence on the concentration of redox species and electrode size. We demonstrate that carbon-fiber microelectrodes, typically used in amperommetric analysis, when backfilled with an electrolyte to establish conductivity are

closed BPEs. The coupling between the oxidation reaction, e.g., dopamine oxidation, on the carbon disk/cylinder and the reduction of oxygen on the interior fiber is likely to be responsible for the conductivity. We also demonstrate the ability to quantitatively measure voltammetric properties of both the cathodic and anodic poles in a closed bipolar cell from a single CV scan. It was found that "secondary" reactions such as oxygen reduction play an important role in this process. We also described the fabrication and use of Pt bipolar nanoelectrodes which may serve as a useful platform for future advances in nanoscale bipolar electrochemistry.

For a more in-depth investigation into the fundamental behavior of BPEs chapter 4 reports the theory and experimental study of the steady-state voltammetric behavior of a microelectrode used as a limiting pole in a closed bipolar electrochemical cell. We show that the steady-state voltammetric response of a microelectrode used in a closed bipolar cell can be quantitatively understood by considering the responses of both poles in their respective conventional two-electrode setups. In comparison to a conventional electrochemical cell the voltammetric response of the bipolar cell has a similar sigmoidal shape and limiting current, however, the response is often slower than that of the typical two-electrode setup. This leads to a broader voltammogram and a decreased wave slope which can be somewhat misleading and appear that the process being studied is irreversible when it instead can be a result of the coupling of two reversible processes. We show that a large limiting current on the excess pole would facilitate the observation of a faster voltammetric response and both redox concentration and electrode area of the excess pole affect the wave shape. Both factors should be maximized in electroanalytical experiments in order to obtain fast voltammetric

responses on the main electrode of interest and to detect quick changes in analyte concentrations.

1.5 Recessed Nanoelectrodes

Nanoelectrodes have several advantages over macroscale electrodes including small *iR* drop, as mentioned previously, as well as faster mass transport due to radial diffusion and lower capacitance charging allowing for experiments to be carried out on the order of the nanosecond timescale.[20] By placing the electrode at the bottom of a recess additional advantages arise, most notably an improvements in the uniformity of the current density along the electrode surface.[21,22] Additionally, electrodes of this design, particularly glass nanopore electrodes, have proven useful to studies of mass-transport within the confines of a recess[23-26] and may be beneficial to investigations of electric double layer structure.

Presented in chapter 5 is a detailed report on the fabrication and electrochemical response of recessed gold nanoband electrodes, hereafter referred to as gold nanotrench electrodes. Gold nanotrench electrodes of 12.5 and 40 nm in width with various depths from a few tens of nanometers to approximately 4 μm are fabricated and characterized by cyclic voltammetry. The fabrication of a Au nanotrench electrode follows a simple electrochemical etching process in which a small AC signal is applied to an inlaid Au nanoband electrode submersed in a NaCl solution. The voltammetric behavior of a Au nanotrench electrode is characterized by a quasi-steady-state response at lower scan rates (e.g., < 1 V/s for a 12.5-nm-wide electrode). We present an analytical expression for the quasi-steady-state diffusion-limited current of the nanotrench electrode based upon the analysis of the mass-transport resistance. Finite-element simulation of steady-state and transient voltammetric responses of the nanotrench electrodes provides additional insights for the analytical model. Peak-shaped

transient voltammetric responses were observed at scan rates as low as 5 V/s for both inlaid and nanotrench electrodes. This result may suggest that the exposed area of the nanoband electrode is much greater than that expected from the fabrication of the inlaid bands. However, the extent to which this is seen is greatly decreased in the nanotrench electrode by a smoothing effect during etching. Our results confirm previous reports of excess overhanging metal and delamination cracks contributing significantly to the shape and magnitude of the voltammetric response.

1.6 Nanopore Sensors

Resistive pulse sensing has advanced considerably since 1947 when Wallace Coulter first used a pierced cellophane wrapper to count cells.[27,28] Today biological ion-channel proteins and solid-state synthetic nanopores are routinely used for the detection of single molecules using the same principles described by Coulter six decades ago. A tremendous effort is currently underway to further advance nanopore sensing to a degree which will allow for high throughput DNA sequencing.[29] Part of this effort has focused on improving our fundamental understanding of the nonlinear current-voltage (*i*-*V*) response often seen with nanopores used in ion conductance measurements.[30-34] This phenomenon, known as current rectification, is generally believed to originate from the asymmetric distribution of surface charges on the pore walls[32] however it was not well understood.

We believe that a more complete understanding of the fundamental behavior of nanopore sensors will help improve the likelihood of the development of a successful DNA sequencing nanopore-based device. To this end chapter 6 reports the fundamental study of the voltammetric behavior of cone-shape silica nanopores in quartz nanopipettes in aqueous solutions as a function of the scan rate, ν. Current rectification behavior has been studied for

silica nanopores with diameters in the range of 4-25 nm. The rectification behavior was found to be strongly dependent on the scan rate. At low scan rates (e.g., $\nu < 1$ V/s), the rectification ratio was found to be at its maximum and is relatively independent of ν. At high scan rates (e.g., $\nu > 200$ V/s) a nearly linear current-voltage response was obtained. In addition, the initial voltage was shown to play a critical role in the current-voltage response of cone-shape nanopores at high scan rates. We explain this ν-dependent current-voltage response by ionic redistribution in the vicinity of the nanopore mouth.

1.7 References

(1) Bard, A. J.; Faulkner, L. R. *Electrochemical Methods*. 2nd ed.; John Wiley & Sons: New York, 2001.
(2) Bard, A. J.; Zoski, C. G. *Anal. Chem.* **2000**, *72*, 346A-352A.
(3) Hickling, A. *Trans. Faraday Soc.* **1942**, 38, 27-33.
(4) Cox, J. T.; Zhang, B. *Annu. Rev. Anal. Chem.* **2012**, *5,* 253-272.
(5) Saito, Y. *Rev. Polarogr*. **1968**, *15*, 177-182.
(6) Zhang, B.; Zhang, Y. H.; White, H. S. *Anal. Chem.* **2006**, *78*, 477-483.
(7) Li, Y.; Cox, J. T.; and Zhang, B. *J. Am. Chem. Soc.* **2010**, *132*, 3047-3052.
(8) Bard, A. J.; Fan, F.R.F.; Kwak, J.; Lev, O. *Anal. Chem.* **1989,** *61,* 131-138.
(9) Amemiya, S., Bard, A.J., Fan, F.-R.F., Mirkin, M.V.; Unwin, P.R. *Annu.Rev. Anal. Chem.* **2008,** *1,* 95-131.
(10) Eckhard, K., Chen, X., Turcu, F.; Schuhmann, W. *Phys. Chem. Chem. Phys.* **2006,** *8,* 5359-5365.
(11) Fernandez, J. L., Walsh, D. A.; Bard, A. J. *J. Am. Chem. Soc.* **2005,** *127,* 357-365.
(12) Schulte, A.; Nebel, M.; Schuhmann, W. *Annual Rev. Anal.Chem.* **2010,** *3*, 299-318.
(13) Mavre, F.; Anand, R. K.; Laws, D. R.; Chow, K. F.; Chang, B. Y.; Crooks, J. A.; Crooks, R. M. *Anal.Chem.* **2010,** *82*, 8766-8774.
(14) Loget, G.; Kuhn, A.; *Anal. Bioanal.Chem.* **2011,** *400,* 1691-1704.
(15) Chow, K. F.; Mavre, F.; Crooks, R. M. *J. Am. Chem. Soc.* **2008,** *130*, 7544-7545.
(16) Perdue, R. K.; Laws, D. R.; Hlushkou, D.; Tallarek, U.; Crooks, R. M. *Anal. Chem.* **2009,** *81*, 10149-10155.
(17) Chow, K. F.; Chang, B. Y.; Zaccheo, B. A.; Mavre, F.; Crooks, R. M., A. *J. Am. Chem. Soc.* **2010,** *132*, 9228-9229.
(18) Arora, A.; Eijkel, J. C. T.; Morf, W. E.; Manz, A. *Anal. Chem.* **2001,** *73*, 3282-3288.

(19) Mavre, F.; Chow, K. F.; Sheridan, E.; Chang, B. Y.; Crooks, J. A.; Crooks, R. M. *Anal.Chem.* **2009,** *81*, 6218-6225.
(20) Oja, S. M.; Wood, M.; Zhang, B. *Anal. Chem.* **2013**, *85*, 473-476.
(21) Weiland, J. D.; Anderson, D. J.; Pogatchnik, C. C.; Boogaard, J. J. *Proc. 19th Annu. Int. Conf. IEEE EMBS* **1997**, 2273–2276.
(22) Rubinstein, J. T.; Spelman, F. A.; Soma, M.; Suesserman, M. F. *IEEE Trans. Biomed. Eng.***1987,** *34*, 864-875.
(23) Zhang, B.; Zhang, Y. H.; White, H. S. *Anal. Chem.***2004,** *76*, 6229-6238.
(24) Sun, P. *Anal. Chem.* **2010,** *82*, 276-281.
(25) Li, Y. X.; Ito, T. *Anal. Chem.* **2009,** *81*, 851-855.
(26) Zhang, B.; Galusha, J.; Shiozawa, P. G.; Wang, G. L.; Bergren, A. J.; Jones, R. M.; White, R. J.; Ervin, E. N.; Cauley, C. C.; White, H. S. *Anal. Chem.* **2007,** *79*, 4778-4787.
(27) Coulter, W. H. US Patent #2,656,508 **1953**.
(28) Graham, M. D. *J. Lab Autom.* **2003**, *8*, 72–81.
(29) Wanunu, M. *Phys. Life Rev.* **2012**, 9, 125–158.
(30) Wei, C.; Bard, A. J.; Feldberg, S. W. *Anal. Chem.* **1997,** *69*, 4627-4633.
(31) Siwy, Z.; Heins, E.; Harrell, C. C.; Kohli, P.; Martin, C. R. *J. Am. Chem. Soc.,* **2004**, *126*, 10580-10581.
(32) Siwy, Z. S. *Adv. Funct. Mater.,* **2006**, *16*, 735-746.
(33) White, H. S.; Bund, A. *Langmuir*, **2008**, *24*, 2212-2218.
(34) Jin, P.; Mukaibo, H.; Horne, L. P.; Bishop, G. W.; Martin, C. R. *J. Am. Chem. Soc.* **2010**, *132*, 2118-2119.

CHAPTER 2
Fluorescence-Enabled Electrochemical Microscopy*

2.1 Introduction

The ability to spatially and temporally resolve electrochemical processes has become increasingly important for many investigations in the past several decades, particularly for electrocatalysis studies[1] and studies involving heterogeneous electrode surfaces[2] and biological redox processes.[3] Among the most widely applied electrochemical imaging methods is scanning electrochemical microscopy (SECM), which relies on the rastering of an ultramicroelectrode over a substrate of interest to obtain topographical or electrochemical information.[4,5] SECM has proven to be extremely valuable for applications such as mapping a catalytic surface,[6,7] studying molecular transport at localized domains,[8-11] and imaging single biological cells.[12,13] In addition to the stand alone technique, SECM has been combined with other imaging techniques such as atomic force microscopy (AFM)[14] and scanning ion-conductance microscopy (SICM).[15-17] Despite these outstanding properties, it is necessary, however, with SECM to make a compromise between image spatial resolution, scan-time and size of working area. Several attempts have been reported to overcome this limitation, most notably by Girault and coworkers who have used flexible linear microelectrode arrays to minimize the total scan duration.[18,19] However, if faster temporal

---

* This chapter is adapted with permission from Guerrette, J. P.; Percival, S. J.; Zhang, B. Fluorescence coupling for direct imaging of electrocatalytic heterogeneity *J. Am. Chem. Soc.* **2013**, *135,* 855-861. Copyright (2013) American Chemical Society.

information is desired for transient or short-lived processes, a scanning technique will not suffice.

Tao and coworkers have recently introduced an elegant electrochemical imaging method, which utilizes surface plasmon resonance (SPR) to detect local changes in current density[20,21] or electrochemical impedance[22,23] and to perform square wave voltammetry[24] at thin film gold electrodes. Their method can obtain data comparable to a conventional voltammetric response over various regions of an electrode with excellent sensitivity for small redox species such as $Ru(NH_3)_6^{3+}$ or TNT. However, this method requires the use of a thin-film gold electrode, which may limit its application in certain processes. Additionally, certain redox processes involving larger electroactive molecules may likely involve relatively little change in the index of refraction and thus a weak signal. Another challenge with this technique may be the deconvolution of local SPR changes due to heterogeneity of the electrochemical current from irregularities due to electrode surface functionalizations themselves.

To address the aforementioned challenges it would be desirable to use an array of thousands or more individually and simultaneously addressable microelectrodes. This, however, presents several major challenges, both in the array fabrication and the complex and costly electronics/data acquisition requirements for monitoring such an extreme number of channels. The Ewing group has extended the traditional limit to the numbers and size of microelectrode arrays for electrochemical analysis[25,26] including a recent report using an array containing fifteen ultramicroelectrodes.[27] This has allowed for the direct imaging of transient exocytosis events from single-cells. In order to significantly increase the number of

simultaneously-addressable electrodes and to spatially resolve smaller features, an alternative method for addressing individual microelectrodes and monitoring their current is necessary.

Here we report a new electrochemical approach, called fluorescence-enabled electrochemical microscopy (FEEM), to locally monitor electrochemical current on large electrochemical arrays. This method couples a fluorogenic redox reaction to the redox reaction of interest so that one can use fluorescence microscopy to examine a conventional faradaic reaction on individual microelectrodes. Extending this strategy on a closed bipolar electrochemical array allows one to simultaneously monitor thousands of electrodes. Figure 2.1a illustrates the basic principles of FEEM. At the core of the setup is a closed bipolar electrode,[28,29] which along with its surrounding insulative substrate completely separates the two solution compartments. One solution compartment contains an oxidizable redox analyte (**R**) while the other contains a buffered solution of resazurin (**S**). No direct electrical contact is made to the bipolar electrode from the external circuit thus simplifying the electrical setup. Instead, a small bias voltage is applied to two electrodes to couple the redox reactions on the bipolar electrode. The oxidation of **R** to **O** at the anodic pole is coupled to the two-electron, two-proton fluorogenic reduction of resazurin (Figure 2.1b). Optical monitoring of the fluorescent product of this reaction, resorufin (**P**), provides a convenient and sensitive way to measure the electrochemical signal of the analyte.

The use of fluorescence microscopy to study electrochemical processes is itself not a new concept. Fluorescence-voltage single molecule spectroscopy (F-V/SMS)[30] and single-molecule spectroelectrochemistry (SMS-EC), developed by Barbara and coworkers[31,32] has led to much related work for the study of electron transfer kinetics[33] and electrocatalytic reduction[34,35] of single organic dyes. While all of these studies demonstrate applications of

fluorescence-based electrochemical detection, their usefulness is strictly limited to investigations into the properties of a limited number of redox active fluorophores or special fluorogenic redox reactions. FEEM instead relies on the fluorogenic reaction only to report the rate of electrochemical processes involving redox species with no inherent fluorescence of their own. *This makes possible the broad application of FEEM to study nearly any redox active species.*

A unique advantage of this method is the ability to individually and simultaneously address a large number of parallel microelectrodes (e.g., $>10^4$) and optically monitor their faradaic response. The absence of a direct connection and the conversion of an electrochemical current signal to a fluorescence signal allow for the use of a large array of parallel bipolar electrodes. This provides a new means to spatially and temporally resolve electrochemical processes. In this report we first provide the initial demonstration of FEEM using two series-coupled microelectrodes. Next, electrochemical arrays containing thousands of ultramicroelectrodes are used to image redox species discharged from a glass micropipette. Finally, due to the growing interest in electrocatalyst screening[36,37] we demonstrate the use of FEEM to map catalytically active hot spots on a carbon fiber electrode array, which was selectively patterned and modified with Pt. Although this simple demonstration here uses only two materials it can be easily scaled up for high throughput, parallel, multicomponent screening of electrocatalysts.

2.2 Experimental Section

2.2.1 Chemicals and Materials.

Ferrocene (Fc, Fluka Analytical), ferrocenemethanol (FcMeOH, Aldrich), hydrogen peroxide (30%, J.T. Baker), tetra-*n*-butylammonium hexafluorophosphate ($TBAPF_6$,

Aldrich), potassium chloride (J.T. Baker), sodium sulfate (Fisher Chemicals), sodium hydroxide (J.T. Baker), monosodium phosphate (Fisher), disodium phosphate (J.T. Baker), platinum (IV) chloride (Aldrich), sulfuric acid (EMD Chemicals) and reagent grade acetonitrile (MeCN, Aldrich) were all used without further purification. Resazurin sodium salt (Aldrich) containing resorufin in small quantities was purified using previously established procedures.[38] A Barnstead Nanopure water purification system was used to provide >18 MΩ·cm deionized water for all aqueous solutions.

2.2.2 Fabrication of Bipolar CF Arrays and Pt Deposition.

Carbon pultrusion rods (OD 0.280 – 4mm) consisting of hundreds or thousands of individual 6-μm-diameter carbon fibers within an insulative epoxy binder were obtained from DPP Pultrusion through the distributor A2Z Corp. Sections of the rods were further sealed in Epo-Tek 301epoxy (Epoxy Technologies, Inc.) to further increase rigidity and provide additional isolation between both ends of the rods. Thin cross-sections of the resulting carbon fiber/epoxy rods were cut and then polished to the desired final thickness from ~0.1 to 4mm. CF arrays to be selectively patterned with Pt were first patterned with photoresist. Samples were spin coated with adhesion promoter (Micro Prime MP-P20 (20% hexamethyldisilazane (HMDS), 80% propylene glycol monomethyl-ether acetate (PGMEA)) then with AZ1512 photoresist (AZ Corporation). Patterning was accomplished using a chromium-on-glass UV mask and a Newport UV Flood Exposure System with a 500 Watt Hg lamp followed by developing to expose the selected carbon fibers (AZ351 developer AZ Corporation, diluted 1:5 developer:DI H_2O). Pt was deposited on exposed carbon fibers using a solution of 1 mM $PtCl_4$ and 0.5 M H_2SO_4 in a bipolar deposition configuration. To provide electron transfer at the anodic poles of the CF array a solution of 2 mM FcMeOH in 0.1 M

KCl was used and a potential pulse of -1.6 V for 200 ms followed by a resting potential of 0 V for 800 ms. The voltage was applied to two Ag/AgCl QREs for a total of 5 minutes.

2.2.3 FEEM Apparatus Setup.

An Olympus IX70 inverted microscope equipped with an IX-FLA inverted reflected light fluorescence observation attachment was used for all fluorescence experiments. Illumination was provided using an Olympus U-ULS100HG 100 W mercury burner. A filter set consisting of a HQ535/50 excitation filter, a Q565lp dichroic mirror and a HQ610/75 emission filter was used. Video/images were recorded using an Andor iXon+ EMCCD camera cooled to -80 °C and a Dell PC equipped with Andor SOLIS software. Electric potential was applied to two AgCl-coated Ag wire quasi-reference electrodes through a Chem-Clamp potentiostat (Dagan) connected to an EG&G 175 programmer. Voltammetric response was recorded using a PCI-6251 (National Instruments) card on a Dell PC using in-house LabView 8.5 software (National Instruments). A scan rate of 200 mV/s was used for all potential sweep experiments unless noted otherwise.

2.2.4 Video Acquisition and Processing.

Andor SOLIS software was used for all video/image recording and postprocessing. Video was recorded at a frame rate of 19.81 Hz for the experiments shown in Figure 2.5 and Figure 2.7 and 33.887 Hz for all other experiments. A pre-amplifier gain setting of 5.1 was used. Time derivative of fluorescent intensity is presented as a moving average for Figure 2.3c. (n=30) and Figure 2.9 (n=10) to smooth short-term fluctuations in fluorescent signal.

2.2.5 Scanning Electron Microscopy.

Scanning Electron Microscopy (SEM) images were obtained using a field-emission electron microscope (FEI Sirion). Samples were sputter coated with a thin layer (2-3 nm) of Au/Pd prior to imaging.

2.3 Results and Discussion

2.3.1 Fluorescence coupling on a closed bipolar electrode.

Here, we first use a simple closed bipolar electrode to demonstrate electrochemical coupling between the oxidation of ferrocene and the reduction of resazurin. Two 25-μm-diameter Au disk electrodes (SEM of the electrode surface shown in Figure 2.2) were connected in series to create a closed bipolar electrode as shown in Figure 2.3a. The anodic pole was placed in an acetonitrile solution containing 2.5 μM ferrocene and 0.1 M $TBAPF_6$ while the cathodic pole was placed in an aqueous solution containing 50 μM resazurin and 50 mM phosphate buffer (pH = 7.4). The solution surrounding the cathodic pole was illuminated (with a Hg lamp and a HQ535/50 excitation filter) to excite resorufin fluorescence. A triangular potential waveform 0-1.4 V was applied on the bipolar cell at a scan rate of 200 mV/s to oxidize ferrocene. This process was coupled to the reduction of resazurin to generate resorufin as a fluorescent product on the cathodic pole. Figure 2.3b shows five background corrected snapshots at selected voltages taken from a video recording a burst of fluorescence throughout the course of the potential sweep experiment. The sixth panel in Figure 2.3b is a plot of the fluorescence intensity versus time for the region over the electrode surface. The fluorescence signal seen here is the product of coupling the two electrochemical reactions, the oxidation of ferrocene and the fluorogenic reduction of resazurin, through the closed bipolar electrode.

For comparison Figure 2.3c shows the voltammetric responses of a 25-μm-diameter Au disk electrode in 2.5 μM Fc in a conventional two-electrode cell (blue) and the corresponding closed bipolar configuration as used in the above fluorescent experiment (red). It can be seen here that the current-voltage response of the bipolar configuration is somewhat broader than the response from the conventional cell and the curve is shifted to higher potentials. This change in wave slope is the result of coupling these two electrochemical processes and is not itself an indication of kinetic limitations.[39] Additionally, the position of the curve (i.e. the half-wave potential) can be approximated by taking the difference between formal potentials for the reactions at each of the two poles of the bipolar electrode. A more detailed discussion of the voltammetric response of closed bipolar electrodes can be found in our recent work.[28,39] The black curve shown in Figure 2.3c is the time derivative of the fluorescent intensity, *dI/dt*, at different applied potentials during the forward scan from 0 to 1.2 V. A nice correlation can be seen between the "fluorescence current" (black curve) and the corresponding electrochemical current (red curve). The total fluorescent count should be proportional to the total number of fluorescent resorufin molecules, which by Faraday's law (Q = nFN), is proportional to the total charge passed through the bipolar electrode. As such, the time derivative of the fluorescence count, *dI/dt*, could generate a response linearly correlated to the faradaic current response. Lei et al. have also recently shown the correlation between the derivative of fluorescence intensity and the measured electrochemical current for the quasi-reversible oxidation of cresyl violet.[33] Here, due to the relatively low concentration of ferrocene, the oxidation reaction on the anodic pole limits the overall faradaic response of bipolar electrode and the resulting "fluorescent voltammetric response" in Figure 2.3c is representative primarily of the oxidation of ferrocene. At short time intervals this

relationship holds true, however, other factors such as photobleaching, diffusion of fluorescent product and, at elevated potentials, further reduction of resorufin to the non-fluorescent dihydroresorufin[40] may lead to a more convoluted signal at extended times. Quantification of the fluorescent response and its exact relationship to electrochemical current is an inherently difficult task. This would require consideration of the extinction coefficients and quantum efficiencies of both the fluorescent product and the redox active precursor, the detector efficiency as well as other less easily quantifiable factors such as those discussed above. For this reason we believe that FEEM, in its present configuration, is more useful for measurements of relative electrochemical response. Additional controls and standards could be introduced into an experimental configuration to yield a more quantifiable result.

Figure 2.4 shows the results of several additional FEEM experiments for the oxidation of dopamine over the course of a potential sweep. The oxidation of dopamine and the reduction of resazurin are both two-electron electrochemical processes. Thus, we anticipate that there is a 1:1 ratio between the total oxidized dopamine on the anodic pole and the generated resorufin on the cathodic pole. Indeed, here we see a linear correlation between peak fluorescence intensity and dopamine concentration. In this present experimental configuration the limit of detection was approximately 1 μM, which corresponds to an oxidation limiting current of ~10 pA on the 25-μm-diameter gold ultramicroelectrode.[41] However, other parameters including volume and concentration of the resazurin solution and method of fluorescence monitoring may be adjusted in order to increase sensitivity. A more systematic study is needed to better understand the relationship between fluorescence

generation and electrochemical current including the possible use of other fluorogenic reporter reactions to improve sensitivity as well as to detect reducible analytes.

2.3.2 Fluorescence-Enabled Electrochemical Imaging.

A unique advantage of this method is that it can be used on an array of ultramicroelectrodes to image dynamic and heterogeneous redox processes. We demonstrate this concept using a carbon-fiber ultramicroelectrodes array. Figure 2.5a illustrates a scheme of an experiment designed to electrochemically image redox species. Here we use this array to detect and image FcMeOH molecules as they are released from a glass micropipette. An SEM image of the microelectrode array is shown in Figure 2.5b. This array consisted of nearly 1000 parallel carbon fibers, each with a diameter of ~6 μm and a length of ~200 μm, insulated from each other by epoxy. A constant voltage of 800 mV was applied between the two Ag/AgCl driving electrodes in the anodic (top) and cathodic (bottom) solution compartments. The 3-micron inner diameter tip micropipette containing an aqueous solution of 2 mM FcMeOH with 0.1 M Na_2SO_4 was placed at the left most edge of the array adjacent to the anodic poles (top) and discharged for 5 s at 1 PSI. A burst of fluorescence was immediately observed at the corresponding location on the cathodic poles of the bipolar array. An image showing the initial burst of fluorescence is presented in the top left panel of Figure 2.5c and demonstrates the ability to spatially resolve transient presence of FcMeOH near the surface of the carbon electrodes. Figure 2.5d is a composite image showing the initial fluorescent signal for a series of four experiments with the pipette placed at different locations demonstrating the ability to resolve signal a various locations on the same array. A series of six snapshots is presented in Figure 2.5c showing the growing fluorescent signal with time as more FcMeOH molecules are released from the pipette positioned at left. The

mass transport of FcMeOH at the anodic side of the array is visualized in this process. One drawback of this method, however, is the loss of spatial resolution due to diffusion of the fluorescent product along the surface of the microelectrode array.

Figure 2.6 shows the fluorescence intensities for select regions both to the right of the pipette tip location over the array and to the left of the tip over the insulating substrate. It can be seen that the intensity decays more rapidly with distance to the left than with an equal distance to the right indicating that transport of the analyte on the dark side of the array can be discerned from the diffusion of the fluorescent product alone. Diffusion of resorufin will of course lead to a decrease in spatial resolution at extended experiment times. This can possibly be hindered or even completely prevented by immobilizing these fluorescent molecules on the surface of the bipolar electrodes. However this may significantly decrease our upper limit of detection by lowering the concentration of fluorogenic reaction precursor available at or near the electrode surface. We are currently investigating methods to immobilize resazurin onto the electrodes without adversely affecting our detection limit.

To further explore the spatial resolution provided by FEEM in its present setting, a carbon-fiber array was patterned with photoresist on the anodic side (top) to physically block the oxidation of FcMeOH on selected regions of the bipolar electrode array. Only the carbon fiber surfaces inside the Husky pattern, shown in Figure 2.7a, are exposed to FcMeOH solution while the rest of the areas are covered with photoresist. No photoresist was placed on the cathodic side of the array where the fluorescence was observed. The FEEM image shown in Figure 2.7b provides a clear representation of the oxidation of 2 mM FcMeOH at the anodic poles of the array and the pattern is well resolved. There are however noticeable

distortions to the image seen in Figure 2.7b as compared to the pattern in Figure 2.7a. For example, in the fluorescent signal we see a brighter section at the jaw line of the Husky, flanked by two less intense regions. This distortion is likely due to irregularities in the original carbon fiber array such as lateral crosstalk or convergence/divergence of adjacent wires. We have found that very thin cross sections of the array, as thin as 100 μm, greatly reduce image distortions. We are working to incorporate highly ordered nanowire arrays into our setup to virtually eliminate this issue. The resolution of FEEM is currently limited by the size of each of the individual carbon fibers of the array, approximately 6 μm for the arrays used here. However, we anticipate greatly increasing the spatial resolution through the use of metallic nanowire arrays.

2.3.3 Electrochemical imaging of electrocatalytic heterogeneity.

Development of new electrocatalysts requires quick and rigorous screening to determine their activity. As a result, there has been an increasing demand for improved high throughput screening methods. FEEM provides an excellent platform for quick, parallel screening of electrocatalytic materials. To demonstrate the use of FEEM for electrocatalyst screening, a simple experiment was carried out where a carbon fiber bipolar electrode array was selectively patterned with platinum on one side and used to study the electrocatalytic oxidation of hydrogen peroxide (Figure 2.8a). SEM images of the array (Figure 2.8b) show the five regions where Pt about 200 nm thick was electrochemically deposited on individual carbon fibers within the array. The remaining bare carbon fibers were unmodified. A solution of 10 mM H_2O_2 in 0.1 M NaOH was placed on the dark side of the array with the Pt-coated carbon fibers (Pt-CF). A voltage ramp from -400 to 700 mV was applied on the bipolar array to allow for the oxidation of H_2O_2. A large contrast in the oxidation signal can be clearly seen

between the Pt covered region and the remaining bare fibers. Figure 2.8c shows an FEEM image (top) and corresponding line scan (bottom) taken at the peak fluorescence intensity from a video recorded during the potential sweep. The five regions corresponding to the Pt-CFs are well resolved in the fluorescence image showing the much higher electrocatalytic activity of Pt to H_2O_2 oxidation versus bare carbon fiber.

In a subsequent experiment the hydrogen peroxide solution was replaced with 2 mM FcMeOH in 0.1 M KCl and the potential was swept from 0 to 1 V. Unlike H_2O_2, FcMeOH is oxidized by an outer-sphere mechanism and therefore the electron transfer kinetics is relatively independent of the electrode material. This can be visualized using FEEM as shown in Figure 2.8d, where the entire array fluoresces almost uniformly. The voltammetric response of a single bare carbon fiber and resulting Pt-CF after deposition in the same solutions of H_2O_2 and FcMeOH are shown in Figure 2.8e and Figure 2.8f, respectively. As expected the oxidation of hydrogen peroxide is strongly dependent upon the electrode material, showing a much greater current response after Pt deposition. The response of the bare CF and Pt-CF in FcMeOH, on the other hand, are very similar in magnitude. Slight differences in charging current and a more peak shaped response with the Pt-CF is likely due to increased surface roughness and an increased contribution due to linear diffusion.

The time derivative of the fluorescent signal intensity, like in the FEEM experiment using single electrodes shown in Figure 2.3, can be used to obtain information comparable to traditional electrochemical current signal. The fluorescent voltammetric response from the FEEM videos for the oxidation of H_2O_2 and FcMeOH are shown in Figure 2.9a and Figure 2.9b, respectively. Like the conventional voltammetric response, the fluorescent voltammetric response shows a clear difference in the catalytic activity for a region of bare

carbon fibers versus a region of Pt-CF with hydrogen peroxide oxidation, but little difference in the response for FcMeOH oxidation. This simple demonstration of the possible application of FEEM to electrocatalyst screening uses only two materials, platinum and carbon fiber. However, large scale use of this method to interrogate an array containing hundreds of parallel, multicomponent materials could be realized with little additional cost or technical requirements. Furthermore, significant improvements to the resolution of FEEM can be expected through the use of highly uniform, dense electrochemical arrays.

2.4 Conclusions

In summary, we have studied the electrochemical coupling of a fluorogenic reduction reaction and conventional oxidation reactions (e.g., oxidation of Fc, dopamine, and H_2O_2) on closed bipolar microelectrodes and their array. The generation of a fluorescent product allows one to use highly sensitive fluorescence microscopy to observe electrochemical kinetics and monitor electrocatalytic heterogeneity over large electrochemical arrays. This is a unique electrochemical imaging approach to study many conventional electrochemical oxidation reactions with excellent spatial and temporal resolutions. We have shown the correlation between the derivative of fluorescence intensity and electrochemical current and are currently carrying out additional studies in order to quantify this relationship. The use of fluorogenic oxidation reactions, such as the oxidation of cresyl violet or amplex red, may be used in future experiments to allow for the extension of this method to the detection of reducible analytes. We have briefly shown the applicability of FEEM to electrocatalyst screening and believe that it could serve as a useful platform for high throughput, multicomponent, and parallel testing. The future incorporation of arrays of bipolar

nanoelectrode into the FEEM configuration holds the possibility for reaching submicron or even diffraction-limited resolution.

2.5 Figures

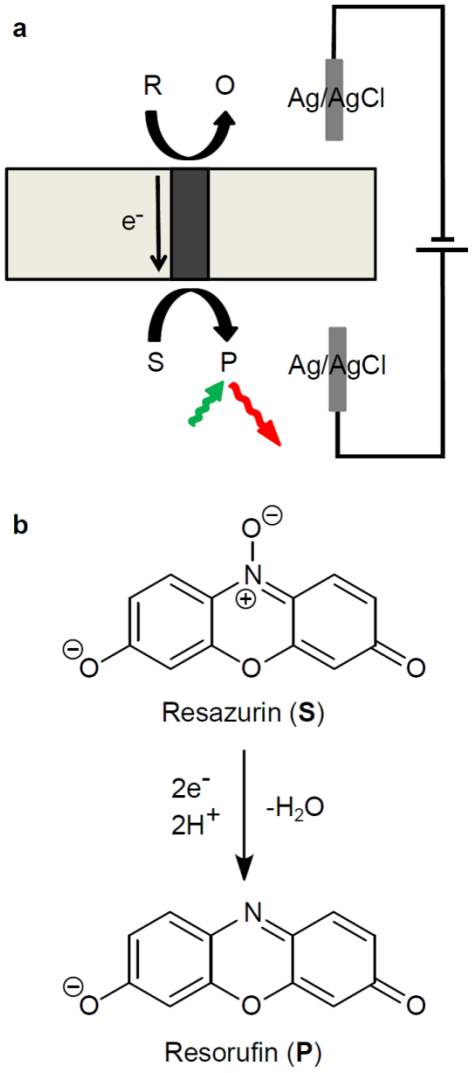

Figure 2.1 Fluorescence-enabled electrochemical microscopy.
(a) Schematic illustrating the basic principle of FEEM and (b) the fluorogenic reduction of resazurin

.

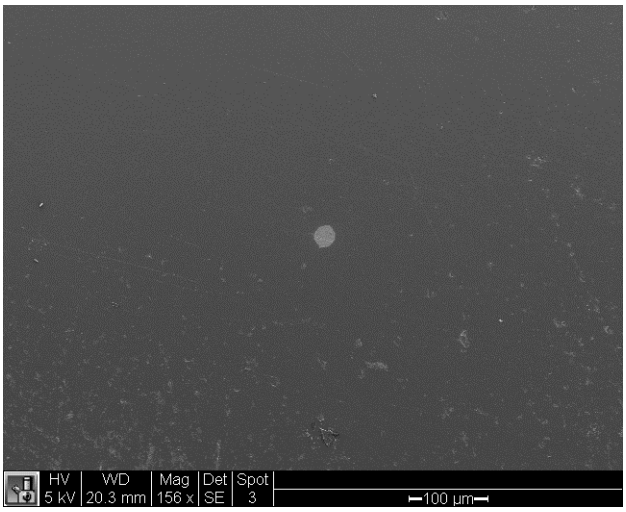

Figure 2.2 SEM image of 25 µm Au electrode.
Scanning electron micrograph showing a 25µm diameter Au disk electrode used for the series coupled BPE FEEM experiments.

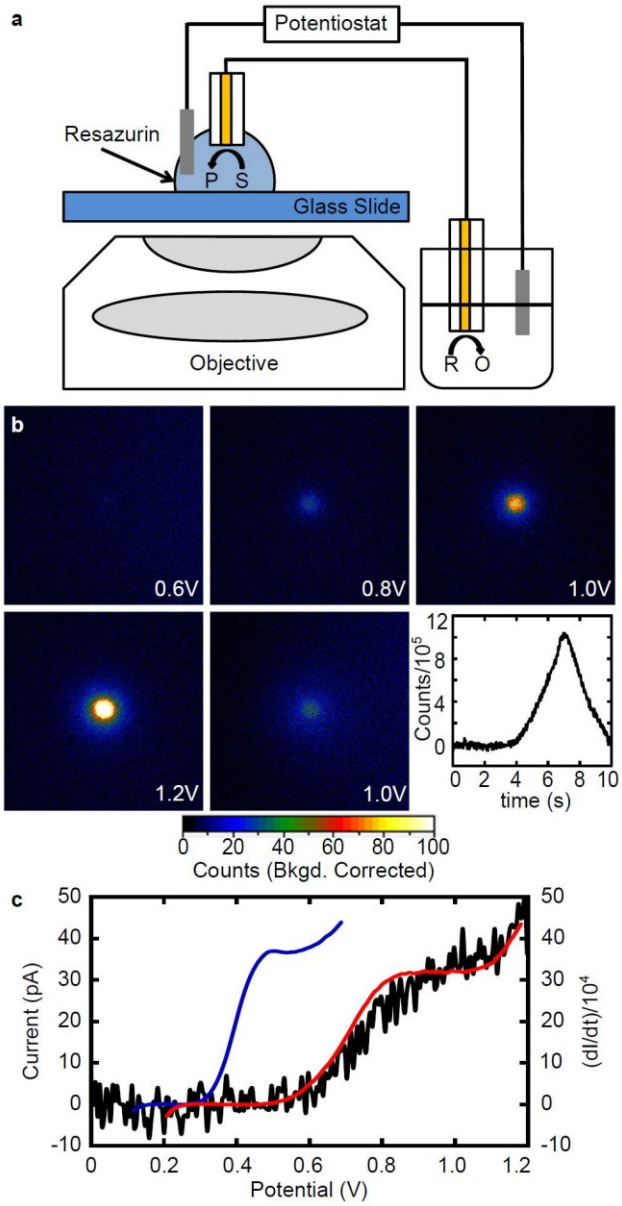

Figure 2.3 FEEM based analysis using two microelectrodes connected in series.
(a) Schematic for experimental FEEM setup in which two microelectrodes are connected in series to create the BPE. (b) A series of fluorescence images over the course of a potential sweep experiment (0-1.4V, 200mV/s) for the detection of 2.5 µM Fc using 50 µM resazurin 50mM phosphate buffer pH = 7.4. The last panel shows the total fluorescence counts plotted as a function of time during the voltage sweep. (c) Voltammetric response of a 25µm Au disk electrode in 2.5µM Fc (blue curve), the response when the same electrode is connected in series to another 25µm Au disk electrode in 50 µM resazurin (red curve) and the time derivative of the fluorescence intensity (black trace) for the experiment shown in (b) as a function of potential from 0-1.2V.

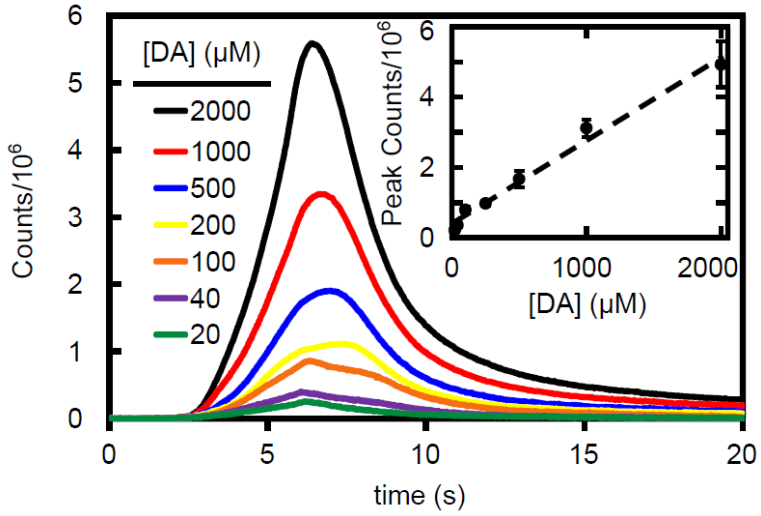

Figure 2.4 Concentration dependence of FEEM.
Fluorescence intensity for several FEEM experiments during a potential sweep (0.4 -1.6V, 200mV/s) for the detection of dopamine (DA) using two series coupled, 25 μm diameter Au disk electrodes and the concentration dependence of the peak fluorescence intensity (inset).

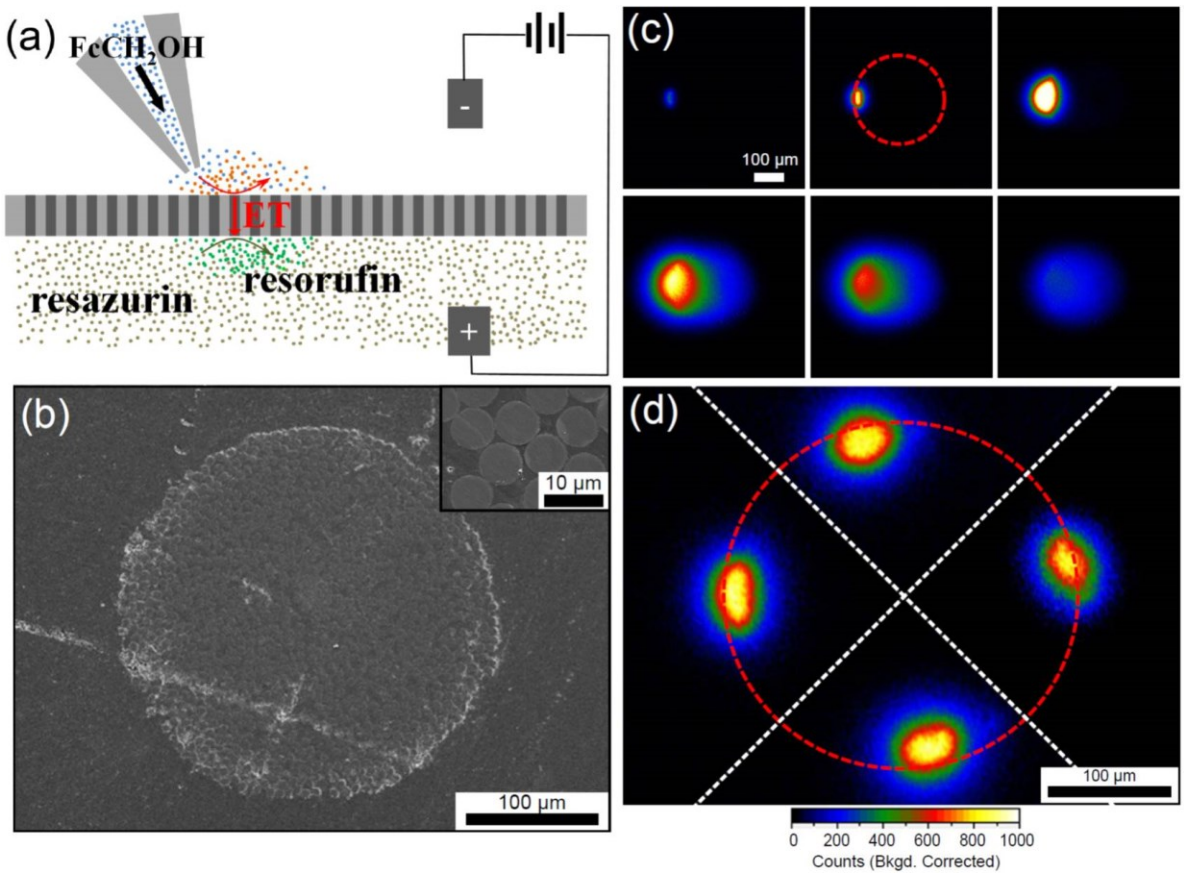

Figure 2.5 Fluorescence imaging redox analyte mass-transport.
A schematic diagram (a) showing the setup to image release of FcMeOH from a glass micropipette with an array of carbon-fiber ultramicroelectrodes. The FcMeOH molecules are oxidized on the top surface of the carbon electrodes generating resorufin on the bottom surface of the carbon rods. (b) Scanning electron micrograph of a 300 µm diameter CF array consisting of hundreds of individual 5 µm diameter carbon fibers in parallel. (c) Fluorescence snapshots recorded from an experiment in which a solution of 2 mM FcMeOH with 0.1 M Na_2SO_4 was discharged from a 3-µm micropipette for 5 s at 1 PSI onto the left most side of a CF array with a total diameter of 300 µm. (d) Composite fluorescence image showing the initial fluorescence bursts when the analyte solution was discharged at four separate locations on the dark side of the array. Potential was help at 800mV.

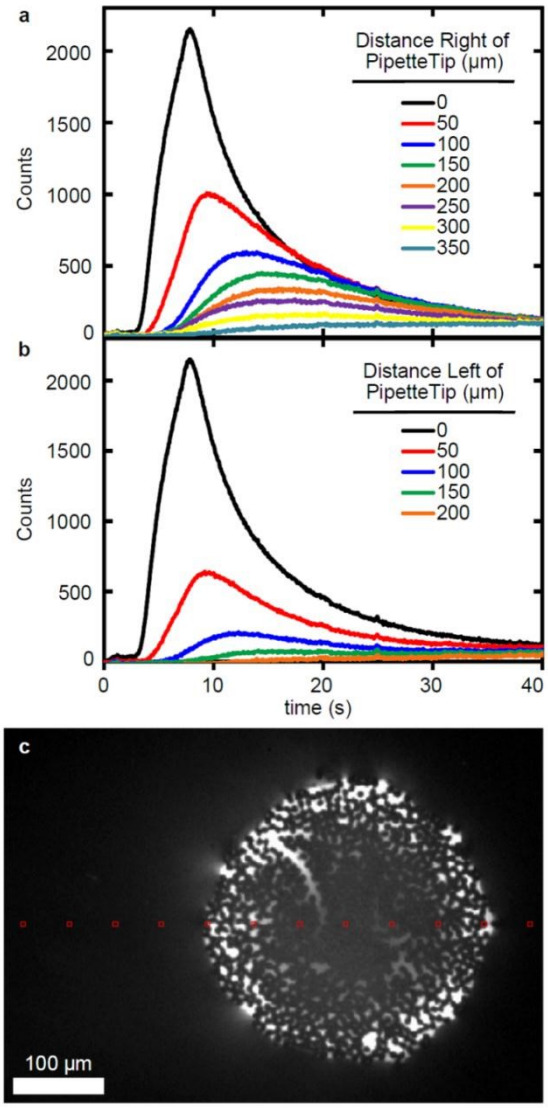

Figure 2.6 Fluorescence intensity after redox solution discharge from micropipette. Fluorescence intensity for FEEM experiment shown in Figure 2.5 at various positions (a) to the right over the CF array showing mass transport of analyte and diffusion of resorufin and (b) to the left showing only diffusion of resorufin for 10x10 pixel regions shown as red squares in (c). It can be seen that the signal decays much more rapidly to the left with time and distance indicating that signal over array is indicative of FcMeOH mass transport and can be distinguished from diffusion of resorufin alone.

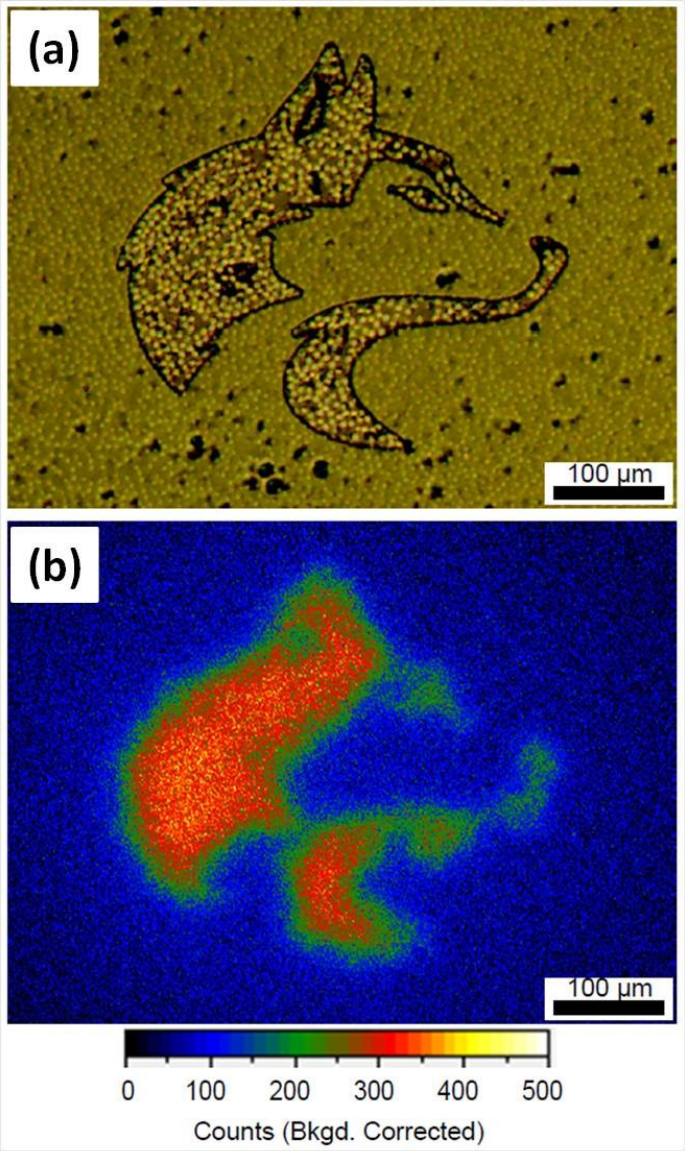

Figure 2.7 Spatially resolved imaging using FEEM.
Optical micrograph of a CF array patterned with photoresist (a) and a FEEM image of the oxidation of 2mM FcMeOH at the patterned anodic side of the array (b).

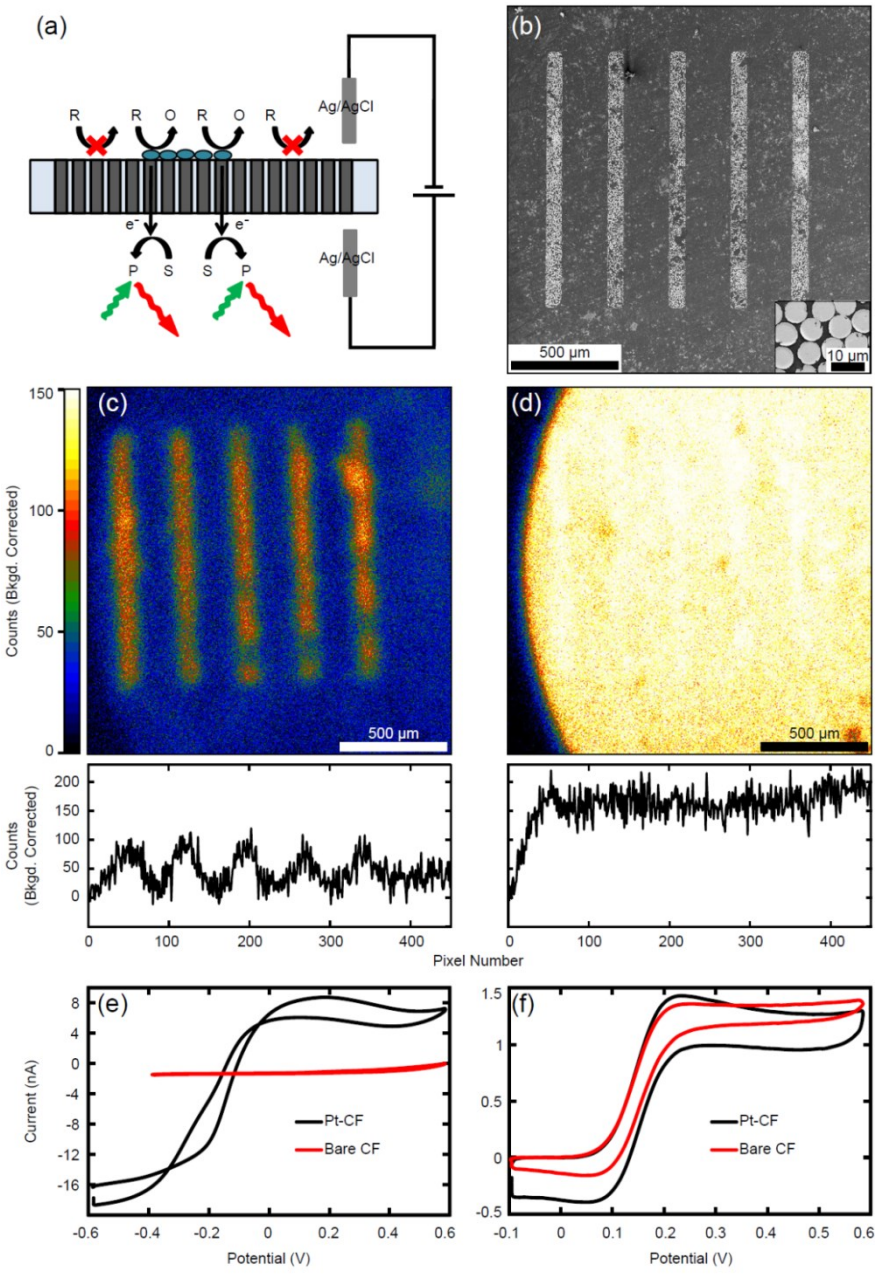

Figure 2.8 Application of FEEM for catalyst screening.
(a) Schematic showing the experimental design and (b) an SEM images showing the pattern of Pt deposition on the CF array surface with higher resolution image inset. (c) FEEM image (top) and line scan (bottom) showing the oxidation of 10mM H_2O_2 in 0.1M NaOH at catalytically active "hot-spots" where Pt was deposited on a CF array. (d) FEEM image for the same Pt patterned CF array showing the non-selective oxidation of 2mM FcMeOH in 0.1M KCl. (e) and (f) are the cyclic voltammetric response of a single 5µm diameter CF electrode in 10mM H_2O_2 and 2mM FcMeOH, respectively before and after Pt deposition on the electrode surface.

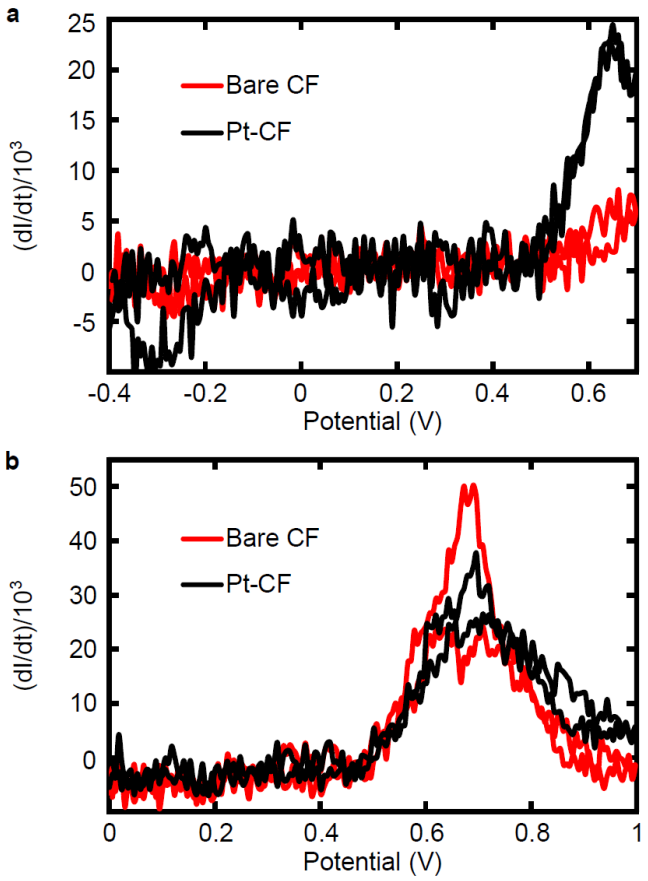

Figure 2.9 Fluorescent voltammetric response from catalyst screening experiment. Time derivative of the fluorescence intensities for the experiment shown in Figure 2.8 as a function of potential for (a) the catalytic oxidation of 10mM H_2O_2 at a Pt patterned CF array and (b) the non-selective oxidation of 2mM FcMeOH in 0.1M KCl at the same Pt patterned CF array.

2.6 Supplement: Derivation of the relationship between the Faradaic current on a closed bipolar electrode and the time derivative of the fluorescence intensity.

Assuming that all fluorophores can be treated identical, the overall fluorescence intensity from fluorophores in detection volume can be described as follows:

$$I(t) = N(t) \cdot \kappa \cdot I_{ex}(r) \cdot S(r) \cdot \sigma(\lambda) \cdot \phi(\lambda) \tag{1}$$

where, $I(t)$ is the time-related fluorescence intensity collected on the CCD detector, $N(t)$ is the number of fluorophores in the detection volume, κ is the overall detection efficiency, $I_{ex}(r)$ is spatial distribution of the excitation energy with the maximum amplitude I_0, $S(r)$ is the optical transfer function of the objective which determines the spatial collection efficiency of the setup, $\sigma(\lambda)$ and $\phi(\lambda)$ are the absorption cross-section (absorption extinction coefficient) of the fluorophore and the quantum yield, respectively.

Given Faraday's law, $Q = nFN$, where n is the number of electrons transferred in the process and F is Faraday's constant, the Faradaic current on the bipolar electrode can be expressed as,

$$i = \frac{dQ}{dt} = nF\frac{dN}{dt} \tag{2}$$

Combing equations (1) and (2), we can obtain an expression relating the electrochemical current of a fluorogenic redox reaction, i, to the change in fluorescence intensity.

$$i = \frac{nF}{\kappa \cdot I_{ex}(r) \cdot S(r) \cdot \sigma(\lambda) \cdot \phi(\lambda)}\frac{dI}{dt} \tag{3}$$

Alternatively, we can derive a similar liner relationship between the electrochemical current and the fluorescence intensity from a "bulk" perspective. Fluorescence intensity can be quantified using the Beer-Lambert law where at low fluorophore concentrations simplifies to the following expression,

$$I = I_0 k\phi \ln(10)\varepsilon b C \tag{4}$$

where I is the fluorescence intensity, I_0 is the excitation light intensity, k is a constant for the system that includes the detection efficiency and other geometric instrumentation parameters, b is the path length of illuminated sample and ϕ is the quantum yield, ε is the extinction coefficient and C is the concentration of the given fluorophore. Converting concentration into number of fluorophores, N, in the volume given by bA_I, where A_I is the area illuminated gives:

$$I = I_0 k\phi \ln(10)\frac{\varepsilon N}{A_I} \tag{5}$$

$$\frac{dI}{dt} = \frac{I_0 k\phi \ln(10)\varepsilon}{A_I}\frac{dN}{dt} \tag{6}$$

Given Faraday's law, $Q = nFN$, where n is the number of electrons transferred in the process and F is Faraday's constant, the Faradaic current on the bipolar electrode is

$$i = \frac{dQ}{dt} = nF\frac{dN}{dt} \tag{7}$$

We can then obtain an expression relating the electrochemical current of a fluorogenic redox reaction to the change in fluorescence intensity.

$$i = \frac{nFA_I}{I_0 k\phi \ln(10)\varepsilon}\frac{dI}{dt} \tag{8}$$

For resorufin, the quantum efficiency ϕ is ~0.97 (in neutral to basic solutions) and the extinction coefficient ε (570nm) is 57000 M^{-1} cm^{-1}. [40]

2.7 References

(1) Sanchez-Sanchez, C. M.; Bard, A. J. *Anal. Chem.,* **2009**, *81*, 8094-8100.

(2) Basame, S. B.; White, H. S. *Anal. Chem.*, **1999**, *71*, 3166-3170.

(3) Kurulugama, R. T.; Wipf, D. O.; Takacs, S. A.; Pongmayteegul, S.; Garris, P. A.; Baur, J. E. *Anal. Chem.,* **2005**, *77*, 1111-1117.

(4) Bard, A. J.; Fan, F. R. F.; Kwak, J.; Lev, O. *Anal. Chem.,* **1989**, *61***,** 131-138.

(5) Amemiya, S.; Bard, A. J.; Fan, F. -R. F.; Mirkin, M. V.; Unwin, P.R. *Annu. Rev. Anal. Chem.,* **2008**, *1*, 95-131.

(6) Eckhard, K.; Chen, X.; Turcu, F.; Schuhmann, W. *Phys. Chem. Chem. Phys.,* **2006**, *8*, 5359-5365.

(7) Fernandez, J. L.; Walsh, D. A.; Bard, A. J. *J. Am. Chem. Soc.,* **2005**, *127*, 357-365.

(8) Scott, E. R.; White, H. S.; Phipps, J. B. *Anal. Chem.*, **1993**, *65*, 1537-1545.

(9) McKelvey, K.; Snowden, M. E.; Peruffo, M.; Unwin, P. R. *Anal. Chem.*, **2011**, *83*, 6447-6454.

(10) Uitto, O. D.; White, H. S. *Anal. Chem.,* **2001**, *73*, 533-539.

(11) Shen, M.; Ishimatsu, R.; Kim, J. and Amemiya, S. *J. Am. Chem. Soc.,* **2012**, *134*, 9856-9859.

(12) Bard, A. J.; Li, X.; Zhan, W. *Biosens. & Bioelectron.*, **2006**, *22*, 461-472.

(13) Schulte, A.; Nebel, M.; Schuhmann, W. *Annual Rev. Anal.Chem.,* **2010**, *3*, 299-318.

(14) Gardner, C. E.; Macpherson, J. V. *Anal. Chem.,* **2002**, *74*, 576A-584A.

(15) Morris, C. A.; Friedman, A. K.; Baker, L. A. *Analyst,* **2010**, 135, 2190-2202.

(16) Comstock, D. J.; Elam, J. W.; Pellin, M. J.; Hersam, M. C. *Anal. Chem.,* **2010**, *82*, 1270-1276.

(17) Takahashi, Y.; Shevchuk, A. I.; Novak, P.; Murakami, Y.; Shiku, H.; Korchev, Y. E.; Matsue, T. *J. Am. Chem. Soc.,* **2010**, *132*, 10118-10126.

(18) Cortes-Salazar, F.; Momotenko, D.; Lesch, A.; Wittstock, G.; Girault, H. H. *Anal. Chem.,* **2010**, *82*, 10037-10044.

(19) Lescha, A.; Momotenkob, D.; Cortés-Salazarb, F.; Wirthc, I.; Tefashea, U. M.; Meinersa, F.; Vaskea, F.; Giraultb, H. H.; Wittstock. G. *J. Electroanal. Chem.,* **2012**, *666*, 52-61.

(20) Shan, X.; Patel, U.; Wang, S.; Iglesias, R.; Tao, N. J. *Science* **2010**, *327*, 1363-1366.

(21) Shan, X.; Díez-Pérez, I.; Wang, L.; Wiktor, P.; Gu, Y.; Zhang, L.; Wang, W.; Lu, J.; Wang, S.; Gong, Q.; Li, J. H.; Tao, N. J. *Nat. Nanotech.,* **2012**, *7*, 668-672.

(22) Foley, K. J.; Shan, X.; Tao, N. J. *Anal. Chem.,* **2008**, *80*, 5146-5151.

(23) Wang, W.; Foley, K.; Shan, X.; Wang, S.; Eaton, S.; Nagaraj, V. J.; Wiktor, P.; Patel, U.; Tao, N. J. *Nat. Chem.,* **2011**, *3*, 249-253.

(24) Shan, X., Wang, S., Wang, W. & Tao, N. *Anal. Chem.,* **2011**, *83*, 7394-7399.

(25) Zhang, B.; Adams, K. L.; Luber, S. J.; Eves, S. J.; Heien, M. L.; Ewing, A. G. *Anal. Chem.,* **2008**, *80*, 1394-1400.
(26) Zhang, B.; Heien, M. L. A. V.; Santillo, M. F.; Mellander, L.; Ewing, A. G. *Anal. Chem.,* **2011**, *83*, 571-577.
(27) Lin, Y.; Trouillon, R.; Svensson, M. I.; Keighron, J. D.; Cans, A-S.; Ewing, A. G. *Anal. Chem.,* **2012**, *84*, 2949-2954.
(28) Mavre, F.; Anand, R. K.; Laws, D. R.; Chow, K. F.; Chang, B. Y.; Crooks, J. A.; Crooks, R. M. *Anal. Chem.,* **2010**, *82*, 8766–8774.
(29) Guerrette, J. P.; Oja, S. M.; Zhang, B. *Anal.Chem.,* **2012**, *84*, 1609-1616.
(30) Gesquiere, A. J.; Park, S. J.; Barbara, P. F., *J. Phys. Chem. B* **2004,** *108,* 10301-10308.
(31) Palacios, R. E.; Fan, F. R. F.; Bard, A. J.; Barbara, P. F., *J. Am. Chem. Soc.* **2006,** *128*, 9028-9029.
(32) Palacios, R. E.; Fan, F. R. F.; Grey, J. K.; Suk, J.; Bard, A. J.; Barbara, P. F., *Nature Mater.* **2007,** *6*, 680-685.
(33) Lei, C.; Hu, D.; Ackerman, E. J. *Chem. Commun.*, **2008**, 5490-5492.
(34) Xu, W.; Kong, J. S.; Yeh, Y. T. E.; Chen, P., *Nature Mater.* **2008,** *7*, 992-996.
(35) Xu, W.; Shen, H.; Kim, Y. J.; Zhou, X. C.; Liu, G. K.; Park, J.; Chen, P., *Nano Lett.* **2009,** *9*, 3968-3973.
(36) Smotkin, E. S.; Diaz-Morales, R. R. *Annu. Rev. Mater. Res.,* **2003**, *33*, 557-579.
(37) Fosdick, S. E.; Crooks, R. M. *J. Am. Chem. Soc.,* **2012**, *134*, 863-866.
(38) Han, K. S.; Liu, G. K.; Zhou, X. C.; Medina, R. E.; Chen, P. *Nano Lett.* **2012**, *12*, 1253-1259.
(39) Cox, J. T.; Guerrette, J. P.; Zhang, B. *Anal. Chem*. **2012**, *84*, 8797-8804.
(40) Xu, W.; Kong, J. S.; Yeh, Y. T. E.; Chen, P. *Nature Mater.,* **2008**, *7*, 992-996.
(41) Adams, K. L.; Jena, B. K.; Percival, S. J.; Zhang, B. *Anal. Chem.,* **2011**, 83, 920-927.

CHAPTER 3
Coupled Electrochemical Reactions at Bipolar Microelectrodes and Nanoelectrodes*

3.1 Introduction

Electroanalytical chemists have recently become interested in the unique properties of bipolar electrodes (BPEs) and their application towards novel sensing and separation systems.[1,2] Several interesting studies have been published lately, predominantly by the Crooks group, discussing new detection schemes[3-6] and new applications of BPEs in sensing[7] and separation.[8] Previous work, however, has primarily focused on the use of open bipolar systems in which a BPE or an array is placed inside a microfluidic channel. Figure 3.1a illustrates a schematic of a typical open bipolar cell containing a pair of driving electrodes to apply a voltage along the length of the channel which polarizes the electrode. A significant portion of the total current between the driving electrodes is carried by an ionic current within the microchannel. As such, the electrochemical reaction rate on the BPE in general cannot be monitored by the current in the external circuit. The voltage needed to achieve the desired faradic response is inversely proportional to the length of the BPE[1] and can be quite large for certain applications.

A closed bipolar electrode[9] eliminates the microfluidic path thus completely separating the two poles in two different compartments. Figure 3.1b displays the basic design of a closed bipolar cell, which also uses two driving electrodes to supply a voltage across the

---

* This chapter is adapted with permission from Guerrette, J. P., Oja, S. M. & Zhang, B. Coupled Electrochemical Reactions at Bipolar Microelectrodes and Nanoelectrodes. *Anal. Chem.* **2012**, 84, 1609-1616. Copyright (2012) American Chemical Society.

two separated solutions. This voltage is dropped almost entirely at the solution interface adjacent to the two ends of the BPE when two ideal nonpolarizable electrodes, e.g., Ag/AgCl electrodes, are used. A relatively small voltage (<1 V) is normally sufficient to drive both redox reactions on the BPE. In this case the entire electrical current must pass through the BPE and can therefore be used to report the rates of the faradic processes on the BPE. In this study we limit our discussion to closed BPEs. This system is analogous to two series-coupled electrochemical cells, as recently described by Dryfe and co-workers.[10] Such cells have been used to study electron transfer at liquid/liquid interfaces[10-12] and electroless deposition.[13]

It is important to note that one of the most common examples of a closed BPE used in electroanalytical chemistry, although not previously described as such, could be the carbon-fiber microelectrode (CFE). CFEs are routinely used for both single-cell studies[14] and *in vivo* experiments.[15] These electrodes are usually prepared by sealing a small carbon fiber in a pulled glass capillary pipet. The fiber is then beveled or cut to obtain a disk or cylinder electrode. Although other means exist,[16] electrical conductivity on the interior pipet is often established by backfilling the capillary with an aqueous solution of KCl[17,18] or potassium acetate[19,20] and inserting a Ag or steel wire[21]. This procedure is advantageous because it facilitates rapid change of CFEs between cell experiments. It is assumed that the rate of electron transfer on the interior fiber is capable of occurring in sufficient excess to allow for quantitative measurements limited solely by the oxidation reaction at the carbon electrode. We believe that this assumption may not always be true and that a deeper investigation into the redox coupling at closed BPEs is necessary to improve the reliability of such measurements.

In this report we start by investigating the voltammetric response of CFEs. We then focus on a simplified setup in which two electrochemical cells are coupled in series. This setup allows us to use well-characterized Au and Pt microelectrodes and nanoelectrodes connected in series to obtain a more detailed understanding of the voltammetric behavior of closed bipolar microelectrodes. We then return our discussion to CFEs and the voltammetric detection of dopamine (DA). Through this investigation we begin to understand the role of secondary reactions (ie. the oxidation of water and reduction of oxygen) in the response of BPEs in aqueous solutions. We demonstrate the ability to obtain quantitative information (such as electrode size or redox concentration) about both poles of a closed bipolar cell in a single voltammetric scan. Finally we briefly discuss the use of bipolar nanoelectrodes.

3.2 Experimental Section

3.2.1 Chemicals.

Potassium ferricyanide ($K_3Fe(CN)_6$, Sigma-Aldrich), potassium ferrocyanide ($K_4Fe(CN)_6$, Fluka), ferrocene (Fc, Fluka Analytical), ferrocenemethanol (FcMeOH, Aldrich), dopamine hydrochloride (DA, Sigma-Aldrich), hexaammineruthenium (III) chloride ($Ru(NH_3)_6Cl_3$, Aldrich), tetra-*n*-butylammonium hexafluorophosphate ($TBAPF_6$, Aldrich), KCl (J.T. Baker), sodium sulfate (Na_2SO_4, Fisher Chemicals), perchloric acid ($HClO_4$, Aldrich) and reagent grade MeCN (Aldrich) were all used without further purification. A Barnstead Nanopure water purification system was used to provide >18 MΩ·cm deionized water for all aqueous solutions.

3.2.2 Fabrication of CFEs and Pt Bipolar Nanoelectrodes.

CFEs were fabricated following our previously reported procedures.[22] Briefly, an isolated carbon fiber (5-μm-diameter) was aspirated into a borosilicate glass capillary (1.2

mm O.D., 0.69 mm I.D., Sutter). Capillaries were subsequently pulled with a P-97micropipet puller (Sutter) and sealed with epoxy (Epoxy Technology) and beveled to 45° or further sealed in epoxy and polished at 90° as noted. A Pt bipolar nanoelectrode was prepared by sealing a short piece of a Pt nanowire at the end of a glass micropipette. A ~2 cm length section of 25 μm Pt wire (99.95%, Alfa Aesar) was inserted into a 7.5 cm section of quartz capillary (OD 1.0 mm/ID 0.30 mm, Sutter Instrument Co.). In a two-step process, similar to the method previously described by this group for the preparation of conventional Pt nanodisk electrodes,[23] the quartz is first sealed around the Pt wire and then pulled into an ultra-sharp tip using a P-2000 Laser Puller (Sutter Instrument Co.). Borosilicate glass capillaries (OD 2.0mm/ID 1.16mm, Sutter Instrument Co.) were separately pulled in a P-97 Flaming/Brown Micropipette Puller (Sutter Instrument Co.) to a blunt tip of approximately 10 to 20 μm diameter which served as "holders" for the Pt electrodes and overall insulators between the two solutions. A quartz/Pt tip was then inserted into a borosilicate holder which was subsequently flame sealed around the inner quartz tip. A quick pulling motion of the quartz capillary back out of the outer borosilicate holder resulted in a small section of the quartz/Pt tip remaining behind. The outer end of the tip could then be broken off/cleaved using a scalpel or razorblade edge to create the desired bipolar electrode. Multiple BPEs could be obtained from a single quartz sealed Pt nanowire each slightly larger than the previous. The inside of the borosilicate capillary was then filled with the desired redox solution.

3.2.3 Cyclic Voltammetry.

A four-electrode, two-cell setup equipped with two working electrodes and two Ag/AgCl electrodes (Bioanalytical Sciences Inc.) was used in all series coupled bipolar

electrochemical experiments (see Figure 3.3a). Two AgCl-coated Ag wire quasi-reference electrodes were used for pipet-based bipolar nanoelectrodes. Cyclic voltammetry was carried out using a Chem-Clamp potentiostat (Dagan) connected to an EG&G 175 programmer. CV response was recorded using a PCI-6251(National Instruments) card on a Dell PC using in-house LabView 8.5 software (National Instruments). A scan-rate of 50 mV/s was used for all CV experiments unless noted otherwise.

3.2.4 Scanning Electron Microscopy.

Scanning Electron Microscopy (SEM) images were obtained using a field-emission microscope (FEI Sirion). Samples were sputter coated with a thin layer (2-3nm) of Au/Pd prior to imaging.

3.3 Results and Discussion

In the following sections several redox species are discussed in different series-coupled combinations. Table 3.1 provides a summary of experimental half-wave potentials and diffusion coefficients used for calculations and comparisons involving relative limiting factor.

3.3.1 CFEs as Closed Bipolar Electrodes.

A literature search regarding CFEs will not yield any mention of bipolar electrochemistry nor will one find a detailed discussion of the mechanism by which CFEs achieve conductivity when backfilled with an electrolyte solution. Figure 3.2a is a schematic diagram of a CFE, in which Fc is oxidized at the carbon disk and electrons flow through the fiber into the inner capillary. *The oxidation of Fc (or DA) must be balanced through the reduction of another redox species at the interior fiber due to electroneutrality, which makes*

CFE a good example of bipolar electrodes. We believe oxygen reduction reaction (ORR) may be responsible for the establishment of conductivity and therefore sought to investigate this further.

We have found that the CV response of a KCl-filled CFE can often be distorted with significant variability in the half-wave potential, $E_{1/2}$, for a given redox molecule. This behavior may be due to electrochemical limitations on the interior fiber. Figure 3.2b shows a typical CV of a 5-μm-diameter CFE beveled at a 45° angle in MeCN containing 5 mM Fc and 0.1 M $TBAPF_6$. A 3 M KCl solution is used to establish electrical conductivity (black). A sigmoidal CV response is obtained with a limiting current of 22 nA and an $E_{1/2}$ of 0.48 V vs Ag/AgCl. The blue CV is the response of another similarly prepared CFE in the same Fc solution. This CV shows a typical distortion seen with CFEs of this design: the current due to Fc oxidation increases much slower producing an $E_{1/2}$ almost 300 mV higher than the other electrode (black). An electrode with such response is often discarded in single-cell studies due to its slow behavior; however it is unclear what causes this slower response. In order to demonstrate the importance of understanding the faradaic process on the internal carbon, for the electrode whose CV is shown in black, the internal solution was replaced by 5 mM $Fe(CN)_6^{3-}$ with 0.1 M KCl (Figure 3.2b, red). This CV displays a similar sigmoidal response as the black curve; however, the $E_{1/2}$ has shifted nearly 250 mV negatively. We believe that the oxidation of Fc is now coupled to the reduction of ferricyanide which requires less external driving force than before.

We suggest that the outside carbon disk and the internal fiber are the anodic pole and the cathodic pole of a closed BPE, respectively. We also suggest that the reduction of oxygen is responsible for the reduction process at the cathodic pole for KCl-filled CFEs (*vide*

infra). In general, the overall voltammetric response of a CFE is determined by the size and shape of exterior carbon electrode and only weakly dependent on the interior fiber or the composition of the inner solution because the interior fiber is typically much greater than the outside. However, if the maximum faradaic current on the interior fiber becomes limited due to a smaller fiber length or the depletion of oxygen, the voltammetric response of the CFE may be significantly altered. In the next section, we show that oxygen reduction is not sufficient to keep up with the external reaction when the internal fiber is comparable to the external carbon in size. The addition of a fast redox mediator, e.g., $Fe(CN)_6^{3-}$, seems to be beneficial because it is easier to maintain a higher concentration and can decrease the overall applied voltage.

3.3.2 The Use of Closed Bipolar Cells Involving Two Microelectrodes.

There are two main difficulties in using a standard pipet-based CFE in this study. The first is the inherent challenge in controlling the size of the interior fiber and the second is the inability to completely replace the internal solution within the confines of the capillary. A simplified experimental setup was chosen which connects two separate two-electrode cells in series. A diagram of this setup is presented in Figure 3.3a. The two electrodes labeled WE1 and WE2 are used as the two ends of a closed bipolar cell. With this setup, the solution composition and the relative size of the poles can now be freely controlled.

Figure 3.3b is a comparison between the CV response of a 25-μm-diameter Au disk electrode (black) in 2 mM FcMeOH and 0.1 M Na_2SO_4 in a conventional one-compartment cell and that of the same electrode in a bipolar cell (red). In the bipolar setup, this electrode was connected to a 12.5-μm-diameter Au electrode placed in 5 mM $Fe(CN)_6^{3-}$ and 3 M KCl, as shown in Figure 3.3a. Although the electrode in the FcMeOH solution has a diameter

twice as large, the lower concentration of FcMeOH and smaller diffusion coefficient ($D \approx 0.67 \times 10^{-5}$ cm^2/s)[24] than ferricyanide ($D \approx 0.76 \times 10^{-5}$ cm^2/s)[25] result in a lower mass transfer rate to the larger electrode. Both CVs are therefore limited by the oxidation of FcMeOH on the 25-µm-diameter Au electrode. The $E_{1/2}$ of the bipolar setup is however 330 mV more negative than that in the conventional experiment. Similar to the analysis used by Dryfe and co-workers to study macroscopic electrodes, the $E_{1/2}$ of the bipolar microelectrode is directly related to the redox reactions on the two poles of the BPE and can be estimated from the difference in the formal redox potentials, $\Delta E°$,

$$E_{1/2} \approx \Delta E° = E°_c - E°_a \quad (1)$$

where $E°_c$ and $E°_a$ are the formal redox potentials for the cathode and anode, respectively. Because the formal potentials are generally close to the half-wave potentials for reversible processes,[26] one can also use $\Delta E_{1/2}$ to estimate the $E_{1/2}$ of a closed bipolar microelectrode. In this case, the oxidation of FcMeOH in 0.1 M Na_2SO_4 has an $E_{1/2}$ of 0.22 V vs Ag/AgCl while the reduction of ferricyanide occurs at 0.32 V vs Ag/AgCl (see Figure 3.4), which yields an expected $E_{1/2}$ of -0.10 V for the BPE as was observed in Figure 3.3b. As we will demonstrate later, additional factors must be considered to estimate the $E_{1/2}$ when the maximum limiting current on the two poles differ greatly.

The series-coupled bipolar setup was used to investigate the behavior of CFEs in the oxidation of DA and the role of ORR. To accomplish this, direct electrical connection was made to the interior fiber of a 5-µm-diameter CFE using Ag paste and a tungsten wire. This electrode was connected in series either to an identically prepared disk electrode to create a CF BPE with two equal area poles or to a 5-µm-diameter CF cylinder of variable length to create an electrode analogous to that shown in Figure 3.2a. Figure 3.5 shows the CV response

of an electrode of this design in an isotonic saline solution containing 100 μM DA and 1 mM $HClO_4$. The CVs obtained with the disk electrode connected in series to a 7-mm-length cylinder in 3 M KCl, both oxygen saturated and deaerated with argon (blue and red solid lines, respectively) show a very similar response to that of a setup using the directly connected electrode (black). Although the oxygen saturated solution requires a slightly lower driving potential than the others, the deaerated 3 M KCl solution still provides sufficient current to reach the same limiting current. When this electrode is connected in series to another 5-μm-diameter disk, the response (dotted lines) is significantly different. The combined detrimental effects of the smaller electroactive area as well as the lower oxygen concentration of the deaerated solution leads to insufficient reduction current on the cathodic pole producing a response that is now unrepresentative of the DA oxidation. The smaller cathodic pole is only capable of achieving a response limited by the DA oxidation at the anodic pole if the solution is oxygenated and a higher potential is applied (blue dotted line). With the larger cylinder electrode, the reduction of low concentrations of residual oxygen in solution and the presence of reducible contaminants provide a sufficient cathodic current. Figure 3.6 shows the CV response of the oxidation of DA coupled to the reduction of 5 mM ferricyanide using two 5 μm disks in series. This result further demonstrates that the electrochemical coupling between the DA oxidation and the reduction reactions plays an important role in the operation of KCl-filled CFEs. It is therefore important to understand and control the electrochemical limitations that exist at both poles of a BPE.

3.3.3 The Limiting Current and the $E_{1/2}$ of a Closed Bipolar Microelectrode.

In order to describe the limitations of the voltammetric response of a BPE, it is useful to first consider the diffusion-limited response of each pole separately. The diffusion-limited steady-state current, i_{ss}, of a planar microelectrode is described by the following equation,[27]

$$i_{ss} = 4nFDC^{*}r \quad (2)$$

where n is the number of electrons transferred per molecule, F is Faraday's constant (96485 C/mol), D is the diffusion coefficient, C^* is the bulk concentration of redox species, and r is the electrode radius. The overall voltammetric behavior of a bipolar microelectrode is expected to be dominated by the pole with a smaller predicted limiting current. This response would in fact be restricted by this "limiting pole". The other pole, capable of producing a greater current response will be called the "excess pole".

We have constructed a closed bipolar microelectrode by connecting two 25-μm-diameter Au disks in series in order to understand how its CV response depends on redox concentration. One pole is placed in a solution containing 5 mM ferricyanide and 3 M KCl while the other was in acetonitrile containing Fc of varying concentrations and 0.1 M $TBAPF_6$. Figure 3.7a shows several CVs corresponding to Fc oxidation on this bipolar microelectrode. Figure 3.7b shows the limiting current plotted as a function of Fc concentration. It can be seen that at concentrations ≤1 mM the limiting current increases linearly with Fc concentration as is predicted by Equation 2. In this region the anodic pole in the Fc solution limits the overall voltammetric response. Ferrocene has a larger diffusion coefficient ($D \approx 2.4 \times 10^{-5} cm^2/s$)[28] than ferricyanide and thus will require a lower concentration to achieve the same limiting current. When Fc concentration is greater than 1

mM the limiting current reaches a maximum at about 19.0 nA. This "upper limit" must therefore be restricted by the reaction occurring at the cathodic pole. The limiting current for a 25-μm-diameter disk electrode in 5 mM ferricyanide calculated from equation 2 is 18.4 nA. Experimentally this value was found to be slightly larger at 19.0 nA (Figure 3.4). Assuming we were using this BPE setup to study the oxidation of Fc or dopamine, we would be limited to measurements below 19.0 nA due to the limitations on the cathodic pole.

More interestingly, the change in Fc concentration has caused a noticeable shift in the position of the CV. The data presented in the inset of Figure 3.7b shows how the $E_{1/2}$ is dependent on the concentration of Fc. Such behavior has been previously discussed in great detail computationally by Stewart et al.[11] and by Dryfe and co-workers.[13] We chose to revisit the topic briefly here with micro- and nanoelectrodes and later extend the concept to $E_{1/2}$ shifts due to asymmetric BPE geometries, where one pole is larger than the other. As can be seen here with an increase in Fc concentration there is initially an increase in $E_{1/2}$ from 85 mV at 10 μM Fc to 133 mV at 1 mM followed by a decrease again to 71 mV for 5 mM Fc. The trend appears to be that as the ratio of the maximum capable limiting current for the two poles (i_{ss1}/i_{ss2}) as determined separately, approaches unity the half-wave potential for the BPE approaches its maximum value, which can be approximated by equation 1. The ratio i_{ss1}/i_{ss2} is not intended to imply that the current passing through the two poles is different, which is in fact not the case due to the necessity of coupled electron transfer. The ratio is instead used to compare the degree to which diffusion to one pole is limiting as compared to the other.

This behavior was further examined on the basis of asymmetric BPE geometries by changing the size of the limiting pole to demonstrate that the $E_{1/2}$ shift is not merely a function of concentration ratios alone. To this end one of the 25-μm-diameter Au electrodes

was replaced by Pt nanoelectrodes with radii from 1 to 830 nm. The Pt nanoelectrodes were placed in 5 mM Fc and the 25 μm Au electrode was kept in 5 mM $Fe(CN)_6^{3-}$ and 3 M KCl. Figure 3.7c shows the $E_{1/2}$ as a function of the radius of the Pt. For the smallest Pt disk an $E_{1/2}$ of -23 mV was found whereas the 830 nm electrode had an $E_{1/2}$ of +88 mV. The shift in the $E_{1/2}$ can be qualitatively explained by the following trend: an increase in the magnitude of the current demand at the limiting pole, with constant conditions at the excess pole, requires an increased voltage driving force. This translates to a requirement for a more positive potential to be applied to the anodic pole with respect to the cathodic pole. The extent to which this behavior was observed depended primarily on the initial response of the electrode used as the excess pole.

3.3.4 Secondary Reactions in the Voltammetric Response of Closed BPEs.

Normally only the pole with a smaller limiting current, or the limiting pole, can be studied from the overall voltammetric response. It is however possible to acquire information about both poles of a closed BPE from a single CV through the use of multiple redox species or "secondary" redox reactions. The series of CVs presented in Figure 3.8a illustrates this concept. The black and blue CVs correspond to a 25-μm-diameter and a 12.5-μm-diameter Au disk electrodes, respectively, both of which were obtained in an aqueous solution containing 2 mM $Fe(CN)_6^{3-}$/2 mM $Fe(CN)_6^{4-}$ and 1 M KCl in a conventional one-compartment cell. The limiting current for the 12.5-μm-diameter electrode is approximately half that of the 25 μm electrode as expected. These two cells were then connected in series to produce a closed bipolar microelectrode. The CV obtained from this setup is also shown in Figure 3.8a (red). Over the region of the scan from ~0.1 to 0.6 V the response reaches steady-state at a current, i_1, equal to that of the 12.5 μm pole where the oxidation of

ferrocyanide occurs. The reduction of ferricyanide on the 25 μm pole occurs at a rate less than its maximum capability at this point, making this the excess pole over this region of the CV. As the potential is swept beyond 0.7 V the response reaches a new higher-magnitude steady-state, i_2, equal to the steady-state response seen at the 25-μm-diameter disk alone. In this region it is clear that the 25-μm-diameter cathodic pole is now limiting, but this must then require a secondary process on the 12.5μm anodic pole to reach this elevated current. The second oxidation wave at approximately 0.7 V with respect to its ferricyanide couple would correspond to about 1.2 V vs NHE. It is likely that water oxidation ($2H_2O \rightarrow O_2 + 4H^+ + 4e^-$) with a standard redox potential of 1.229 V vs NHE is responsible for the process.[26] Figure 3.9 shows the CV response of a 25-μm-diameter Au disk electrode in the same ferricyanide/ferrocyanide mixture in a conventional setup. As the potential is swept above ~0.8 V the oxidation of water is observed by a large increase in current. In the bipolar experiment presented in Figure 3.8a this secondary reaction is limited only by the rate of the reduction of ferricyanide at the cathodic pole.

To investigate this behavior further we measured the CV response of a BPE composed of two 25-μm-diameter Au disks. One electrode was immersed in a solution of 5 mM ferricyanide and 3 M KCl and the other in 2 mM Fc and 0.1 M $TBAPF_6$ in MeCN. The CVs presented in Figure 3.8b were recorded after the ferricyanide solution was oxygen-saturated (black) and after it had been deaerated with nitrogen (red). Both CVs reached their limiting current of approximately 19 nA due to the reduction of 5 mM ferricyanide. The excess anodic pole in the Fc solution is capable of a limiting current ~1.3 times greater than that of the cathode pole due to the ratio of diffusion coefficients and concentrations of the two species. The reduction of O_2 must therefore be responsible for the additional wave in the

black curve, making the total current approximately 26 nA, now limited by the oxidation of Fc. Figure 3.10 shows an additional example in which a solution containing of a mixture of ferricyanide and hexaaammineruthenium(III) was used in series with a solution containing Fc. In the voltammogram two distinct waves with half-wave potentials of approximately -0.1 V and -0.65 V were observed, for the reductions of ferricyanide and hexaaammineruthenium(III), respectively. A third, less noticeable, wave can be seen at approximately -0.95 V corresponding to the ORR with an overall limiting current of 31 nA equal to what was observed for the diffusion-limited steady-state response of the Au electrode in 2 mM Fc for the conventional electrochemical cell configuration. The results shown in Figure 3.8 and Figure 3.10 have demonstrated that by using a second redox reaction both poles can be studied from a single CV scan.

3.3.5 Platinum Bipolar Nanoelectrodes.

Figure 3.11 shows a schematic of the experimental setup (a) and an optical micrograph (b) of one of the Pt bipolar nanoelectrodes. The voltammetric response of a BPE of this design filled with 2 mM Fc and 0.1 M $TBAPF_6$ and immersed in a solution of 5 mM ferricyanide and 3 M KCl is presented in Figure 3.11c. On the first half of the potential scan in the negative direction the voltammetric response is relatively featureless and reaches a steady-state current of approximately -350 pA until approximately -0.75 V where the current increases slightly. On the return scan two separate well defined waves can be seen with an overall shape similar to what was observed for the two 25-μm-diameter Au electrodes shown in Figure 3.8b. It appears that the wave between -0.4 to -0.2V is due to reduction of ferricyanide on the outer cathodic pole indicating a radius of approximately 210 nm of the external pole calculated from equation 2. At a potential from -0.4 V to -0.9 V it is believed

that the ORR occurs at the cathodic pole in addition to the reduction of ferricyanide. Previous studies on the reduction of oxygen with Pt electrodes have shown that the condition of the electrode surface and the starting potential of the scan greatly affect the ORR response.[29,30] With the potential held at a positive voltage an oxide layer forms on the Pt, which may hinder the reduction of oxygen. In the return scan in the positive direction the ORR can now occur at more positive potentials. The ORR, being an inner-sphere electrode reaction,[31] is more dependent on the condition of the electrode surface than the reduction of ferricyanide, an outer-sphere electrode reaction. Therefore, the wave due to ORR is more variable for the two scan directions.

The CV response of another pipet-based Pt BPE is shown in Figure 3.12a for the same solutions except in this case the aqueous side was either oxygen saturated or deaerated with nitrogen as noted. The CV for the oxygen saturated solution shows a sigmoidal response with a limiting current of approximately -1.2 nA. Upon deaeration the CV displays the double wave similar to that seen in Figure 3.11 with limiting currents of -0.9 nA and -1.15 nA for the lower and higher waves, respectively. It appears that oxygen remaining in solution is responsible for the second reduction wave. Figure 3.12b shows the CV of a conventional Pt nanoelectrode in 5 mM ferricyanide containing 3 M KCl. As expected the wave due to oxygen reduction can be seen in this CV as well, with the ORR occurring at a more negative potential on the initial sweep in the negative direction. Figure 3.13 shows two additional examples of pipet-based Pt BPEs and their CVs along with corresponding SEM images. In both cases the electrode radii calculated from the CVs' distinct steady-state regions using Equation 2 agree well to the dimensions measured from the corresponding SEM micrographs for the exterior poles.

3.4 Conclusions

We have shown that carbon-fiber microelectrodes are closed BPEs when backfilled with an electrolyte to establish conductivity. The direct coupling between the oxidation of redox species, e.g., dopamine, on the carbon disk and the reduction of soluble oxygen on the inner fiber is likely to be responsible for the conductivity. The voltammetric response of micro- and nanoscale BPEs differ considerably from the response of comparable conventional electrodes. Factors that affect not only the magnitude but also the position and shape of this response include the presence of varying degrees of an excess of redox molecule at one pole as compared to the other and asymmetric pole size. We have demonstrated the ability to obtain, from a single voltammogram, quantitative measurements of the properties of both the poles of a bipolar microelectrode. This process required the use of secondary reactions such as the ORR or the presence of additional redox species. Finally we have described the preparation and use of Pt bipolar nanoelectrodes.

3.5 Tables and Figures

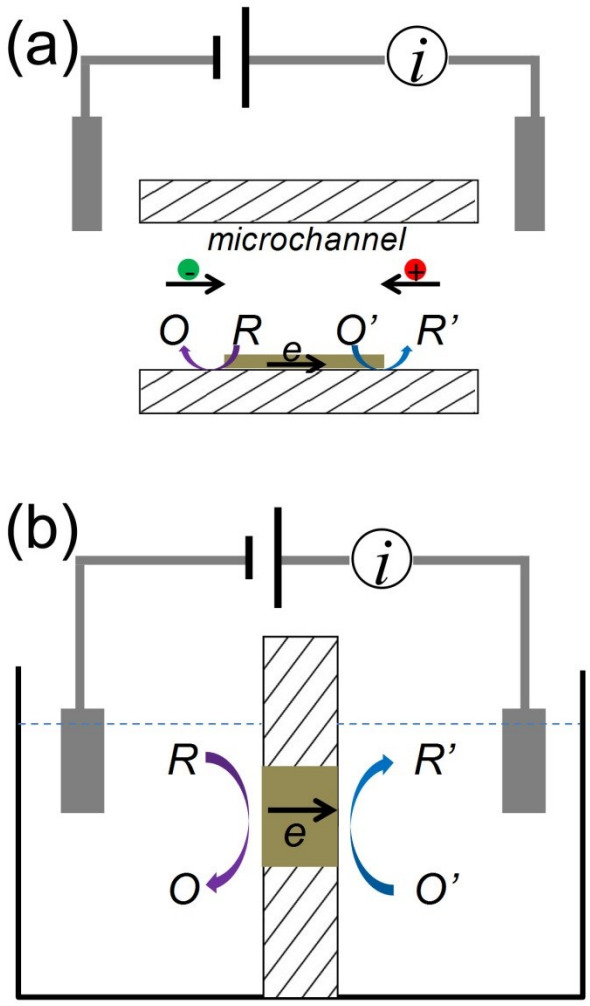

Figure 3.1 Open versus closed bipolar electrode cell.
A comparison of an open bipolar cell (a) and a closed bipolar cell (b).

Table 3.1 Diffusion Coefficients and Experimental Half-Wave Potentials for Select Redox Species.

Redox Species	*Supporting Electrolyte/Buffer/ Solvent*	*Half-Wave Potentials (vs Ag/AgCl)*	*Diffusion Coefficient(D) ($10^5 D/cm^2 s^{-1}$)*	*Ref.† for D*
Fc	0.1 M $TBAPF_6$/MeCN	0.48	2.4	32
FcMeOH	0.1 M Na_2SO_4/aq.	0.22	0.67	33
$Fe(CN)_6^{3-}$	1M KCl/aq.	0.32	0.76	34
$Fe(CN)_6^{4-}$	1M KCl/aq.	0.32	0.63	34
DA	1 mM $HClO_4$/ isotonic saline/aq.	Variable	0.665	35
H_2O	-	1.007 (E° for oxidation)	-	36 (for E°)
O_2	3 M KCl/aq.	Variable	1.75	37

†Diffusion coefficients from literature are in similar yet different media than used here.

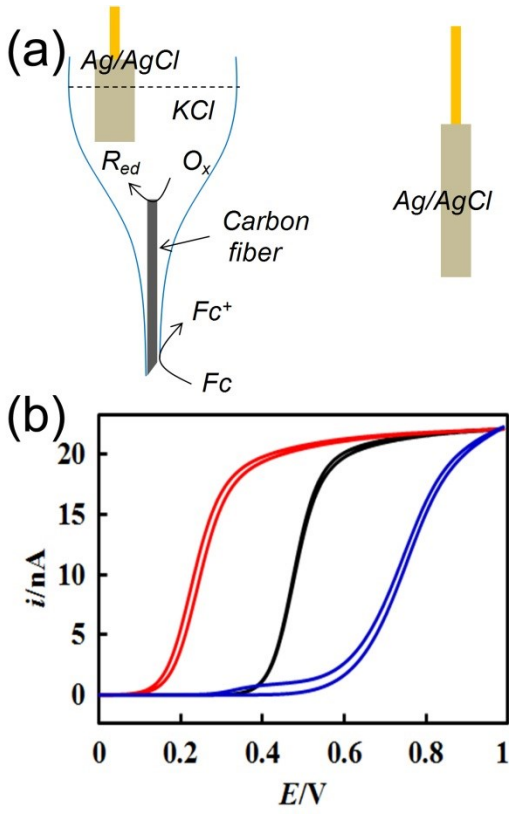

Figure 3.2 Carbon fiber electrodes as closed BPEs.
(a) A schematic diagram of a CFE being used to study the oxidation of Fc. A KCl solution is used to establish the conductivity in the capillary. (b) Voltammetric response of a 5-μm-diameter CFE in 5 mM Fc, 0.1 M TBAPF6 in MeCN. Electrical conductivity inside of the CFE was made with 3 M KCl (black) and 5 mM $Fe(CN)_6^{3-}$ in 0.1 M KCl (red). The blue CV was obtained from a second CFE with 3 M KCl on the inside showing a typical distortion.

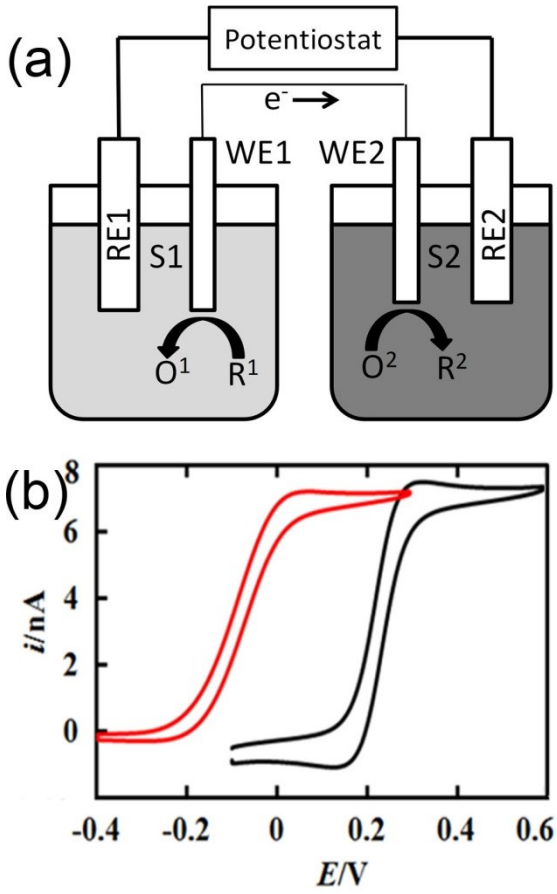

Figure 3.3 Series-coupled BPE configuration.
(a) Schematic showing the simplified cell configuration of a closed bipolar microelectrode. (b) Cyclic voltammetric response of a 25-µm-diameter Au electrode in 2 mM FcMeOH in 0.1 M Na2SO4. The black CV shows the oxidation of FcMeOH on the 25-µm- diameter Au electrode with a conventional one-compartment cell versus a Ag/AgCl reference electrode. The red CV was obtained on the same electrode using a closed bipolar cell as shown in (a). A 12.5-µm-diameter Au electrode in 5 mM $Fe(CN)_6^{3-}$, 3 M KCl was used for the second compartment.

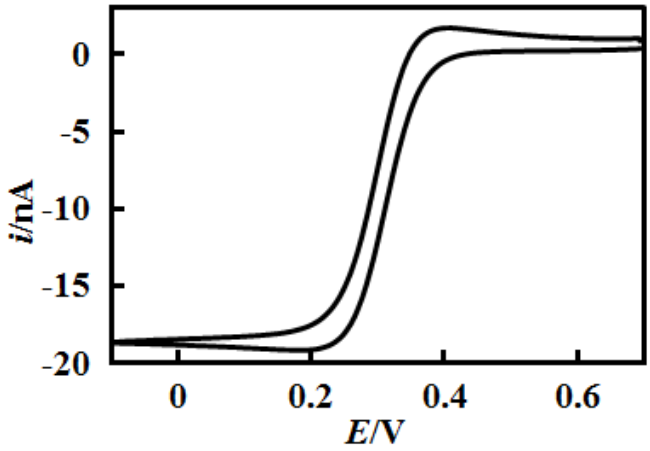

Figure 3.4 CV of 25 µm Au electrode in ferricyanide.
Cyclic voltammogram of the 25-µm-diameter Au disk electrode in a solution containing 5 mM Ferricyanide and 3 M KCl in a conventional one-compartment two-electrode cell. This electrode and solution was connected in series with another 25-µm-diameter Au disk electrode to produce the CVs presented in Figure 3.3.

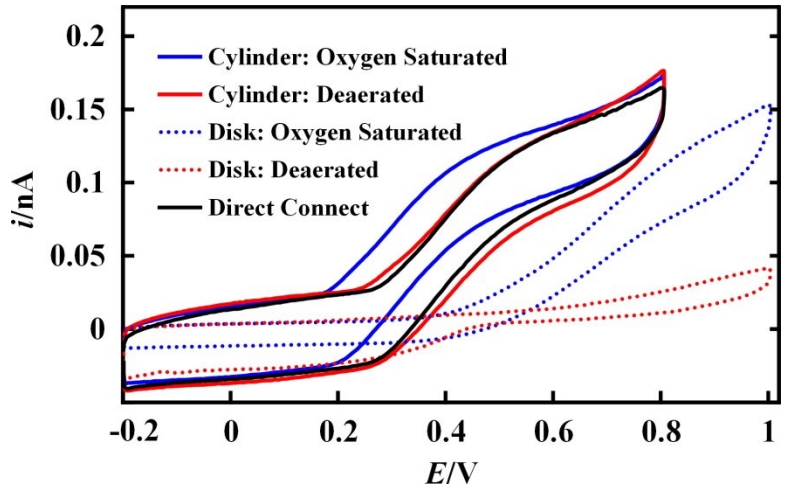

Figure 3.5 The role of ORR in voltammetric response of carbon fiber electrode.
Cyclic voltammograms showing the oxidation of DA at a 5-µm-diameter CF disk in a series-coupled bipolar configuration similar to Figure 3.3a. The cathodic pole was a 5-µm-diameter CF cylinder of 7 mm in length (solid lines, red and blue) or another 5-µm-diameter CF disk (dotted lines, blue and red) in a solution containing 3 M KCl. The black trace shows the response when the CF is directly connected to the working electrode lead using silver paste and a tungsten wire.

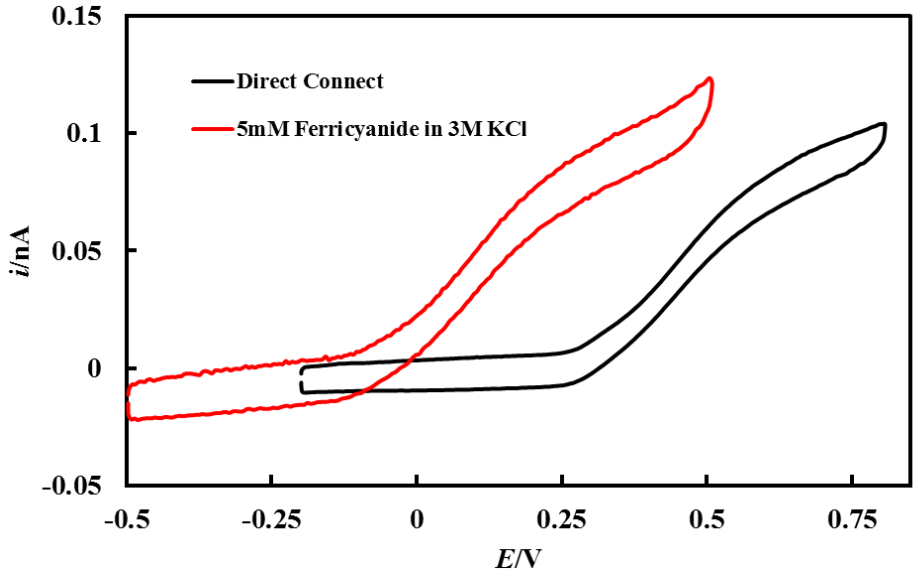

Figure 3.6 DA oxidation at CF electrode.
Cyclic voltammogram for the oxidation of 100 µM DA with 1 mM HClO4 in isotonic saline at a 5-µm-diameter CF disk electrodes coupled in series to a second 5-µm-diameter CF disk in a solution of 5 mM Ferricyanide in 3 M KCl (red). For comparison the response of the same CFE was measured when connection was directly made to the driving electrode (black). CVs were recorded at 20 mV/s.

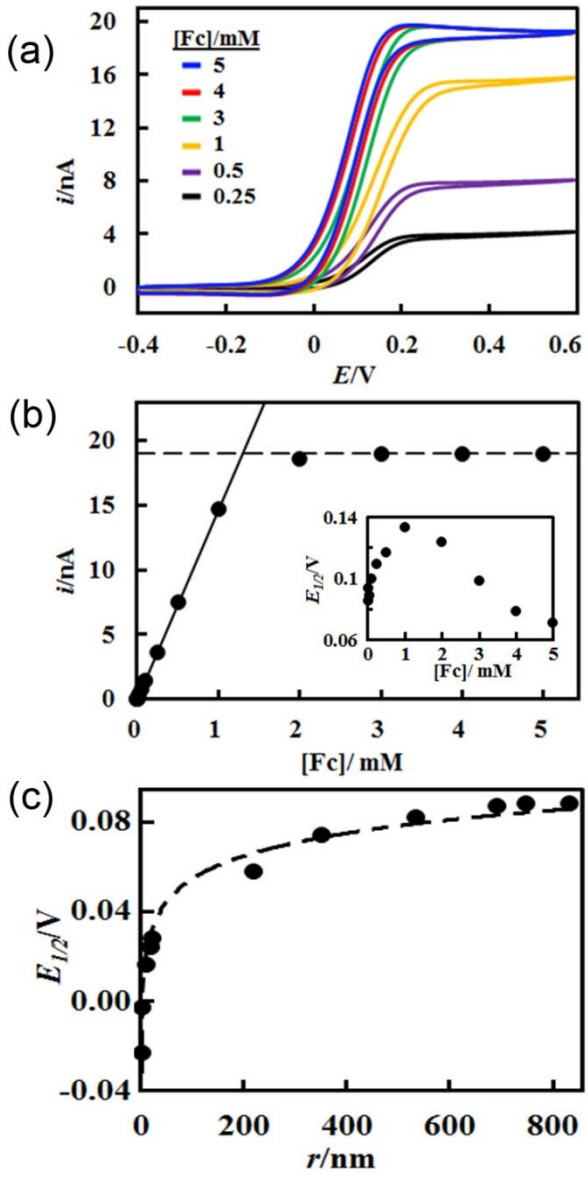

Figure 3.7 Shift in BPE half-wave potential.
(a) CVs of Fc oxidation on a 25-µm-diameter Au closed bipolar microelectrodes as a function of Fc concentration. The other pole was a 25-µm-diameter Au disk in a solution containing 5 mM Fe(CN)63- and 3 M KCl. (b) The limiting current of Fc oxidation plotted versus concentration of Fc from data shown in (a). Solid line in (b) is linear portion where limiting current can be used to determine electrode/solution information on Fc side. Dashed line shows limiting current on ferricyanide side above which information is no longer obtained about the Fc side. Inset (b) is the half-wave potential for the forward scan as a function of concentration of Fc. (c) $E_{1/2}$ as a function of Pt nanoelectrode radius for a closed bipolar setup in which a Pt nanoelectrode in MeCN containing 5 mM Ferrocene, 0.1 M $TBAPF_6$ is connected to a 25-µm-diameter Au disk electrode in 5 mM $Fe(CN)_6^{3-}$ and 3 M KCl.

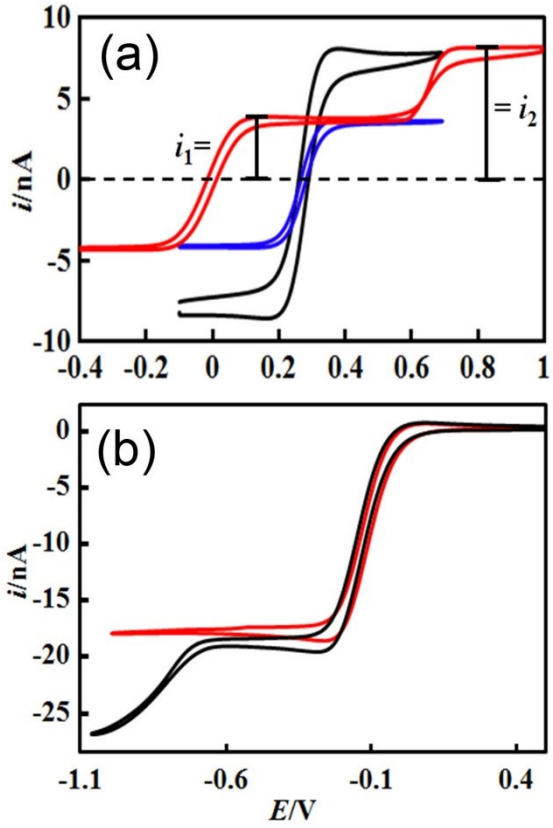

Figure 3.8 Characterization of both poles of a BPE.
(a) CVs of Au microelectrodes in 2 mM Fe(CN) 63- /2 mM Fe(CN)64- . The black CV is a 25-μm-diameter while the blue CV is a 12.5-μm-diameter electrode, both in a conventional one-compartment cell. The red trace was obtained by connecting the cells containing these two electrodes in series to form a closed bipolar cell as in Figure 3.3a. At a potential between 0 and 0.6 V, i_1 is limited on the 12.5 μm pole by the oxidation of ferrocyanide. Above 0.7 V i_2 is limited on the 25 μm pole by the reduction of ferricyanide with the oxidation of H_2O compensating for the limitation on 12.5 μm pole. (b) CVs of a closed bipolar cell containing two 25 μm Au electrodes in series, one in 5 mM $Fe(CN)_6^{3-}$ and 3 M KCl and the other in MeCN containing 2 mM Fc and 0.1 M $TBAPF_6$. The wave at -0.1 V is due to the reduction of $Fe(CN)_6^{3-}$. The CV in red was recorded after the solution was bubbled with N_2. The black curve (recorded after O_2 saturation) shows ORR makes up for the limitation on the ferricyanide side to give a response limited by Fc oxidation below -1 V.

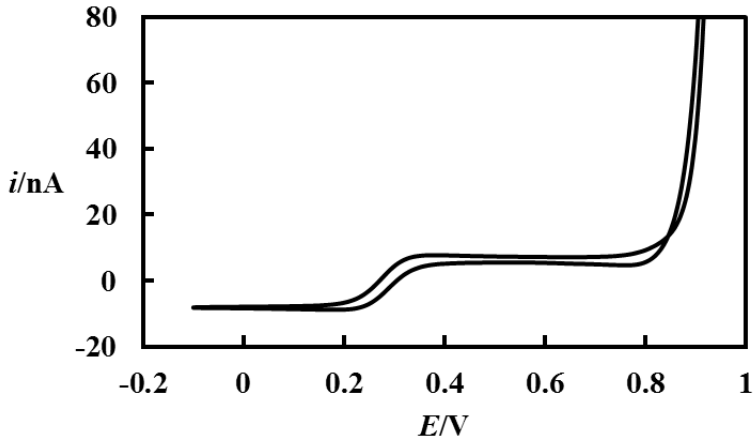

Figure 3.9 Water oxidation at Au electrode in ferri-/ferrocyanide solutions.
Cyclic Voltammogram of a 25-µm-diameter Au disk electrode in 2 mM $Fe(CN)_6^{3-}$/2 mM $Fe(CN)_6^{4-}$ containing 1 M KCl. As the potential is swept above ~0.8V vs Ag/AgCl the oxidation of water begins to occur.

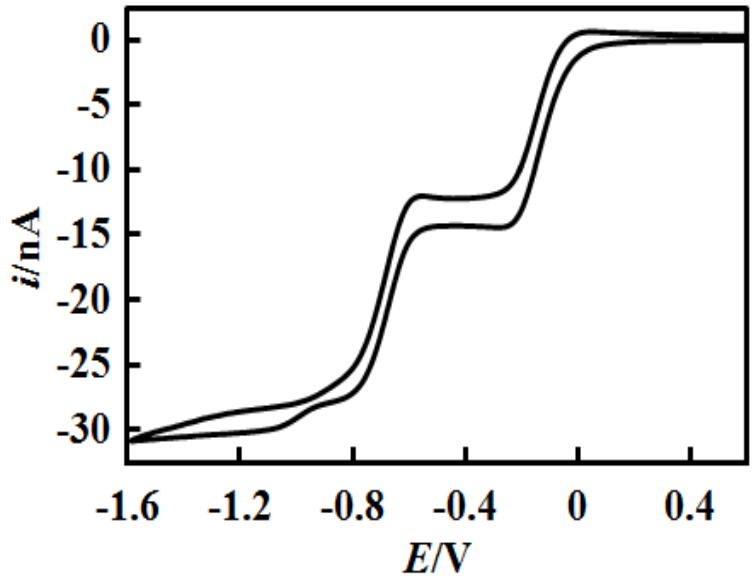

Figure 3.10 Response of BPE in multicomponent solutions.
Cyclic voltammogram of a closed bipolar cell composed of two 25-μm-diameter Au electrodes in series, one in MeCN containing 2 mM Fc, 0.1 M TBAPF6 and the other in a solution containing a mixture of 5 mM $Fe(CN)_6^{3-}$ and 5 mM $Ru(NH_3)_6^{3+}$ containing 3 M KCl. The two reduction waves at -0.1 V and -0.65 V are due to the reduction of $Fe(CN)_6^{3-}$ and $Ru(NH_3)_6^{3+}$, respectively. A third wave at -0.95 V is due to the reduction of oxygen. This solution is not stable. An orange precipitate began to form shortly after the solution was made decreasing the effective concentrations of the two redox species.

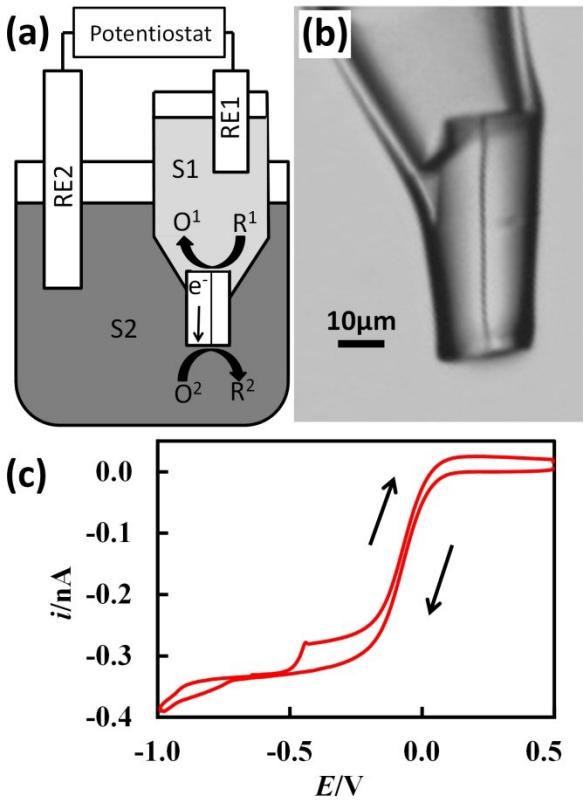

Figure 3.11 Pt nano-bipolar electrode response.
Schematic showing cell design (a) and optical micrograph (b) of a pipet-based Pt bipolar nanoelectrode. (c) Voltammetric response of a Pt bipolar nanoelectrode with 2 mM Fc, 0.1 M TBAPF6 in MeCN on the inside of the pipet and 5 mM Fe(CN)63- in 3 M KCl on the outside.

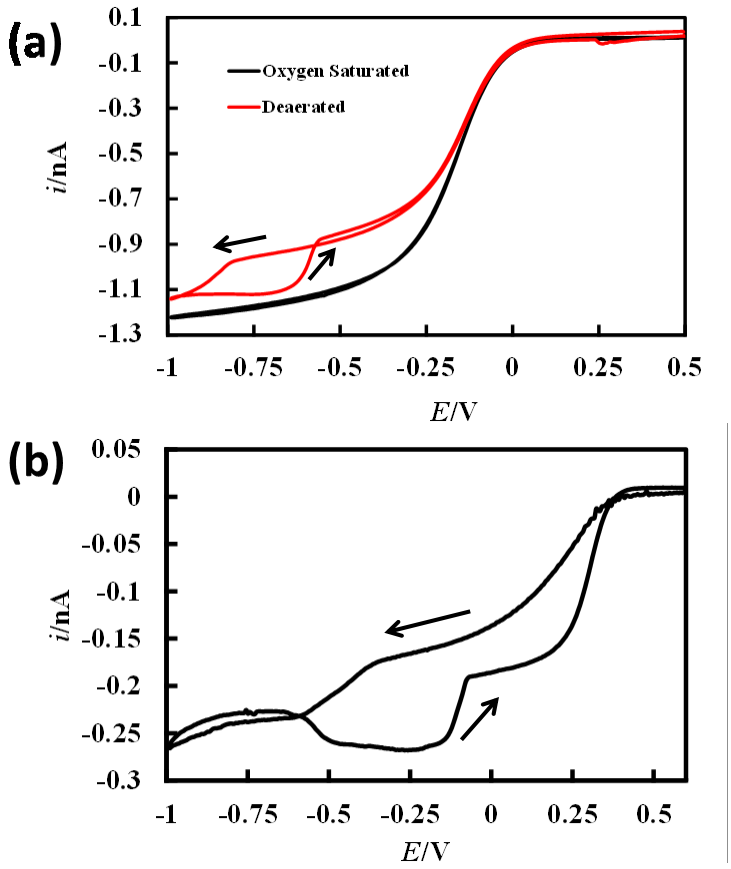

Figure 3.12 Response of Pt electrodes in ferricyanide solutions.
(a) Voltammetric response of a pipet-based Pt bipolar ultra-microelectrode. CVs were recorded with 2 mM Fc, 0.1 M TBAPF6 in MeCN on the inside of the pipet and 5 mM $Fe(CN)_6^{3-}$ in 3 M KCl on the outside. (b) Voltammetric response of a conventional Pt nanoelectrode in 5 mM $Fe(CN)_6^{3-}$ containing 3 M KCl.

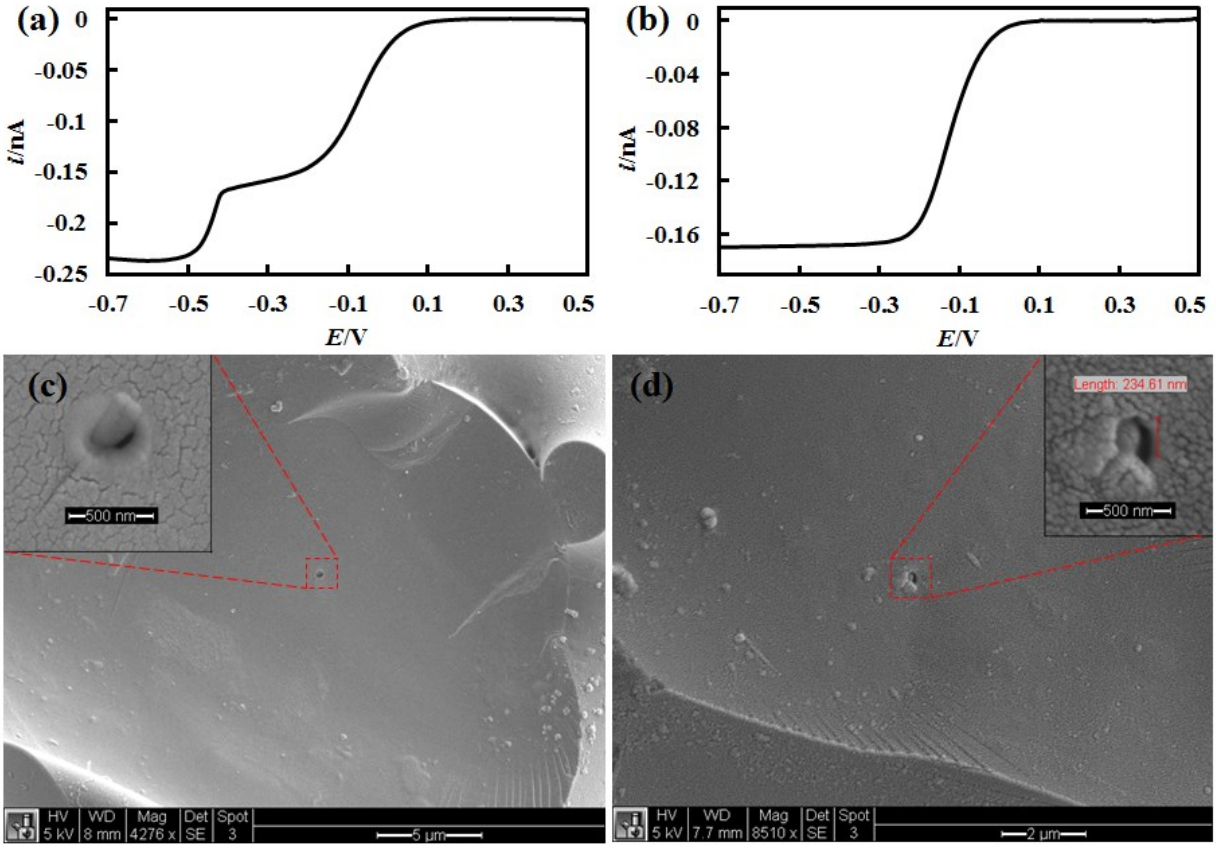

Figure 3.13 Comparison of Pt bipolar nanoelectrode CVs with SEM images.
Voltammetric response (a) and (b) of two pipet-based Pt bipolar nanoelectrodes whose tips are shown in SEM (c) and (d) respectively. Only the forward CV scan is shown for clarity. CVs were recorded with 2 mM Fc, 0.1 M TBAPF6 in MeCN on the inside of the pipet and 5 mM $Fe(CN)_6^{3-}$ in 3 M KCl on the outside. The steady-state current of the first wave in panel (a) corresponds to an electrode with a radius of 115 nm on the exterior. This is in fairly good agreement with the radius as measured from the SEM image for the exterior of this electrode (c) inset. Although the CV shows a clear second wave (which would correspond to a disk of 126-nm-radius on the interior) it cannot be confidently used as there is no clear indication of which pole and process the upper limit is set by. The steady-state current observed in the voltammogram in panel (b) of 170 pA corresponds to an electrode radius of 115 nm which again corresponds very well to the 235-nm-diameter measure from the SEM of this tip in panel (d) inset. No second wave was seen with this voltammogram.

3.6 References

(1) Mavre, F.; Anand, R. K.; Laws, D. R.; Chow, K. F.; Chang, B. Y.; Crooks, J. A.; Crooks, R. M. *Anal.Chem.,* **2010,** *82*, 8766-8774.

(2) Loget, G.; Kuhn, A. *Anal. Bioanal.Chem.,* **2011,** *400,* 1691-1704.

(3) Chow, K. F.; Chang, B. Y.; Zaccheo, B. A.; Mavre, F.; Crooks, R. M. *J. Am. Chem. Soc.,* **2010,** *132*, 9228-9229.

(4) Arora, A.; Eijkel, J. C. T.; Morf, W. E.; Manz, A. *Anal. Chem.,* **2001,** *73*, 3282-3288.

(5) Mavre, F.; Chow, K. F.; Sheridan, E.; Chang, B. Y.; Crooks, J. A.; Crooks, R. M. *Anal. Chem.,* **2009,** *81*, 6218-6225.

(6) Chang, B. Y.; Mavre, F.; Chow, K. F.; Crooks, J. A.; Crooks, R. M. *Anal. Chem.,* **2010,** *82*, 5317-5322.

(7) Chow, K. F.; Mavre, F.; Crooks, R. M. *J. Am. Chem. Soc.,* **2008,** *130*, 7544-7545.

(8) Perdue, R. K.; Laws, D. R.; Hlushkou, D.; Tallarek, U.; Crooks, R. M. *Anal. Chem.,* **2009,** *81*, 10149-10155.

(9) Ndungu, P. G. Ph.D. Thesis, Drexel University, Philadelphia, PA, 2004.

(10) Plana, D.; Jones, F. G. E.; Dryfe, R. A. W. *J. Electroanal. Chem.,* **2010,** *646*, 107-113

(11) Stewart, A. A.; Campbell, J. A.; Girault, H. H.; Edddowes, M. *Ber. Bunsen Phys. Chem.,* **1990,** *94*, 83-87.

(12) Hotta, H.; Akagi, N.; Sugihara, T.; Ichikawa, S.; Osakai, T. *Electrochem. Comm.,* **2002,** *4*, 472-477.

(13) Plana, D.; Shul, G.; Stephenson, M. J.; Dryfe, R. A. W. *Electrochem. Comm.,* **2009,** *11*, 61-64.

(14) Zhang, B.; Adams, K. L.; Luber, S.; Heien, M., Ewing, A. G. *Anal. Chem.* **2008**, *80*. 1394-1400.

(15) Keithley, R. B.; Carelli, R. M.; and Wightman, R. M. *Anal. Chem.,* **2010**, *82*, 5541-5551.

(16) Amatore, C.; Arbault, S.; Bouret, Y.; Guille, M.; Lemaitre, F.; Verchier, Y. *Anal. Chem.,* **2009**, *81*, 3087– 3093

(17) Sombers, L. A.; Hanchar, H. J.; Colliver, T. L.; Wittenberg, N.; Cans, A.; Arbault, S.; Amatore, C.; and Ewing, A. G. *J. Neurosci.*, **2004**, *24*, 303-309.

(18) Bruns, D. *Methods*, **2004**, *33*, 312-321.

(19) Heien, M.; Johnson, M.; Wightman, R. *Anal. Chem.,* **2004**, *76*, 5697– 5704

(20) Ge, S.; White, G. J.; Haynes, C. L. *Anal. Chem.,* **2009**, *81*, 2935-2943.

(21) Takmakov, P.; Zachek, M. K.; Keithley, R. B.; Walsh, P. L.; Donley, C.; McCarty, G. S.; Wightman, R. M. *Anal. Chem.,* **2010**, *82*, 2020-2028.

(22) Adams, K. L.; Jena, B. K.; Percival, S. J.; Zhang, B. *Anal. Chem.,* **2011**, *83*, 920-927.

(23) Li, Y.; Bergman, D.; Zhang, B. *Anal. Chem.,* **2009,** *81*, 5496-5502.

(24) Anicet, N.; Bourdillon, C.; Moiroux, J.; and Saveant, J-M. *J. Phys. Chem. B,* **1998**, 102, 9844–9849.
(25) Stackelberg, M. von; Pilgram, M.; and Toome, W. Z. *Elektrochem.*, **1953**, *57*, 342-350.
(26) Bard, A. J.; Faulkner, L. R. *Electrochemical Methods*. 2nd ed.; John Wiley & Sons: New York, 2001.
(27) Saito, Y. *Rev. Polarogr*., **1968**, *15*, 177-182.
(28) Bond, A. M.; Henderson, T. L. E.; Mann, D. R.; Mann, T. F.; Thormann, W.; and Zoski, C. G. *Anal. Chem.*, **1988**, *60*, 1878-1882.
(29) Damjanovic, A.; Hudson, P. G., *J. Electrochem. Soc.* **1988,** *135*, 2269-2273.
(30) Zoski, C. G.; Fernandez, J. L.; Imaduwage, K.; Gunasekara, D.; Vadari, R., *J. Electroanal. Chem.* **2011,** *651*, 80-93.
(31) Bard, A. J. *J. Am. Chem. Soc.,* **2010**, *132*, 7559-7567.
(32) Bond, A. M.; Henderson, T. L. E.; Mann, D. R.; Mann, T. F.; Thormann, W.; and Zoski, C. G. *Anal. Chem.*, **1988**, 60, 1878-1882.
(33) Anicet, N.; Bourdillon, C.; Moiroux, J.; and Saveant, J-M. *J. Phys. Chem. B,* **1998**, 102, 9844–9849.
(34) Stackelberg, M. von; Pilgram, M.; and Toome, W. Z. *Elektrochem.*, **1953**, *57*, 342-350.
(35) Hsieh, S.; Jorgenson, J.W. *Anal. Chem.,* **1996**, *68,* 1212–1217.
(36) Bard, A. J.; Faulkner, L. R. *Electrochemical Methods*. 2nd ed.; John Wiley & Sons: New York, 2001.
(37) Ikeuchi, H.; Hayafuji, M.; Aketagawa, Y.; Taki, J.; Sato, G. P., *J. Electroanal. Chem.,* **1995**, *396*, 553-556.

CHAPTER 4
Steady-State Voltammetry of a Microelectrode in a Closed Bipolar Cell*

4.1 Introduction

Bipolar electrochemistry has emerged as a useful tool for a number of important analytical applications, [1] such as electroanalysis,[2-7] separation,[8] preconcentration,[9-11] and neurochemical sensing using carbon-fiber microelectrodes.[12] In addition, bipolar electrochemistry mechanisms have been utilized in industrial processes for many decades.[13,14] Other recent applications of bipolar electrochemistry include synthesis and manipulation of nanomaterials,[15-18] and fast screening of electrocatalysts.[19] A unique aspect of bipolar electrochemistry is that it uses an electrode with opposite polarity on two ends to allow for direct coupling of two different redox reactions. In a conventional two or three-electrode electrochemical cell, one focuses primarily on electrochemical reactions at the working electrode. The reference and counter electrodes function only to provide a reference potential and balance the current on the working electrode. The counter electrode is usually sufficiently large so that it does not limit the faradaic process on the working electrode. A bipolar electrochemical cell, on the other hand, involves two separate electrochemical interfaces coupled directly on a bipolar electrode (BPE). A pair of driving electrodes (usually much greater than the bipolar electrodes) supplies the voltage needed to

---

* This chapter is adapted with permission from Cox, J. T.; Guerrette, J. P. & Zhang, B. Steady-State Voltammetry of a Microelectrode in a Closed Bipolar Cell. *Anal. Chem.* **2012**, 84, 8797-8804.

drive the electrochemical reactions on the BPE. The overall electrochemical response of the BPE could thus be limited by both poles.

Electroanalytical studies involving BPEs have mainly been carried out using open BPEs. A typical open BPE cell uses a microfluidic channel to host a conductive microelectrode. A voltage bias is applied along the length of the microchannel from a pair of driving electrodes allowing two coupled electrochemical reactions to occur at each of the poles of the BPE. Open BPEs have been especially useful for performing wireless electrochemistry in a microfluidic environment.[1] We[20] and others[21,22] have recently discussed series-coupled electrochemical reactions on closed BPEs. As shown in Figure 4.1a, a closed BPE cell contains two separate compartments connected via a metallic wire electrode. The electrochemical current on the closed BPE can be directly measured due to the lack of the microchannel and ionic current path. A closed BPE is analogous to two electrochemical cells connected in series as depicted in Figure 4.1b. In this configuration, the faradaic reaction occurring on the disk electrode is electrochemically coupled to the reaction on the large cylinder electrode. By our convention we refer to the pole where the limiting process occurs as the limiting pole and the other as the excess or coupling pole.[20]

As an important application of closed bipolar setup, one can make direct electrochemical current-voltage recordings on a microelectrode without the need to make direct electrical wire contact to the electrode. This is, in many cases, preferable to significantly simplify experimental procedures. For example, one can use a bipolar setup to measure electrochemical response of single nanowires[20] and their arrays prepared in an insulating membrane. Additionally, carbon-fiber microelectrodes (CFEs),[23-25] when a salt

solution is used to establish electrical continuity, use a closed bipolar mechanism to detect fast changes in catecholamine concentration. [20]

Although a microelectrode can be used in a closed bipolar setup to make direct electrode recordings, its electrochemical behavior can be quite different from its "normal" behavior in a two or three-electrode setup. For example, in a previous study we have shown that the voltammetric response of a microelectrode in a closed bipolar cell is related to the properties of the excess pole with a shift in the response as a function of the difference in formal potentials of both poles. Additionally, there is a clear dependence of the half-wave potential on the redox concentration at, and relative size of the excess pole.[20] However, in this previous report we did not reach a quantitative understanding of this relationship. In order to fully extend the potential use of BPEs for fundamental electrochemical studies as well as key bioanalytical applications, it becomes critical to develop a more comprehensive understanding of the steady-state voltammetric response of a microelectrode in a closed bipolar setup.

In this work, we discuss the theory to quantitatively describe the steady-state voltammetry of closed bipolar microelectrodes. We focus our attention on the steady-state voltammetry of a microelectrode used as a limiting pole of a BPE and how it is affected by the processes occurring at the excess pole. We show that the voltammetric response can be readily expressed by considering the individual responses of both poles separately in conventional two or three-electrode configurations and that the wave shape depends strongly on the ratio of the limiting currents of both individual poles. We have also provided experimental results to support our theoretical prediction. Additionally, we discuss methods to obtain a fast and nearly reversible voltammetric response from a microelectrode when

used in a closed bipolar electrochemical configuration. These methods could be useful for improving performance of microscale BPEs such as CFEs routinely used for quantitative analysis in biological systems.

4.2 Theory

In order to understand the voltammetric response of a microelectrode in a closed bipolar cell, it is beneficial to first consider the steady-state response of individual poles. Under simple mass-transport control, the reversible voltammetric response of a microelectrode in a conventional two-electrode cell can be readily expressed by the following equation,[26]

$$E = E^{o'} + \frac{RT}{nF}\ln\frac{D_O}{D_R} - \frac{RT}{nF}\ln\left(\frac{i_{ss} - i}{i}\right) \quad (1)$$

where E and $E^{O'}$ are the applied electrode potential and the formal potential for a simple n-electron redox reaction, $R_{ed} \rightarrow O_x + ne^-$, R is the gas constant, T is the absolute temperature, n is the number of electrons transferred per redox molecule, D_R and D_O are the diffusion coefficients for the redox species R_{ed} and O_x, respectively, i is the faradaic oxidation current at voltage E, and i_{ss} is the steady-state limiting current. In our experiments the microelectrodes have inlaid disk geometry, and the limiting current is given by,[27]

$$i_{ss} = 4nFDC^*r \quad (2)$$

where C^* is the concentration of redox species in the bulk and r is the radius of the microelectrode. Assuming the diffusion coefficients of the R_{ed} and O_x are approximately the same, equation (1) is further simplified as,

$$E = E^{o'} - \frac{RT}{nF}\ln\left(\frac{i_{ss} - i}{i}\right) \tag{3}$$

A closed bipolar electrode allows one to couple two electrochemical reactions such that the faradaic currents on the anodic pole and the cathodic pole have the same magnitude and opposite sign due to electroneutrality. Additionally, the overall bias voltage across the BPE is equal to the difference in the applied potentials on both poles.[20] This voltage can thus be expressed by combining the equations (3) for both cathodic pole and the anodic pole,

$$E = E_a - E_c = \left(E_a^{o'} - E_c^{o'}\right) + \frac{RT}{F}\left\{\frac{1}{n_a}\ln\left(\frac{i_a}{i_{ss}^a - i_a}\right) - \frac{1}{n_c}\ln\left(\frac{i_{ss}^c - i_c}{i_c}\right)\right\} \tag{4}$$

where i_{ss}^a and i_{ss}^c are the limiting currents on the anodic pole and the cathodic pole, and $E_a^{o'}$ and $E_c^{o'}$ are the formal potentials for the reactions on the anodic and cathodic poles, respectively. *Here, we define the anodic current as positive and cathodic current as negative current.* Because of electroneutrality in a closed bipolar cell, the magnitude of the oxidation current on the anodic pole should be equal to that of the reduction current on the cathodic pole, or, $i = i_a = -i_c$. By further assuming both reactions are 1-electron processes, equation (4) becomes,

$$E = \left(E_a^{o'} - E_c^{o'}\right) + \frac{RT}{F}\left\{\ln\left(\frac{i}{i_{ss}^a - i}\right) + \ln\left(\frac{-i}{i_{ss}^c + i}\right)\right\} \quad (5)$$

Equation (5) now shows a more complicated relationship between the total current *i* and the voltage across the bipolar electrode, which is closely dependent on the limiting currents of both poles. Several important conclusions can be drawn from equation (5). First, the limiting current on the bipolar electrode will be limited by the pole with smaller limiting current. If i_{ss}^a is smaller than $-i_{ss}^c$, the anodic pole will be the limiting pole and the limiting current of the BPE will be i_{ss}^a. Furthermore, the $E_{1/2}$ can be derived from equation (5),

$$E_{1/2} = \left(E_a^{o'} - E_c^{o'}\right) - \frac{RT}{F}\ln\left(-2\left(\frac{i_{ss}^c}{i_{ss}^a}\right) - 1\right) \quad (6)$$

Equation (6) indicates that the $E_{1/2}$ not only depends on the difference of the formal potentials but is also closely related to the ratio of the limiting currents. The greater the ($-i_{ss}^c / i_{ss}^a$), the more the *i*-*V* response would shift negatively on the potential axis.

Additionally, the steady-state *i*-*V* response of a microelectrode in a closed bipolar setup can now be predicted from equations (4) and (5). Let us first consider a case where we have a simple $1e^-$ oxidation process, $R_{ed} \rightarrow O_x + 1e^-$, coupled to its corresponding reduction process. Since they are complimentary reactions, their formal potentials are the same. As such, equation (5) becomes

$$E = \frac{RT}{F}\left(\ln\left(\frac{i}{i_{ss}^{a} - i}\right) + \ln\left(\frac{-i}{i_{ss}^{c} + i}\right)\right) \tag{7}$$

Figure 4.2a shows three predicted *i*-*V* responses assuming the limiting current on the cathodic pole is 1, 10, and 100 times of that on the anodic pole. Also shown in Figure 4.2a is the *i*-*V* response of the anodic pole in a conventional two-electrode setup. This *i*-*V* response has been generated assuming a 0-V formal potential for simplicity and easy comparison of the bipolar *i*-*V* responses. All the current in Figure 4.2 has been normalized to the limiting current on the anodic pole for easy comparison.

One can immediately see that when compared to the *i*-*V* response in a conventional two-electrode setup, all bipolar *i*-*V* responses have similar sigmoidal shape. *However, the bipolar responses clearly show a slower current increase with voltage.* The 1:1 current ratio gives the slowest current increase and requires a higher applied voltage to reach steady-state. We believe that this apparent wave broadening or slower *i*-*V* response is solely due to additional energy (or voltage) requirement to drive the second faradaic reaction on the excess pole. The higher the cathodic limiting current, the faster the current increases with voltage. We can anticipate that when the cathodic steady-state limiting current is much higher than that on the anodic pole, the overall *i*-*V* response would resume the reversible shape of the CV in the conventional two-electrode setup. Figure 4.2a also shows a clear negative shift of the $E_{1/2}$ of the bipolar response as the ratio of the limiting currents increases, which is in agreement with our previous observation.[20]

In order to more quantitatively understand the change in the shape of the bipolar *i*-*V* response, we have generated the *E* vs. log[$i/(i_{ss}$-i)] plots of the bipolar electrode and that of

the conventional setup. Often times a plot of E vs. $\log[i/(i_{ss}-i)]$ is prepared to show whether a process is reversible or not on a microelectrode.[26] If this plot is linear with a slope equal to $59.2/n$ mV the process is said to be reversible. For a non-linear plot with a slope greater than $59.2/n$ mV, the system is typically considered quasireversible or irreversible. The conventional direct connect configuration in Figure 4.2b shows a linear relationship with a slope of 59.2 mV as expected. On the other hand, for the bipolar setup, a linear relationship is obtained only when both poles have the same limiting current, in which case, the slope of the curve is 118 mV. When the cathodic pole has a greater limiting current than the anodic pole, a nonlinear relationship is obtained between E and the $\log[i/(i_{ss}-i)]$ as predicted from equations (4) and (5). The slope of the line at $E_{1/2}$ is a function of the ratio, $-i_{ss}^{c}/i_{ss}^{a}$, and is between 59 mV and 118 mV. We can anticipate that when this ratio goes to infinity, the slope of the line would approach 59 mV at half-wave potential.

This increased slope may be mistakenly understood to be an indication of irreversibility. Instead it is the result of directly coupling two reversible processes and is not itself indicative of any kinetic limitations. An alternative approach to determine the reversibility of an electrochemical process is to apply the Tomeš criterion of reversibility which states that for a reversible charge transfer the difference in quartile potentials, $\left|E_{3/4}-E_{1/4}\right|=56.4/n$ mV, where $E_{3/4}$ and $E_{1/4}$ refer to the three-quarter and one-quarter wave potentials respectively.[26] From Equation 5 we can derive the modified Tomeš criterion of reversibility for two coupled electrochemical reactions at a BPE to be:

$$\left|E_{3/4}-E_{1/4}\right|=\frac{RT}{F}\ln\left(27\left(\frac{i_{ss}^{c}+0.25i_{ss}^{a}}{i_{ss}^{c}+0.75i_{ss}^{a}}\right)\right) \tag{8}$$

This will allow for a more complete description of processes occurring at a microelectrode when used in a closed bipolar cell configuration as a tool for electrochemical analysis. By applying this criterion to the simulated results, values of 113 mV, 86 mV and 85 mV for 1:1, 10:1 and 100:1 are calculated respectively.

4.3 Experimental Section

4.3.1 Reagents and Chemicals.

Ferrocene (Fc, Fluka Analytical), dopamine hydrochloride (DA, Sigma-Aldrich), potassium ferricyanide ($K_3Fe(CN)_6$, Sigma-Aldrich), potassium ferrocyanide ($K_4Fe(CN)_6$, Fluka), potassium chloride (KCl, J. T. Baker), hexaammineruthenium (III) chloride ($Ru(NH_3)_6Cl_3$, Aldrich), tetra-n-butylammonium hexafluorophostphate ($TBAPF_6$, Aldrich), perchloric acid ($HClO_4$, Aldrich), and reagent grade acetonitrile (MeCN, Aldrich) were all used without further purification. All aqueous solutions were prepared using ≥18 MΩ-cm water from a Barnstead NanoPure purification system (Thermo Scientific). Oxygen reduction reactions were carried out in a 0.1 M KOH (Mallinkrodt) solution that had been bubbled with O_2 for a minimum of 20 minutes.

4.3.2 Electrode Fabrication.

Metal microelectrodes were fabricated by encapsulating wire in a glass capillary. Pt and Au micro wires with a diameter of 25 μm (99.95%, hard Alfa Aesar) were partially sealed in a borosilicate capillary (*o. d.* = 2.0 mm, *i. d.* = 1.0 mm, Sutter Instrument Co.) using a vacuum and hydrogen flame. Electrical contact was made by connecting the unsealed portion of the wire to a 150 μm tungsten wire with conductive silver paste (DuPont). The sealed portion of the wire was exposed with regular sandpaper and an alumina suspension on a wet polishing cloth. Carbon-fiber microelectrodes were fabricated according to our

previously published methods.[28] Briefly, a 5-μm-diameter carbon fiber was aspirated into a borosilicate glass capillary (*o. d.* = 1.2 mm, *i. d.* = 0.69 mm, Sutter Instrument Co.) and pulled with a micropipette puller (Model P-97, Sutter Instrument Co.). Afterwards the pulled tip was sealed with epoxy (Epoxy Technology) and beveled to 45º. For a direct connect carbon fiber electrode, electrical contact to the carbon fiber was achieved with conductive silver paste from inside the pulled glass capillary.

4.3.3 Cyclic Voltammetry.

All current-voltage responses were measured using a Chem-Clamp voltmeter/amperometer (Dagan) and a PAR 175 (Princeton Applied Research) universal function generator. The potentiostat was interfaced to a Dell computer through a PCI-6251 data acquisition board (National Instruments) via a BNC-2090 analog breakout box (National Instruments). The current-voltage data was recorded and analyzed using an in-house written virtual instrumentation with LabView 8.5 (National Instruments). For simplicity a direct-connect setup refers to a traditional one compartment two-electrode cell with one working electrode and a Ag/AgCl reference electrode (Bioanalytical Sciences Inc). A closed BPE cell was constructed by connecting two cells in series with two working microelectrodes connected.[20] Two Ag/AgCl electrodes were used to supply the driving voltage bias of the closed BPE cell.

4.4 Results and Discussion

4.4.1 Steady-State Voltammetry of a Microelectrode in a Closed Bipolar Cell.

Our theory has shown that when a microelectrode is used as the limiting pole in a closed bipolar setup, it would show a sigmoidal shape current-voltage response. Compared

to its voltammetric response in a conventional two-electrode setup, the bipolar response has the same limiting current. However, the $E_{1/2}$ and the shape of the voltammetric response are strongly dependent on the property of the excess pole. In general, the bipolar response is slower than the response in a conventional two-electrode cell as evident by the broadening of the wave. The distortion is however unrelated to electron-transfer kinetics and is simply due to electrochemical coupling in a bipolar cell.

Figure 4.3 displays the voltammetric responses of a 25-μm-diameter Au disk electrode in an aqueous solution of 1 mM ferrocyanide and 3 M KCl in three different setups. The black curve is the *i-V* response of the electrode in a two-electrode cell. A nice sigmoidal shape response is obtained for the oxidation of $Fe(CN)_6^{4-}$. The limiting current is 3.69 nA in good agreement with the prediction of 3.66 nA from equation 2. The blue, red, and green curves are *i-V* responses recorded from the same electrode in a closed bipolar cell. A second Au disk electrode of the same size is used as a cathodic pole. In this case, the cathodic pole is placed in an aqueous solution containing 1 mM ferricyanide and 0.1 M KNO_3 (blue curve). Since $Fe(CN)_6^{3-}$ has the same concentration and roughly the same diffusion coefficient as $Fe(CN)_6^{4-}$, the cathodic pole would yield a reduction limiting current equal to the oxidation limiting current on the anodic Au electrode (i.e., the electrode of interest), or, $-i_{ss}^{c}/i_{ss}^{a} = 1$. One can clearly see that the *i-V* response (blue) has roughly the same limiting current as that recorded in the two-electrode setup (black). However, the bipolar response is clearly slower than that of the two-electrode setup. This result is in good agreement with prediction from Figure 4.2a. The slower *i-V* response in the bipolar setup can be qualitatively understood by the additional energy/voltage requirement to drive the electrochemical process on the cathodic pole. The higher the redox concentration in the cathodic pole, the less voltage is

needed to drive the same amount of current on the cathodic pole. In a second experiment, the cathodic pole is placed in a 10 mM $Fe(CN)_6^{3-}$ solution (red curve). This would correspond to a situation in which the cathodic limiting current is roughly 10 times greater than the anodic pole, or $-i_{ss}^{c}/i_{ss}^{a} = 10$. Compared to the blue curve, the red *i-V* response indeed becomes much faster due to the increase in the cathodic limiting current. An even stronger effect is observed when the cathodic Au electrode is placed in a 100 mM $Fe(CN)_6^{3-}$ solution (green curve). Additionally, there is a clear negative shift in the $E_{1/2}$ as the concentration of $Fe(CN)_6^{3-}$ is increased, which is in good agreement with equation 6 and results in Figure 4.2. We have plotted the voltage across the bipolar electrode with respect to the logarithm of the limiting current ($\log[i/(i_{ss}-i)]$), as shown in Figure 4.3b. Also shown is the same plot for the electrode in the two-electrode setup (the black curve). The two-electrode setup yields a linear curve with a slope of 59.3 mV as expected indicating reversible response. Conversely, the blue curve is the plot for the same electrode in the bipolar setup with $-i_{ss}^{c}/i_{ss}^{a} = 1$. The blue curve is also found to be linear with a slope of 113.5 mV in agreement with prediction in Figure 4.2b. The red and green curves are the plots of the same electrode in the bipolar setup corresponding to when $-i_{ss}^{c}/i_{ss}^{a}$ is ~ 10 and ~100, respectively. These are nonlinear plots and the slopes at $E_{1/2}$ are 93.9 mV and 83.3 mV. The values obtained for $\left|E_{3/4} - E_{1/4}\right|$ are shown in Table 4.1 and are in agreement with the derived modified Tomeš criterion of reversibility. In summary, our experimental results have confirmed the theoretical prediction.

Both theory and experimental results have revealed that when a microelectrode is used in a bipolar setup, its voltammetric response may change significantly depending on the properties of two coupling poles. Most significantly, a microelectrode shows a slower *i-V*

response in a bipolar setup than its corresponding response in a conventional two or three-electrode cell. This sluggish voltammetric behavior is a result of electrochemical coupling and extra voltage requirement to drive complimentary current at the other pole. A greater limiting current on the coupling pole could lower this voltage requirement. Therefore, it could likely facilitate the observation of a faster voltammetric response.

4.4.2 Is "Reversible" Voltammetric Behavior Obtainable in a Bipolar Cell?

A bipolar mechanism can greatly simplify experimental setup in certain experiments involving ultramicroelectrodes and nanoelectrodes by eliminating direct wire contacts to the electrodes. For example, carbon-fiber microelectrodes use a salt solution to establish electrical contact which makes it convenient to quickly change electrodes during single-cell measurements. However, the electrochemical coupling between the two poles could complicate the analysis of the voltammetric behavior of a micro- or nanoelectrode by slowing down its *i*-*V* response. Although the limiting current is unlikely affected, the shape of the voltammetric response could depend strongly on the condition of the coupling pole. This could have significant impacts for electroanalytical applications where the shape of the voltammetric response is important. For example, the shape of the steady-state voltammogram of very small nanoelectrodes can be used to analyze heterogeneous electron-transfer kinetics.[29,30] Additionally, the sluggish voltammetric response of microelectrodes in a bipolar setup may cause increased uncertainty in certain electroanalytical sensing experiments, such as detection of electroactive neurotransmitters in single-cell measurements. It is reasonable to believe that a faster voltammetric response would be preferable in almost all electroanalytical experiments involving the use of microelectrodes and nanoelectrodes and a bipolar mechanism to establish electrical contact.

It is thus important to explore possible methods to obtain a nearly "reversible" voltammetric response in a closed bipolar setup. Because the slow voltammetric response is a result of additional voltage requirement from the coupling pole, we believe that a greater limiting current at the coupling pole could facilitate the observation of a nearly "reversible" voltammetric response. Since the limiting current on the coupling pole depends on the concentration of the redox species and electrode size and both factors are relatively easy to adjust, we set out experiments to obtain fast voltammetric responses by changing redox concentrations and greatly increasing the size of the excess pole.

Figure 4.4 shows a series of *i-V* responses of a 25-μm-diameter Pt disk microelectrode in a closed bipolar setup in acetonitrile containing 50 μM Fc and 0.1 M $TBAPF_6$. A second 25-μm-diameter Pt disk electrode is used as the excess cathodic pole and is placed in an aqueous solution containing 3 M KCl and $Fe(CN)_6^{3-}$ of various concentrations. This electrochemical cell configuration is similar to the one shown in Figure 4.1b except that the cathodic pole is a disk microelectrode. Here, the oxidation of Fc on the first Pt microelectrode is coupled to the $Fe(CN)_6^{3-}$ reduction on the cathodic pole, which also limits the overall *i-V* response of the BPE. All the *i-V* responses shown in Figure 4.4 have nearly the same limiting current due to Fc oxidation. The measured limiting current agrees well with prediction according to equation 2.

A general trend is observed in Figure 4.4: the Fc oxidation current increases much more quickly with voltage as the concentration of $Fe(CN)_6^{3-}$ increases. In the absence of $Fe(CN)_6^{3-}$, the oxidation of Fc is likely coupled to the reduction of soluble oxygen on the cathodic pole. A much slower *i-V* response is observed due to a smaller reduction current of oxygen. The oxidation of Fc becomes much faster in the presence of $Fe(CN)_6^{3-}$. The higher

the $Fe(CN)_6^{3-}$ concentration, the faster the current increases with voltage. Because the reduction current of $Fe(CN)_6^{3-}$ is roughly proportional to its concentration, the observed concentration effect on the *i-V* response is analogous to the effect of current ratio of two poles.

It is advantageous in a closed bipolar setup to use a high redox concentration on the coupling pole. However, the redox concentration is often limited in many conditions. For example, the concentration of saturated $Fe(CN)_6^{3-}$ is ~1.4 M at room temperature.[31] Since the limiting current on the coupling pole is also directly related to its size, it is in many conditions convenient to use a large coupling pole to obtain a fast voltammetric response on the limiting pole.

Figure 4.5 shows a series of i-V responses of a 25-μm-diameter Pt disk microelectrode in acetonitrile containing 0.5 mM Fc and 0.1 M $TBAPF_6$. The Pt disk electrode has been coupled to a 25-μm-diameter 2-mm-length Pt wire electrode used as an excess pole. The Pt microwire was placed in three different aqueous solutions of 5 mM $Fe(CN)_6^{3-}$, 5 mM $Ru(NH_3)_6^{3+}$, and oxygen saturated 0.1 M NaOH. The blue curve is the i-V response of the same 25-μm-diameter Pt disk electrode in 0.5 mM Fc in a two-electrode setup for comparison. One can see that all i-V responses in Figure 4.5 show very similar sigmoidal shape except for a noticeable shift in their $E_{1/2}$. The i-V response shows the minimum shift in position when the disk electrode is coupled to the reduction of oxygen on the Pt wire. The greatest $E_{1/2}$ shift is observed when the disk electrode is coupled to the reduction of $Fe(CN)_6^{3-}$. The shift in $E_{1/2}$ can be qualitatively explained by considering the formal potentials of the redox species on both poles and the effect of the limiting current ratio. The formal potential of Fc oxidation is ~0.55 vs NHE.[26] When the disk electrode is

coupled to oxygen reduction with a formal potential of ~-0.065 V vs NHE,[32] an $E_{1/2}$ around +0.61 V is anticipated. The purple i-V response shows an $E_{1/2}$ around 0.4 V, a negative shift of 0.21 V, which is caused by the large limiting current of oxygen reduction. Similar potential shifts have been observed in Figure 4.2 and Figure 4.3. Similarly, the reduction of $Fe(CN)_6^{3-}$ has a formal potential of 0.36 V vs NHE,[26] which would result in an $E_{1/2}$ of the bipolar response around 0.2 V. It is observed in Figure 4.5a that the $E_{1/2}$ is around 0 V, a negative shift of ~0.2 V again caused by the large ratio of the limiting current. The reduction of $Ru(NH_3)_6^{3+}$ has a formal potential of ~0.1 V vs NHE,[26] which gives a predicted $E_{1/2}$ around 0.45 V. However, the observed $E_{1/2}$ is around 0.2 V due to a negative shift of ~0.25 V.

Importantly, a quick examination of Figure 4.5a reveals that all *i-V* responses are very similar in overall shape. Figure 4.5b shows all four curves superimposed on each other. There is hardly any differences observable between the two-electrode response and those of the bipolar setups in $Fe(CN)_6^{3-}$ and $Ru(NH_3)_6^{3+}$. To quantitatively describe differences in wave shapes, the wave slope and $\left|E_{3/4} - E_{1/4}\right|$ are shown in Table 4.2. The calculated values show a slight increase in wave slope and $\left|E_{3/4} - E_{1/4}\right|$ for the bipolar configurations, as expected. The fact that all *i-V* responses have similar shapes and no major distortion is observed in the bipolar setups could be due to the significantly larger faradic current on the Pt wire electrode. A CV response of the Pt wire electrode in 5 mM $Fe(CN)_6^{3-}$ (not shown) shows a reduction current of ~2500 nA, which is roughly 275 times greater than the limiting current on the Pt disk. The results shown in Figure 4.5 are encouraging because it indicates that one can obtain a nearly reversible *i-V* response even in a bipolar setup when a microelectrode is coupled to a large excess pole. This is an important result because it

implies that when a bipolar setup is used in electroanalytical applications, one should use a large coupler electrode in order to more accurately examine the voltammetric properties of a microelectrode or to detect quick changes in analyte concentrations.

Due to the wide usage of carbon-based microelectrodes in bioanalytical sensing, it is important to verify the above conclusions with CFEs. As shown in the Figure 4.6, similar observations have been obtained with carbon-fiber microelectrodes. Figure 4.6a is a series of *i-V* responses collected from a closed bipolar cell consisting of a 5-μm-diameter disk CFE in a 50 μM Fc solution containing 0.1 M $TBAPF_6$ and a CFE with an exposed 5-μm-diameter, 2-mm-length carbon fiber in varying reduction reactions. The *i-V* response of the same disk CFE in a two-electrode cell is given as the blue curve, in which a direct electrical contact was made to the fiber from inside the glass capillary using silver epoxy. Figure 4.6b is the overlaid *i-V* responses after correcting their $E_{1/2}$ shifts. One can see that all the *i-V* responses in the bipolar setup have similar shapes and limiting currents, which are nearly indistinguishable from the response in the two-electrode setup.

In addition to using Fc oxidation as a model reaction, we have studied the oxidation of dopamine on a 5-μm-diameter CFE. Figure 4.6c shows a series of *i-V* responses collected on a 5-μm-diameter CFE in 100 μM dopamine when coupled to the reduction of several different redox species including $Fe(CN)_6^{3-}$, $Ru(NH_3)_6^{3+}$, saturated oxygen in 0.1 M NaOH, and soluble oxygen in 3 M KCl. The resulting *i-V* responses all show very similar shapes and are almost indistinguishable from the one collected in a two-electrode setup on the same electrode, as shown in Figure 4.6c and d. The wave slope and $\left|E_{3/4} - E_{1/4}\right|$ for the curves in Figure 4.6a and c are shown in Table 4.3 and demonstrate little variance between bipolar configurations. The results shown in Figure 4.6 have further confirmed that when a

microelectrode is used in a bipolar setup, a large coupler electrode is needed to obtain nearly reversible voltammetric responses.

4.5 Conclusion

We have discussed the theory and corresponding experiments to more fully understand the steady-state voltammetric response of a microelectrode used in a closed bipolar setup. Our theory shows the voltammetric response is likely distorted when a microelectrode is used in a bipolar setup and is often slower than that in a conventional two-electrode setup. The slower response in the bipolar setup is likely due to additional voltage/energy requirement to drive the faradaic reaction at the coupling pole. The shape of the bipolar voltammetric response depends on the ratio of limiting currents on both poles. A large faradic current on the excess coupling pole facilitates the observation of a fast voltammetric response. This can be realized by increasing the redox concentration and the electrode size on the excess coupling pole.

4.6 Tables and Figures

Table 4.1 A comparison of the wave parameters obtained from the predicted *i-V* curves in Figure 4.2 and that measured from experimental *i-V* curves in Figure 4.3 for different $-i_{ss}^{c}/i_{ss}^{a}$ ratios. The corresponding wave parameters for the two-electrode cell are also listed for comparison.

$-i_{ss}^{c}/i_{ss}^{a}$	Wave slope (mV)	Wave slope$_{calc}$ (mV)	$\lvert E_{3/4}-E_{1/4}\rvert$ (mV)	$\lvert E_{3/4}-E_{1/4}\rvert_{calc}$ (mV)
Two-electrode	59.3	59.2	56	56.4
1:1	113.5	118	111	113
10:1	93.9	86	87	86
100:1	83.3	85	79	85

Table 4.2 Wave parameters obtained from the *i-V* curves in Figure 4.5 for Fc oxidation at a Pt BPE. The corresponding wave parameters for the two-electrode cell are also listed for comparison.

Coupling redox	Wave Slope (mV)	$\lvert E_{3/4}-E_{1/4}\rvert$ (mV)
Two-electrode	68.1	65
$K_3Fe(CN)_6$	89.1	85
$Ru(NH_3)_6Cl_3$	84.9	81
Oxygen	75.5	72

Table 4.3 The wave parameters obtained from the *i-V* curves in Figure 4.6 for the oxidation of Fc and dopamine at a carbon fiber microelectrode coupled to a carbon fiber wire electrode in different redox solutions. The corresponding wave parameters for the two-electrode cells are also listed for comparison.

Redox species (limiting pole)	Redox species (coupling pole)	Wave Slope (mV)	$\lvert E_{3/4}-E_{1/4}\rvert$ (mV)
Ferrocene	Two-electrode	60.8	59
	$K_3Fe(CN)_6$	69.2	66
	$Ru(NH_3)_6Cl_3$	68.1	65
	Oxygen	70.8	67
	KCl	68.1	65
Dopamine	Two-electrode	78.6	74
	$K_3Fe(CN)_6$	83.8	80
	$Ru(NH_3)_6Cl_3$	78.6	75
	Oxygen	89.1	85
	KCl	83.8	80

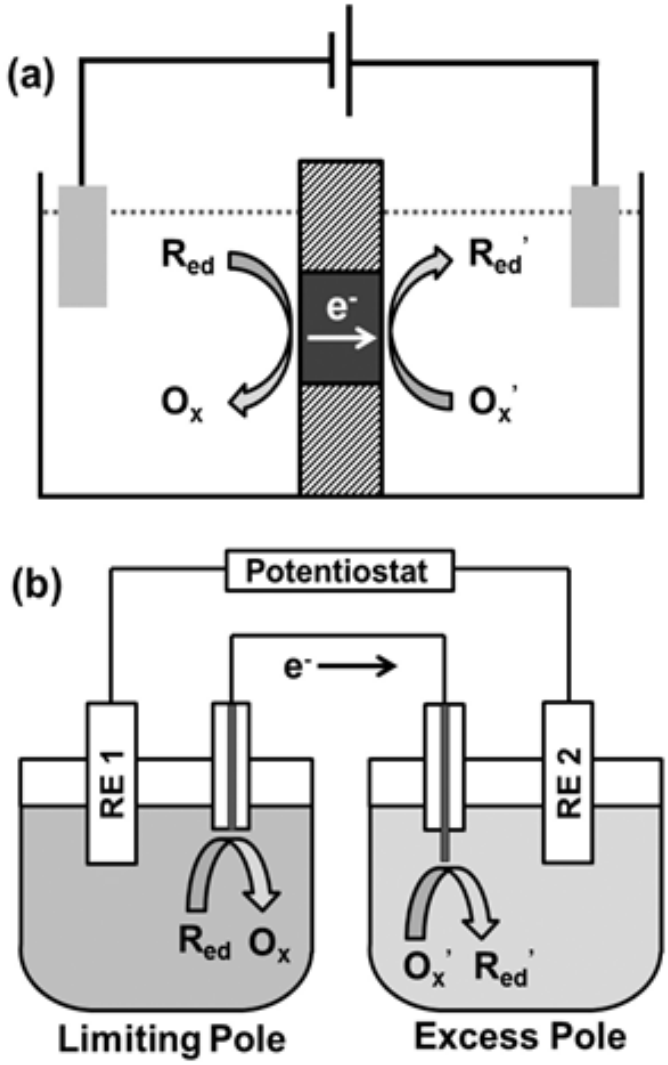

Figure 4.1 Schematic of bipolar electrochemistry.
(a) A schematic of a closed bipolar electrode cell. (b) A schematic of a serious-coupled bipolar cell containing a disk microelectrode in one compartment and a cylindrical microelectrode in the other compartment. The working electrode lead from the potentiostat is connected to reference electrode 2 (RE2) and the reference lead to reference electrode 1 (RE1). The anodic pole is limiting and the cathodic pole is in excess.

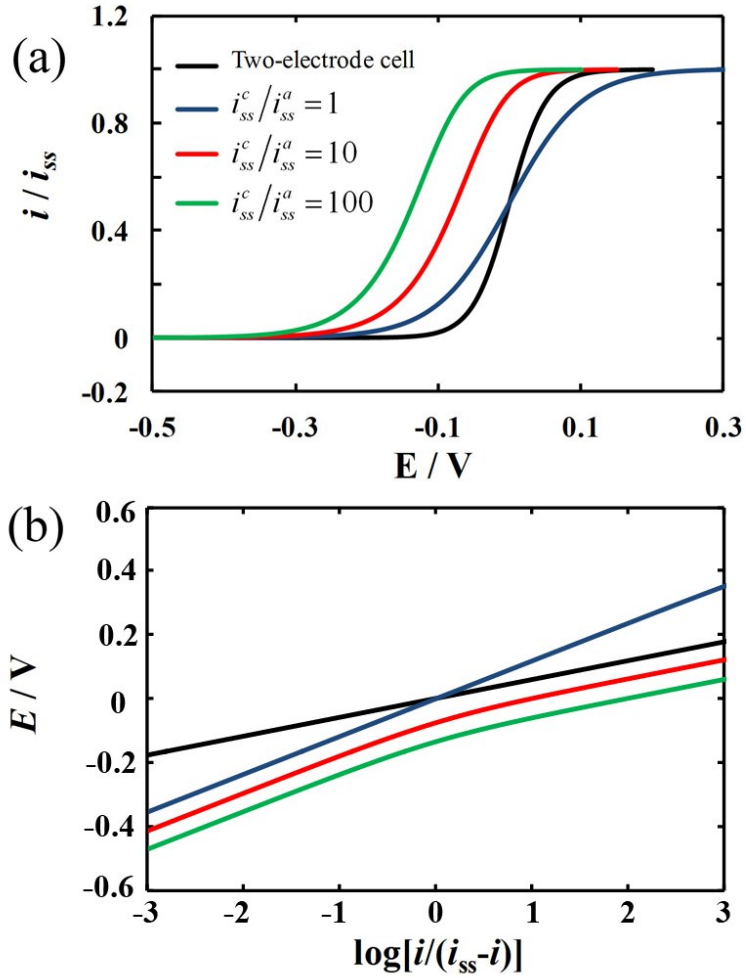

Figure 4.2 Theoretical voltammetric response of bipolar microelectrode
(a) Theoretical *i-V* responses of a microelectrode in a two-electrode cell (black) and in a closed bipolar electrode setup when coupled to a cathodic pole. The blue, red, and green curves correspond to when the ratios of the limiting currents are 1, 10 and 100, respectively. The formal potentials of the oxidation reaction on the microelectrode and the cathodic reaction on the coupling electrode have been assumed to be 0 V. The voltage for the bipolar setup is the voltage applied across the bipolar electrode and the voltage for the two-electrode setup is the voltage applied on the microelectrode with respect to the reference electrode. (b) A plot of the voltage applied across the bipolar electrode (for the blue, red, and green curves) as a function of the $\log[i/(i_{ss}-i)]$ for the *i-E* curves given in (a).

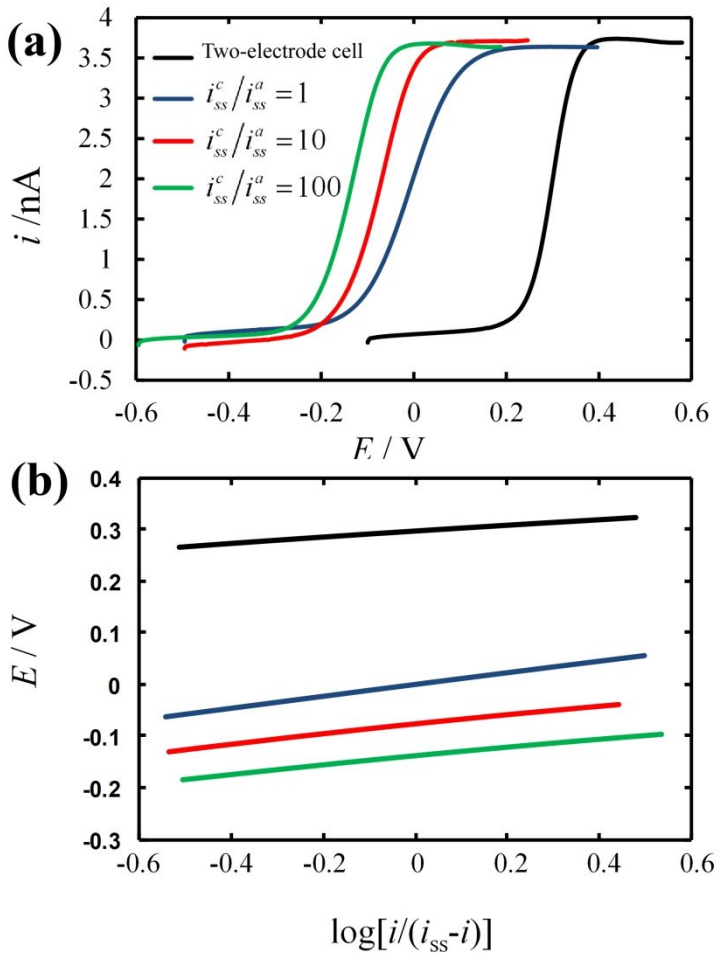

Figure 4.3 Experimental voltammetric response of bipolar microelectrode.
a) The *i-V* responses of a 25-µm-diameter Au disk microelectrode in a solution of 1 mM $Fe(CN)_6^{4-}$ and 3 M KCl in a two-electrode set-up (black curve) and closed bipolar cell when coupled to a second 25-µm-diameter Au disk electrode as a cathodic pole. The cathodic pole was placed in a 3 M KCl solution containing $Fe(CN)_6^{3-}$ of various concentrations: 1 mM (blue curve), 10 mM (red curve), and 100 mM (green curve). The scan rate was 20 mV/s for all scans. The voltage for the bipolar setup is the voltage applied across the bipolar electrode as illustrated in Figure 4.1b and the voltage for the two-electrode setup is the voltage applied on the microelectrode with respect to a Ag/AgCl reference electrode. (b) A plot of the voltage applied across the bipolar electrode (for the blue, red, and green curves) as a function of the log[$i/(i_{ss}-i)$] for the *i-E* curves given in (a). Only voltages between $E_{1/4}$ and $E_{3/4}$ are plotted in (b).

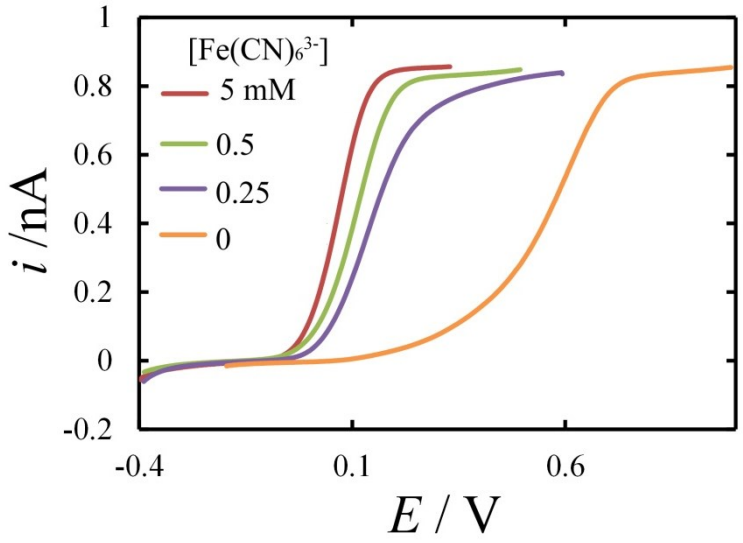

Figure 4.4 Concentration dependence at coupling pole.
The *i-V* responses of a 25-µm-diameter Pt disk electrode in acetonitrile containing 50 µM Fc and 0.1 M $TBAPF_6$. The oxidation of Fc was coupled to the reduction of ferricyanide of varying concentrations in a 3 M KCl solution on another 25-µm-diameter Pt microelectrode.

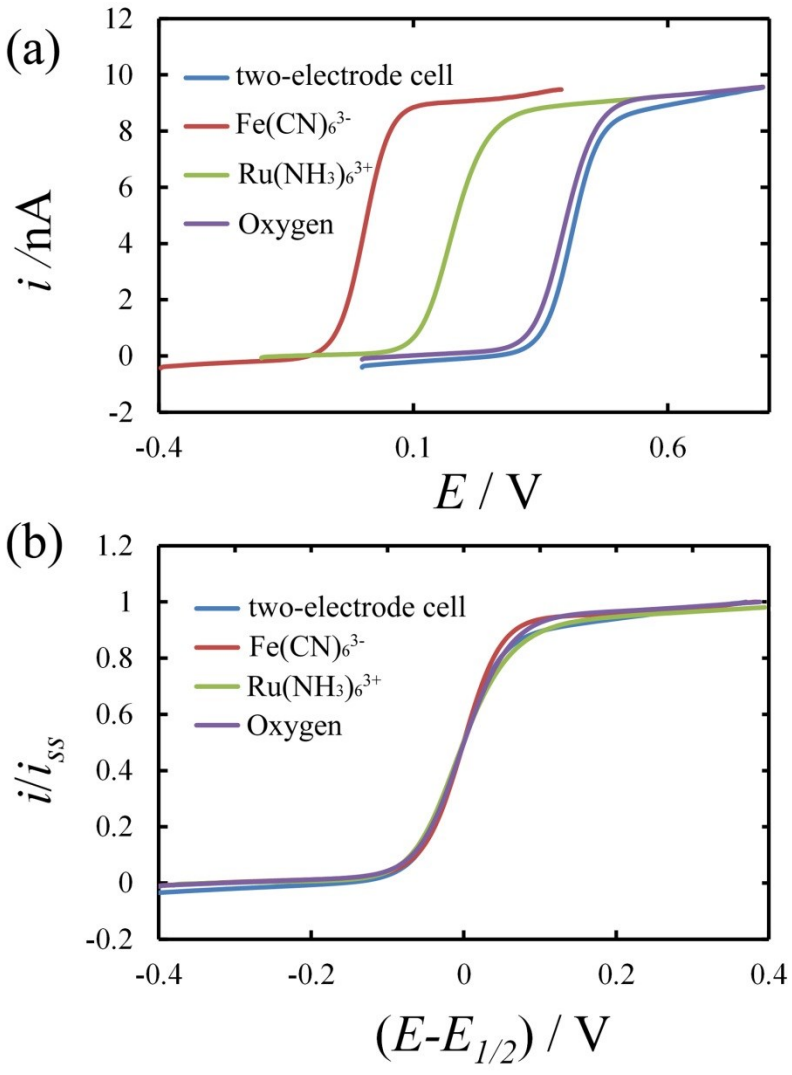

Figure 4.5 Voltammetric response of Pt bipolar microelectrode.
(a) The *i-V* responses of a 25-µm-diameter Pt disk electrode in acetonitrile containing 0.5 mM Fc and 0.1 M $TBAPF_6$. The oxidation of Fc was coupled to the reduction of three different redox species, 5 mM $Fe(CN)_6^{3-}$, 5 mM $Ru(NH_3)_6^{3+}$, and saturated oxygen in 0.1M NaOH on a 25-µm-diameter, 2-mm-length Pt wire. The i-V response of the same electrode in a two-electrode cell is given as the blue curve for comparison. (b) An overlay plot of the normalized CVs in (a) highlighting the change in wave shape.

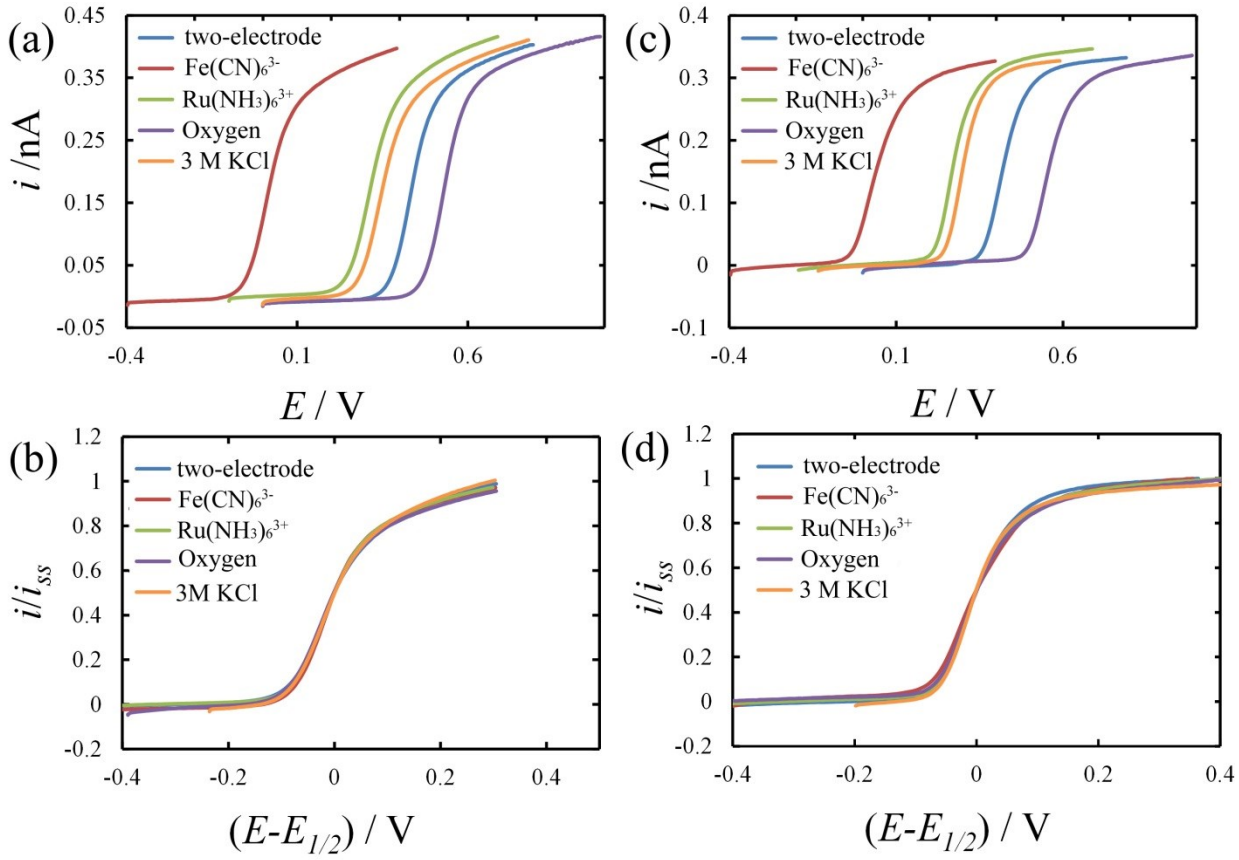

Figure 4.6 Voltammetric response of carbon fiber bipolar microelectrode.
The *i-V* responses of a 5-µm-diameter carbon-fiber disk electrode in a solution of (a) 50 µM Fc 0.1M $TBAPF_6$ and (c) 100 µM dopamine coupled to a 5-µm-diameter, 2-mm-length carbon fiber in a solution containing different redox molecules including 5 mM $Fe(CN)_6^{3-}$, 5 mM $Ru(NH_3)_6^{3+}$, saturated oxygen in 0.1M NaOH, and 3 M KCl. The CV response of the same disk electrode in a two-electrode cell is given for comparison. An overlay plot of the normalized CVs is given in (b) for Fc and (d) for dopamine to highlight the change in wave shape.

4.7 References

(1) Mavre, F.; Anand, R. K.; Laws, D. R.; Chow, K. F.; Chang, B. Y.; Crooks, J. A.; Crooks, R. M. *Anal. Chem.* **2010**, *82*, 8766–8774.

(2) Klett, O.; and Nyholm, L. *Anal. Chem.* **2003**, *75*, 1245–1250.

(3) Ordeig, O.; Godino, N.; del Campo, J.; Munoz, F. X.; Nikolajeff, F.; and Nyholm, L. *Anal. Chem.* **2008**, *80*, 3622–3632.

(4) Zhan, W.; Alvarez, J.; and Crooks, R. M. *J. Am. Chem. Soc.* **2002**, *124*, 13265–13270.

(5) Arora, A.; Eijkel, J. C. T.; Morf, W. E.; and Manz, A. *Anal. Chem.* **2001**, *73*, 3282–3288.

(6) Chow, K. F.; Mavré, F.; and Crooks, R. M. *J. Am. Chem. Soc.* **2008**, *130*, 7544–7545.

(7) Chow, K. F.; Chang, B.-Y.; Zaccheo, B.; Mavré, F.; and Crooks, R. M. *J. Am. Chem. Soc.* **2010**, *132*, 9228–9229.

(8) Laws, D. R.; Hlushkou, D.; Perdue, R. K.; Tallarek, U.; and Crooks, R. M. *Anal. Chem.* **2009**, *81*, 8923–8929.

(9) Dhopeshwarkar, R.; Hlushkou, D.; Nguyen, M.; Tallarek, U.; and Crooks, R. M. *J. Am. Chem. Soc.* **2008**, *130*, 10480–10481.

(10) Hlushkou, D., Perdue, R. K., Dhopeshwarkar, R., Crooks, R. M., and Tallarek, U. *Lab on a Chip* **2009**, *9*, 1903–1913.

(11) Perdue, R. K.; Laws, D. R.; Hlushkou, D.; Tallarek, U.; and Crooks, R. M. *Anal. Chem.* **2009**, *81*, 10149–10155.

(12) Adams, K. L.; Puchades, M.; Ewing, A. G. *Annu. Rev. Anal. Chem.* **2008**, *1*, 329–355.

(13) Hiddleston, J. N.; Douglas, A. F. *Nature* **1968**, *218*, 601–602.

(14) Kazdobin, K.; Shvab, N.; Tsapakh, S. *Chem. Eng. J.* **2000**, *79*, 203–209.

(15) Ulrich, C., Andersson, O., Nyholm, L., and Björefors, F. *Anal. Chem.* **2009**, *81*, 453–459.

(16) Wang, Y.; Hernandez, R. M.; Bartlett, D. J.; Bingham, J. M.; Kline, T. R.; Sen, A.; and Mallouk, T. E. *Langmuir* **2006**, *22*, 10451–10456.

(17) Warakulwit, C.; Nguyen, T.; Majimel, J.; Delville, M. H.; Lapeyre, V.; Garrigue, P.; Ravaine, V.; Limtrakul, J.; and Kuhn, A. *Nano Lett.* **2008**, *8*, 500–504.

(18) Shiguro, Y.; Inagi, S.; Fuchigami, T. *Langmuir* **2011**, *27*, 7158–7162.

(19) Fosdick, S. E.; Crooks, R. M. *J. Am. Chem. Soc.* **2012**, *134*, 863–866.

(20) Guerrette, J. P.; Oja, S. M.; Zhang, B. *Anal. Chem.* **2012**, *84*, 1609–1616.

(21) Plana, D.; Jones, F. G. E.; Dryfe, R. A. W. *J. Electroanal. Chem.* **2010**, *646*, 107–113.

(22) Hotta, H.; Akagi, N.; Sugihara, T.; Ichikawa, S.; Osakai, T. *Electrochem. Commun.* **2002**, *4*, 472–477.
(23) Huffman, M. L.; Venton, B. J. *Analyst* **2009**, *134*, 18–24.
(24) Heien, M.; Johnson, M.; Wightman, R. *Anal. Chem.* **2004**, *76*, 5697–5704.
(25) Bruns, D. *Methods* **2004**, *33*, 312– 321.
(26) Bard, A. J. and Faulkner, L. R. *Electrochemical Methods*, 2nd ed.; Wiley: New York, **2001**.
(27) Saito, Y. *Rev. Polarogr.* **1968**, *15*, 177–182.
(28) Adams, K. L.; Jena, B. K.; Percival, S. J.; Zhang, B. *Anal. Chem.* **2011**, *83*, 920–927.
(29) Watkins, J. J.; Chen, J.; White, H. S.; Abruna, H. D.; Maisonhaute, E.; Amatore, C. *Anal. Chem.* **2003**, *75*, 3962-3971.
(30) Li, Y.; Bergman, D.; Zhang, B. *Anal. Chem.* **2009**, *81*, 5496– 5502.
(31) Friend, J. A. N.; Smirles, W. N. *J. Chem. Soc*. **1928**, 2242–2245.
(32) Song, C. J.; Zhang, J. *PEM Fuel Cell Electrocatalysts and Catalyst Layers Fundamentals and Applications* (Ed.) Zhang, J., 2008, Vol. XXII.

CHAPTER 5
Voltammetric Behavior of Gold Nanotrench Electrodes*

5.1 Introduction

New nanoscale porous electrodes have been increasingly used in studying molecular transport in compact spaces.[1-3] Glass nanopore electrodes have received tremendous research interest in this field due to their easy construction, well-defined and robust structure, and rich surface chemistry at the pore walls.[1,4] Two important facts have placed glass nanopore electrodes in a unique position for this application: 1) the surface of the nanopore walls can be readily modified via silane chemistry to introduce desired chemical and/or physical interactions between the pore walls and the redox molecules[5] and 2) a wide range of sizes of the glass nanopore orifice can be readily obtained.[6] The steady-state limiting current of the nanopore electrode provides direct information for the flux of redox molecule through the nanopore orifice.

A major challenge of using a glass nanopore electrode for analytical applications, however, is the small current magnitude of the voltammetric signal. The steady-state voltammetric response of a nanopore electrode is strongly dependent on the pore depth, the size of the pore orifice, and the angle of the cone for a conical shape nanopore.[6] The diffusion-limited current decreases quickly as the depth of the pore increases. This has placed an important challenge in using such nanopore sensors in everyday experiments due to the required use of specialized equipment capable of measuring current in the picoamp (pA)

---

* This chapter is adapted with permission from Guerrette, J. P., Percival, S. P. & Zhang, B. Voltammetric Behavior of Gold Nanotrench Electrodes. *Langmuir*. **2011**, 27, 12218-12225. Copyright (2011) American Chemical Society.

range. An additional challenge may arise with the possibility of irreproducible surface modification due to the extremely small area of the walls at the nanopore orifice.

Our group has been interested in using nanotrench electrodes to probe transport of redox molecules in nanoscale spaces and to develop new nanoelectrode sensors. A nanotrench electrode can be easily prepared from a Au nanoband electrode by simple electrochemical etching, as depicted in Figure 5.1. A distinct advantage of a nanotrench electrode is that it offers an electrochemical signal (e.g., steady-state limiting current) which can be three orders of magnitude higher than a nanopore electrode with similar critical dimensions and depth. Therefore, a nanotrench electrode with a width (w) in the 1-100 nm range may readily overcome the aforementioned challenge of a nanopore electrode by having a band-length (l) in the millimeter scale. The small width of the nanotrench could help to achieve confined molecular transport. The large band length, on the other hand, offers a desired level of electrochemical current.[7,8] In addition, the surface modification on the insulating walls could also be more controllable for the nanotrench electrode compared to a small nanopore due to increased mass transport.

Nanoband electrodes of various materials[9,10] and geometries[11] have been used in fundamental electrochemistry[12] and electrochemical sensing.[13] It has been shown that a nanoband electrode experiences higher current densities than macroscale band electrodes due predominately to radial-type diffusion.[14] The narrow width of a nanoband electrode also results in a more uniform current density across the band avoiding the issue of large changes nearing the electrode edges seen in macroelectrodes. Further improvements in the uniformity of the current density along the electrode surface have been seen by placing the electrode at the bottom of a recess.[15,16]

Despite their importance, very few methods have been reported on the fabrication of well-defined nanotrench electrodes.[17-20] Penner and co-workers described an interesting method, which involves the etching of a nickel nanoband electrode deposited between a glass surface and a layer of photoresist.[18, 19] The resulting trench has been used as a sacrificial template for the patterned electrodeposition of metal nanowires. A second method, presented by Arrigan and co-workers,[17] uses focused ion beam (FIB) milling to expose a Pt nanoband at the bottom of a silicon nitride passivation layer. Electrodes fabricated using these methods clearly have their useful applications. However, some challenges still exist. The first method produces a band electrode at the bottom of an asymmetrically designed trench with one wall of the trench extending beyond the plane of the top of the trench and that of the inlaid band electrode. This geometry, with one of the walls of the recess extending beyond the other, would not allow for complete radial diffusion to the trench opening and in turn decrease the flux of redox species to the electrode. The FIB milling method, on the other hand, is believed to produces trenches with angled walls and may cause re-deposition of silicon nitride at the base of the trench partially blocking the electrode surface. The band width is limited by the width of the ion beam and the depth is predefined by the thickness of the passivation layer. Additionally, metal ions used in the FIB milling process may be left behind in the substrate and electrode matrices thus causing potential problems for certain analytical applications.

Here we focus our efforts on the preparation and electrochemical characterization of a Au nanotrench electrode, with a single Au nanoband electrode located at the bottom of a glass/epoxy nanotrench. The inlaid nanobands are produced using a method similar to that described by Wightman and co-workers.[7] A facile electrochemical etching process is used to partially remove the inlaid nanoband electrodes in a NaCl solution. By having the electrode

at the bottom of a narrow trench, significant analyte-substrate interaction occurs as the redox species diffuses into the nanotrench. We demonstrate the ability to fabricate nanotrench electrodes with variable recess depths from a few nanometers up to a few microns while maintaining a steady-state voltammetric response. We have obtained an analytical expression for the quasi-steady-state diffusion-limited current of the nanotrench electrode which allows for an estimation of the recess depth. The validity of this expression is shown by an excellent agreement with results obtained through numerical simulations. Our experimental results indicate that although the fabrication and polishing processes of nanoband electrodes often produces delaminations and somewhat rough band geometry, the electrochemical etching process serves to smooth the electrode surface and reduce the adverse effects of delaminations as seen in the voltammetric response particularly at fast scan-rates.

Potential applications of such nanotrench electrodes could include nanoscale electrochemical sensors through modification of the side walls to take advantage of the molecular scale passage way. Additionally, studies of mass-transport within the confines of the recess and the effects on electric double layer structure can also benefit from electrodes of this design.

5.2 Experimental Section

5.2.1 Chemicals.

Ferrocene (Fc, Fluka Analytical), tetra-*n*-butylammonium hexafluorophosphate ($TBAPF_6$, Aldrich), NaCl (J.T. Baker) and reagent grade MeCN (Aldrich) were all used without further purification. A Barnstead Nanopure water purification system was used to provide >18 MΩ·cm deionized water as needed.

5.2.2 Fabrication of gold nanotrench electrode.

Glass microscope slides (Thermo Scientific) were cut into rectangular pieces approximately 1.25 cm x 0.6 cm. The glass was then cleaned in water followed by rinsing with acetone. Once dried the glass surface was masked with standard transparent adhesive tape and patterned by cutting away desired section of the tape. Gold (99.999% pure, Kurt J. Lesker Co.) was then deposited on the glass surface using an in-house thermal evaporator. The thickness of the deposited Au film was monitored by a quartz crystal microbalance equipped with an Inficon XTC deposition controller, which was further verified by atomic force microscopy (AFM) as shown in Figure 5.2. Upon cooling, the gold surface at the working ends of the pre-electrode was coated with Epo-Tek 301 epoxy (Epoxy Technology, Inc.) to prevent contamination from dust and minimize air bubbles and delamination in further fabrication steps. Electrical contact was made to the other end of the gold film with a tungsten wire using Ag conductive paste (DuPont). To increase mechanical stability and ensure all surfaces were initially insulated, the electrodes were placed in latex pipet bulbs (VWR International), used as molds, which were then filled with additional epoxy and allowed to cure at 100°C for 1.5-2h. In order to expose the gold nanoband, the electrodes were sanded, first with a coarse 320 grit sandpaper and then working down to a 1200 grit polishing disk before using 1.0 μm and 0.05 μm alumina powder on a wet polishing cloth pad (Buehler). Electrodes were then rinsed with water followed by methanol and allowed to air dry. After initial characterization by cyclic voltammetry the inlaid gold nanobands were electrochemically etched in a 3M NaCl solution. This was accomplished by applying a sinusoidal potential waveform (80Hz, $4V_{pp}$) using an Agilent 33220A Function Generator. The length of etching time was varied in order to achieve the desired depth of recess.

5.2.3 Cyclic Voltammetry.

A one-compartment, three-electrode cell equipped with a Ag/AgCl reference electrode (Bioanalytical Sciences Inc.) and a Pt coil counter-electrode or a two-electrode cell with a Ag/AgCl reference electrode was used in all electrochemical experiments. Cyclic voltammetry was performed using either a Princeton Applied Research Model 173 Potentiostat/Galvanostat or a Dagan Chem-Clamp voltammeter/amperometer connected to an EG&G PAR Model 175 Universal Programmer. Voltammetric response was recorded using a PCI-6251(National Instruments) data acquisition card on a Dell computer using in-house LabView 8.5 software (National Instruments). For experiments with potential sweep rates faster than 1 V/s, an ultrafast data acquisition card (PCI-5122, National Instruments) was used instead. A scan-rate of 50 mV/s was used for all potential sweep experiments except those specifically noted otherwise.

5.2.4 Finite-Element Simulations.

Steady-state diffusional flux of redox molecule to the electrode surface and the transient voltammetric response were modeled using COMSOL Multiphysics 3.4 software operated on a Dell Precision T7400 workstation (Intel Xeon E5430, 2.66 GHz, 8 GB RAM). Details of the model design and boundary conditions are presented in the results and discussion section.

5.2.5 Scanning Electron Microscopy.

Scanning Electron Microscopy (SEM) images were obtained using a field-emission microscope (FEI Sirion). Some samples were sputter coated with a thin layer (2-3nm) of Au/Pd for SEM imaging as noted.

5.2.6 Atomic Force Microscopy.

Atomic Force Microscopy was performed using a Veeco Dimension 3100 Scanning Probe Microscope operating in tapping mode using OTESPA cantilever tips. The microscope was placed within a noise and vibration isolation table and all AFM images have been flattened to remove the background curvature of the substrate surface, but are otherwise free of modification.

5.3 Results and Discussion

5.3.1 Fabrication of the Au Nanotrench Electrode.

Figure 5.1 shows the general method for the fabrication of the nanotrench electrode through the electrochemical etching of a Au nanoband electrode in a 3M NaCl solution. Several materials have been previously used in the literature as the substrate for creating metal nanoband electrodes including mica,[21,22] glass,[7, 8, 18] silicon dioxide[23] or silicon nitride[17] on silicon wafers, Mylar[7] and Kapton.[19] Glass microscope slides were chosen as the primary substrate in our experiments due to their low cost and mechanical stability, which is important for the polishing step. Glass does however suffer from weak adhesion to thin Au films and therefore is prone to delamination. A thin chromium film, often used to improve adhesion, was not employed here in order to avoid possible interference in the narrow inlaid band and nanotrench electrodes. An adhesion layer would possibly lead to unpredictable geometry of the resulting nanotrench due to the likelihood of different etching rates of Au and Cr. In order to reduce the occurrence of delamination, the glass slides were patterned with Scotch tape, which was removed after deposition of Au, leaving exposed glass on both sides of the metal band. This served to increase the glass/epoxy contact area as well as more

easily regulate band length. A diagram showing the entire patterned electrode is given in Figure 5.3.

A challenging step in the fabrication is the mechanical polishing process to expose the inlaid band electrode. Often times it is difficult to obtain a clean voltammogram without noticeable signs of leakage, delamination or partial blockage. It has been shown that the fabrication of gold microelectrodes, particularly the polishing step, leads to surface heterogeneities that are noticeable in the electrode's voltammetric response.[24] This behavior is seen with microelectrodes however it is likely that the effect is much more apparent in nanoelectrodes. An apparent decrease in limiting current is occasionally observed if excessive polishing is performed using alumina powder. We believe that this is caused by a mechanical etching and blocking of the Au electrode surface, where the rolling alumina particles dig out the gold and become imbedded in the resulting trench. Only slight polishing was performed using alumina powder in an attempt to smooth excess/overhanging Au but reduce damage to the band.

5.3.2 An Analytical Expression of the Diffusion-Limited Current at a Nanotrench Electrode.

In order to better understand the mass-transport of redox species to the electrode surface, we chose to construct a model of the nanotrench electrode. Assuming that the diffusion from the bulk solution to the mouth of the trench would follow the model previously described for an inlaid nanoband electrode, an expression could be easily derived by considering the added mass-transport resistance in the nanotrench. We followed a method similar to what has been previously described for treating the nanopore electrode.[6] The

diffusion-limited current at an inlaid nanoband electrode has been shown to be approximated by the corresponding expression for a hemi-cylinder,[25]

$$i_{lim}^{d=0} = \frac{2\pi nFDC^{*}l}{\ln\left(\frac{64Dt}{w^2}\right)} \quad (1)$$

where D is the diffusion coefficient of the redox molecule (cm^2/s), C^* is the bulk concentration (mol/cm^3), n is the number of electrons transferred per molecule, F is Faraday's constant (96485.3 C/mol), l is length of band (cm), w is the band width (cm) and t is time and is equal to RT/Fv,[17] where R is the gas constant (8.314 J/mol·K), T is temperature (K), and v is scan-rate (V/s). The general definition for mass-transfer limited current, $i_{lim} = nFC^{*}/R_{MT}$, where R_{MT} is the mass-transfer resistance, allows for the derivation of the external mass-transfer resistance, R_{EX}, from equation 1,

$$R_{EX} = \frac{\ln\left(\frac{64Dt}{w^2}\right)}{2\pi Dl} \quad (2)$$

The total mass-transfer resistance for a nanotrench electrode can be obtained by combining R_{EX} with the internal mass-transfer resistance within the trench, R_{IN}. Assuming a linear concentration profile for the nanotrench, R_{IN} can be simply derived as $R_{IN} = d/DA$, where d is the depth and A is the cross sectional area of the trench. This yields a combined mass-transfer resistance, R_{MT},

$$R_{MT} = R_{EX} + R_{IN} = \frac{1}{Dl}\left(\frac{\ln\left(\frac{64Dt}{w^2}\right)}{2\pi} + \frac{d}{w}\right) \quad (3)$$

Therefore an approximate expression for the diffusion-limited current for the nanotrench electrode as a function of recess depth is given by

$$i_{lim} = \frac{nFDC^{*}l}{\left(\frac{1}{2\pi}\ln\left(\frac{64Dt}{w^2}\right)+\frac{d}{w}\right)} \quad (4)$$

Taking the ratio of the expressions in equations 1 and 4 to obtain the normalized current and then solving for *d* yields a convenient equation for the calculation of trench depth,

$$d = \frac{w}{2\pi}\ln\left(\frac{64Dt}{w^2}\right)\left[\left(i_{lim}^{d=0}\Big/ i_{lim}\right)-1\right] \quad (5)$$

All experimental depths reported hereafter are the results of calculations using equation 5.

5.3.3 Numerical Simulations of the Quasi-Steady-State and Transient Voltammetric Response.

Figure 5.4 shows the 2-dimensional geometry of the model used in the numerical simulation. The third dimension, length, is treated as a scalar for values of $l >> w$ and therefore was eliminated from the model to reduce computing time. The boundary conditions used were, bulk concentration of redox molecule, C^{*}, at boundaries 1, 3 and 8; flux equal to zero through all of the insulating surfaces, 2, 4, 6 and 7; and concentration of redox-active molecule equal to zero at the electrode, 5. Migration is ignored in the model due

to the presence of a large excess of supporting electrolyte and the fact that Fc is neutral. Convection is also not considered in these calculations.

Figure 5.5 shows a plot of the normalized limiting current, $i_{lim}/i_{lim}^{d=0}$, as a function of normalized depth for five different band widths in order to compare the simulated data (points) with calculations from equation 4 (lines). The data obtained from the finite-element simulations is in excellent agreement (< 1% difference at all values of *d*) with the values calculated using equation 4 where C^* = 5 mM, D = 2.47 x 10^{-5} cm^2/s, n = 1 and v = 0.05 V/s.

In order to simulate the voltammetric response of the inlaid nanoband and nanotrech electrodes, a 1-e reversible oxidation reaction, $R \longrightarrow O + e^-$, is assumed. We followed the previously described method[1] with slight modification to the potential waveform. Briefly, the triangular potential waveform was modeled using the following infinite-Fourier series:

$$E(t) = \frac{8(E_{range})}{\pi^2} \sum_{k=0}^{\infty} (-1)^k \frac{\sin((2k+1)\omega t)}{(2k+1)^2} \tag{6}$$

where E_{range} is the range of the potential swept, ω is the angular frequency of the wave and is equal to $\pi v/(2E_{range})$. A sufficiently accurate waveform was generated by using values of *k* from 0 to 7 in the above series. Figure 5.6 shows a voltage waveform calculated using equation 6 and *k* values from 0 to 7. By assuming equal diffusion coefficients of *R* and *O*, the mass balance equation, $C^* = C_{R,s} + C_{O,s}$ applies where $C_{R,s}$ and $C_{O,s}$ are the concentrations of *R* and *O* at the electrode surface, respectively. The Nernst equation, $E = E° + (RT/nF) \ln(C_{O,s} / C_{R,s})$, can be rearranged to obtain the concentration of *R* at the electrode,

$$C_{R,s}(t) = C^{*}/\left(1 + \exp\left[\frac{nF}{RT}\left(E°\text{-}E(t)\right)\right]\right) \quad (7)$$

at a given time along the potential sweep in order to simulate the transient voltammetric response. Equation 7 is set as the boundary condition at the electrode (boundary 5 of Figure 5.4) in all transient simulations.

5.3.4 Quasi -Steady-State Voltammetric Response of Nanotrench Electrodes.

Figure 5.7 shows the voltammetric response of two gold nanoband electrodes (w = 40 nm (a) and 12.5 nm (b)) in a 5-mM Fc solution in MeCN containing 0.1 M $TBAPF_6$ at a scan rate of 50 mV/s before and after successive etchings in 3 M NaCl ($4V_{pp}$, 80Hz). As the gold band is etched, creating the nanotrench electrode, the limiting current decreases accordingly. This is in agreement with the results of the numerical simulations as well as predictions by equation 4. The limiting current decreases progressively with etching time, which is due to increasing mass-transfer resistance within the trench. As shown in Figure 5.7a, after 5 s of etching time the limiting current decreases to 48% of the initial current at the inlaid band and then to 13% after an additional 5 s and finally to 2.7% after a total of 15 s of etching. For the band of 40 nm width, this extent of decrease in limiting current after successive etchings corresponds to depths of 120, 740 and 4100 nm after 5, 10 and 15 s, respectively.

Etching of a 12.5-nm-wide band electrode shown in Figure 5.7b resulted in apparent trench depths of 30, 190, 320 and 2600 nm after 5, 10, 15 and 20 s, respectively. The etching rate of this narrower nanoband electrode appears to be somewhat slower than the rate seen for the 40-nm-wide band. It is not until after 25 s of etching (not shown in figure) that the

limiting current of the nanotrench electrode reaches ~1% of the initial current of the original inlaid band, which corresponds to an apparent depth of 4000 nm. This is most likely due to a greater mass-transfer resistance within the 12.5 nm trench. Consequently, a buildup of Au ions near the electrode surface in turn might decrease the overall rate of the Au oxidation. An increased mass transfer could lead to a higher etching rate with the 40-nm-wide nanotrench electrode. At extended etching times, greater than approximately 30s, the depth to width ratio, *d/w*, becomes too large (e.g., > 300) resulting in a distorted CV with a large positive sloping baseline as a transition to an ohmic response is seen. Nanotrench electrodes fabricated by this method have the advantage of being able to be revived after being over-etched. The electrodes are simply re-polished until a clean voltammogram returns with a limiting current once again equal to that of the inlaid band. Subsequent cycling in NaCl solution re-etches the band. The etching time needed for a specific desired depth is difficult to determine as nanoband electrodes fabricated using this method are prone to delamination as well as surface irregularities due to the inherent nature of the mechanical polishing step causing variations in etching rates. Further studies are needed to make a direct correlation between etching times and depth of recess for various nanoband widths.

5.3.5 Scan-Rate-Dependent Peak Current.

It has been previously shown[26-28] that the limiting current of a inlaid nanoband electrode deviates from what is predicted by equation 1 particularly at high scan rates where experimental values are found to be much greater than expected. For the narrowest of bands in their study, Nagale and Fritsch also found a negative deviation at scan-rates less than 5 V/s.[26] These behaviors were attributed to several possible reasons including: i) geometrical differences between the model of an inlaid planar band and their electrode design; ii)

electrode surface roughness from excess overhanging metal, cracks, recesses or delamination adding uncertainty to the actual exposed surface area; iii) the time dependent nature of equation 1 and the difficulty in accurately estimating the appropriate value for this parameter in potential sweep experiments; and iv) a general breakdown of the model particularly at narrow band widths, as discussed by White and co-workers.[12,29] In this last case, the failure of the model was ascribed to discontinuities in the concentration gradient near the electrode surface as a result of the finite size of a redox molecule and fluid inhomogeneity. Since this was seen predominately with a band width <10 nm, we set this size as our lower limit for our experiments and discussion. Here we also attempt to avoid the argument provided in case i) by fabricating inlaid planar band electrodes that more closely adhere to the original model design. Of particular concern in the above mentioned study[26] was the presence of overlapping and blocked diffusion layers due to a "dual-band" and "perpendicular-to-substrate" electrode design, respectively. Both of the physical limitations in cases i) and iv) may explain the negative deviation seen at intermediate to slow scan rates. However, the larger currents at faster scan rates are still rather puzzling. To remain consistent we define the time parameter in equations 1 and 4 as being equal to RT/Fv. Although this does not directly address the issue presented in case iii), we believe that the large divergence observed particularly at the highest scan rates would not be accounted for without arbitrarily choosing a value for time approximately two orders of magnitude faster than currently used. Numerical simulations agree very well with the maximum currents calculated using equations 4 and 8 indicating the time parameters chosen should be sufficiently accurate. This case is therefore not further considered. Here we focus our attention on the large positive deviations observed at the faster scan-rates. In an attempt to determine to what extent surface roughness and cracks, case ii),

attributes to the strong scan-rate dependence of the peak current the model for semi-infinite linear diffusion to a planar electrode is considered.[25]

$$i_p = 2.69 \times 10^5 n^{3/2} A D^{1/2} C^* v^{1/2} \quad (8)$$

At sufficiently fast scan-rates, planar diffusion would potentially dominate giving rise to a peak-shaped voltammogram. As previously discussed in the above mentioned study,[26] when experimental time scales are small the diffusion layer thickness would approach the size of delamination cracks and band surface roughness. The flux of redox species to the electrode surface within these cracks begins to contribute more significantly to the overall current of the electrode yielding areas calculated using equation 8 to be much greater than that of the geometric area. The nanotrench electrode geometry, in which the cross-sectional area of the recess is equal to the electrode area, may however be more suitable for studies designed to gain insight into the time dependent transition between radial and planar diffusion and any distortions in the voltammogram as a result of geometrical inconsistencies. Therefore we chose to revisit this topic using electrodes of this design where at fast time scales the diffusion layer thickness ($\delta = (2Dt)^{1/2}$) is less than the calculated depth of recess. This condition necessitates planar diffusion as the dominating contribution to the shape and intensity of the voltammogram.

Voltammograms were recorded at various scan-rates up to 1000 V/s for both inlaid and recessed nanoband electrodes. Figure 5.8 shows the results for a 12.5 nm width band (l = 0.96 mm, d = 1260 nm determined from measurements at 50 mV/s, Figure 5.8a). This depth is used for calculations in order to predict current expected at higher scan rates according to

equation 4. No significant scan-rate dependence was seen below 1 V/s for both the inlaid and recessed bands indicating quasi-steady-state response at slow scan rates. However, at faster scan-rates, > 5 V/s, the peak-shaped voltammogram is clearly dependent upon scan rate for both inlaid and recessed bands. Possible contributions to this effect may include variations in all of the following: i) capacitance charging current; ii) radial diffusion-limited quasi-steady-state current, modeled by equations 1 and 4; and iii) semi-infinite linear diffusion to a planar electrode modeled by equation 8. Due to their time/scan-rate dependent nature, it is often challenging to discern which factors make more significant contributions to the voltammogram shape and intensity.

In order to obtain a better understanding of the expected response, transient voltammetric responses were modeled using numerical simulations for the nanotrench electrodes. Simulated voltammograms of an electrode with similar dimensions to the one used in Figure 5.8 is now presented in Figure 5.9. As can be seen, Figure 5.9a displays a sigmoidal-shape voltammogram indicative of quasi-steady-state response. This was seen at nearly all scan-rates in this study up to 1000 V/s for the inlaid electrode, which is quite different than the peak-shaped response obtained experimentally above 5 V/s. As for the nanotrench electrode, peak-shaped voltammograms were generated from simulations at scan-rates greater than 100 V/s while a sigmoidal response is seen at lower scan-rates. This response is predicted by comparing the maximum current calculated from equations 4 and 8. When the scan-rate is less than 100 V/s, equation 4 predicts a maximum current closer to the experimental value because the diffusion layer thickness is much greater than the depth of the trench where radial diffusion can occur. At scan rates greater than 100 V/s, the diffusion layer thickness becomes on the order of the 1260 nm recess depth, which leads to transient

response from planer diffusion. Figure 5.10 shows concentration profiles within the trench at five points along the simulated voltammogram presented in Figure 5.9c for a scan-rate of 1000 V/s. The linear concentration profiles are seen within the trench and there is a nearly undisturbed bulk concentration of reduced species at the trench mouth. It is not until sufficient experimental time has passed (> 0.6ms) that the concentration outside the trench is noticeably decreased as can be seen at point 5 in Figure 5.10.

The background-corrected peak/maximum current for the data presented in Figure 5.8 (black points) and Figure 5.9 (open circles) was plotted as a function of square root of scan-rate in Figure 5.11a and b at scan-rates up to 1000 V/s. Theoretical maximum current calculated using equation 4 and equation 8 is shown as solid blue and red lines, respectively, in both figures for comparison. The theoretically predicted current coincides with the experimental data for inlaid bands only at slower scan-rates, < 1 V/s, and at approximately 100 V/s where the two curves cross over each other. At scan rates faster than 100 V/s, the linear dependence of the maximum current with $\nu^{1/2}$ (dashed line) indicates that there are increased contributions from linear diffusion. The magnitude of the experimental peak current is however ~40 times greater than expected based on the geometric area. In order to show the extent of which delamination may contribute to this behavior scanning electron microscopy (SEM) imaging was conducted. Figure 5.12 and Figure 5.13 show SEM images of 40nm inlaid band electrodes. It is clear that delamination is a concern and that this greatly contributes to the uncertainty in the response of both inlaid and recessed band electrodes. Although this situation is not ideal by any means the above ~40 fold increase in calculated surface area from Figure 5.11 is at the lower end of the surface roughness seen in a previous study by Caston and McCarley, where exposed area was found to be 20 to 500 times greater

than expected.[28] It is believed, however, that upon electrochemical etching protruding areas as well as portions of the electrode with delaminations would experience less mass transfer resistance and therefore faster etching rates. This should in turn cause a smoothing of the electrode so that the resulting electrode area is more close to the geometric area established in fabrication. At slow scan rates, for example < 1 V/s where a diffusion layer thickness is >50μm, the surface roughness/irregularity should not significantly affect the liming current and therefore not impact calculations of depth based upon CVs obtained at 50 mV/s. Although the peak current is still significantly larger than that calculated using equation 8 after etching, the area required to obtain a similar response is now less than 4 times greater than what is expected. This decrease leads us to believe that delamination cracks that extended into the electrode and protruding edges are smoothed, as expected, by the etching process. To further investigate the smoothing effect observed during etching, an inlaid nanoband electrode and its subsequent nanotrench electrode were scanned in 0.5 M H_2SO_4 in order to estimate the exposed gold surface area. The voltammograms recorded are presented in Figure 5.14. On the anodic scan the exposed gold surface is oxidized producing a broad peak from ~1.0 to 1.4V. A cathodic peak centered at ~0.67 V vs Ag/AgCl is seen on the return scan due to the reduction of gold oxide to Au. The area of this cathodic peak is used to estimate the exposed electrode area assuming a charge-to-area ratio of 386 μC/cm^2.[25, 30] For the unetched band Au area was calculated to be 4.7 x 10^{-5} cm^2 whereas after etching the area was calculated to be 2.0 x 10^{-7} cm^2. The nominal geometric area for this band taken from the thickness of gold deposited (12.5nm) and the length from the patterned Au edge measured optically (0.68mm) was found to be 8.5 x 10^{-8} cm^2. This corresponds to a surface roughness factor of approximately 550 and 2.4 for the inlaid band and trench electrodes

respectively. Again the surface roughness/excess exposed area due to delaminations of the inlaid band is substantial however the significant decrease in the calculated area for the nanotrench electrode is further verification of smoothing upon etching. Depending on the geometry and quality of the original inlaid band electrode, the extent of etching needed to smooth an electrode will vary. Assuming a uniform design; the fabrication of the nanotrench electrode results in an electroactive surface with the same geometric area as the cross-section of the recess. Electrodes of this design can be characterized by the diffusion-limited currents at slow scan-rates and by the relative intensity of peak-shaped voltammograms at various fast scan-rates.

5.4 Conclusions

We have demonstrated an easy method for the fabrication of a gold nanotrench electrode. The development of an analytical expression for the quasi-steady-state current of a nanotrench electrode has also been presented and verified through numerical simulation of its voltammetric response. The transient voltammetric responses of both inlaid and nanotrench electrodes show increased contribution from planer diffusion indicative of cracks, delaminations and overhanging Au. However, this effect is greatly reduced in nanotrench electrodes by a smoothing process during electrochemical etching. The nanotrench electrodes have potential application to the studies of mass-transport and electric double-layer effects. Additional application may include development of electrochemical biosensors in which significant analyte/substrate interaction is desired thus taking advantage of the geometry of the protruding trench walls.

5.5 Figures

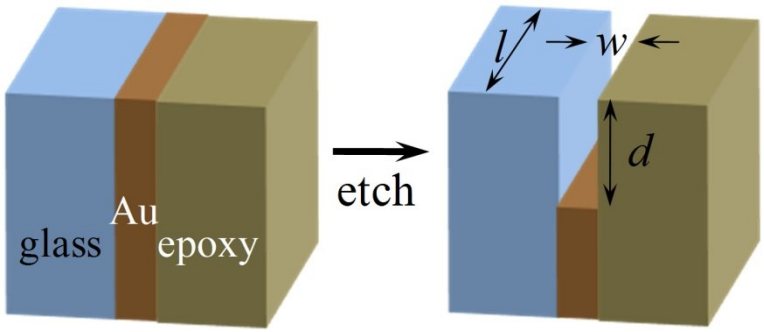

Figure 5.1 Fabrication of a gold nanotrench electrode.

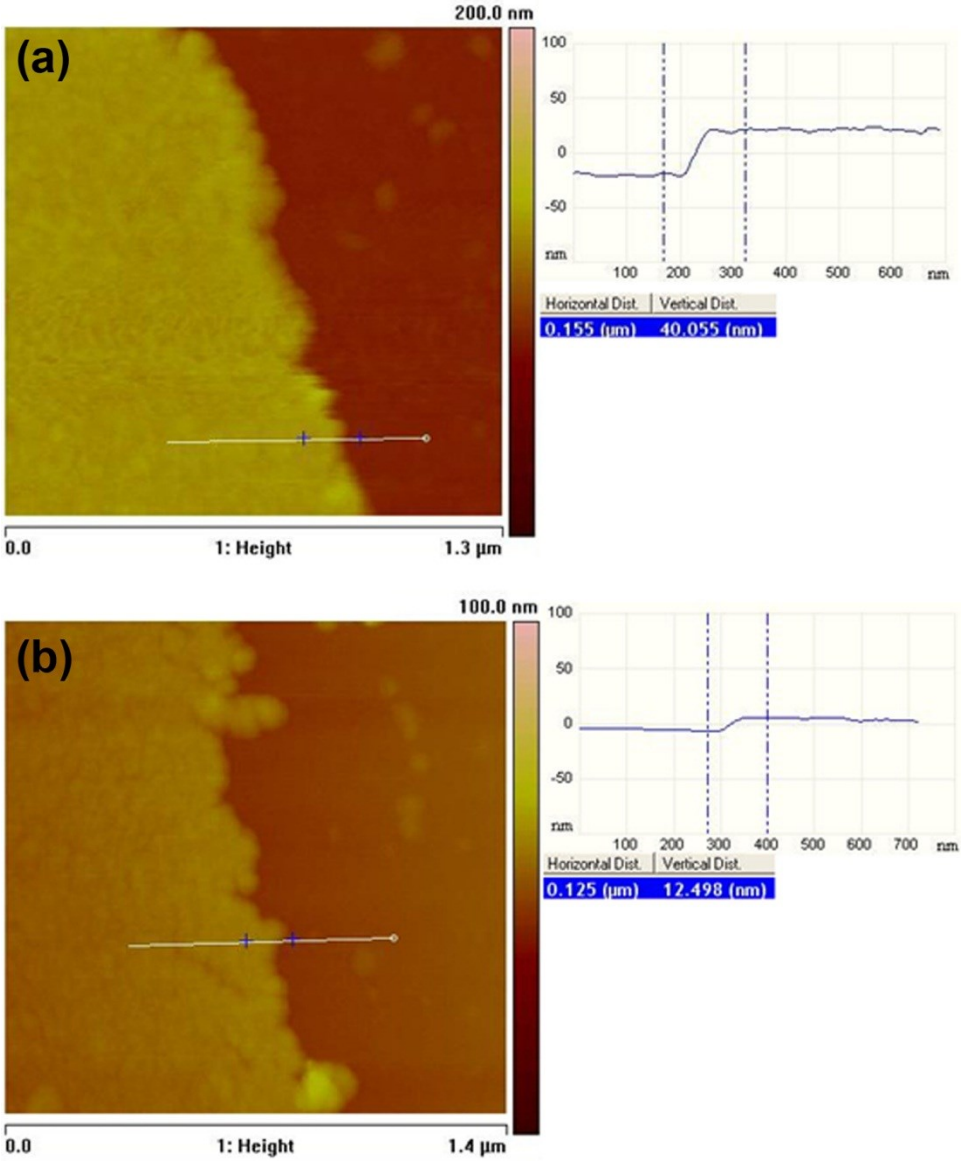

Figure 5.2 AFM images of Au film deposition.
AFM images showing the Au film thickness for the 40nm (a) and 12.5nm (b) depositions.

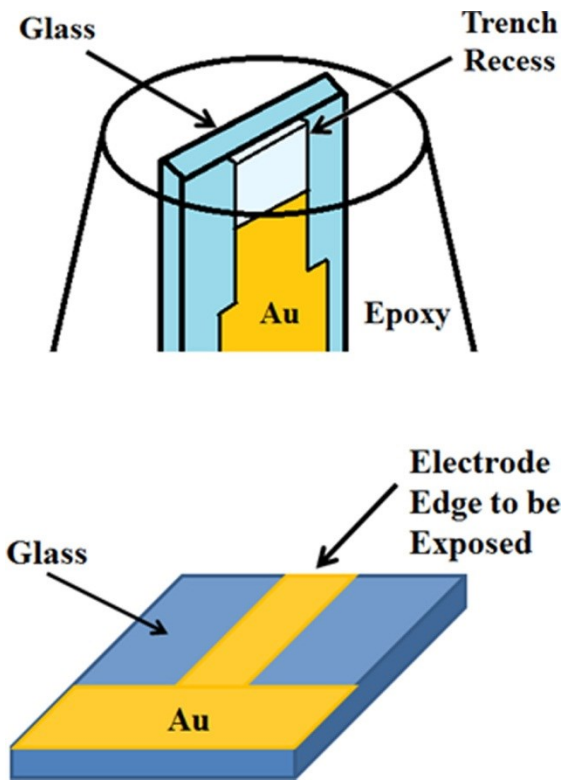

Figure 5.3 Diagrams showing the design of the patterned electrode.
Prior to Au deposition Scotch tape was used to mask sections of the glass where Au was not wanted.

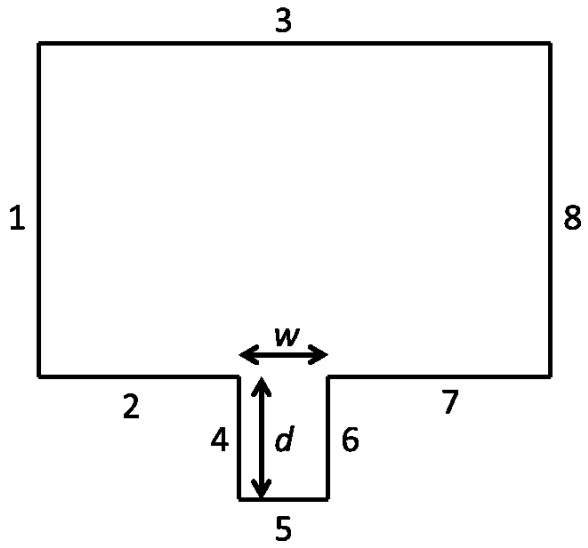

Figure 5.4 Simulation boundary conditions.
Nanotrench electrode 2D model used in COMSOL finite-element simulations with boundary conditions of C^* at boundaries 1, 3 and 8; *flux* = 0 from boundaries 2, 4, 6 and 7; and $C = 0$ (for steady state) at the electrode surface, boundary 5. See text for the time-dependent concentration expression used for boundary 5 for transient simulations.

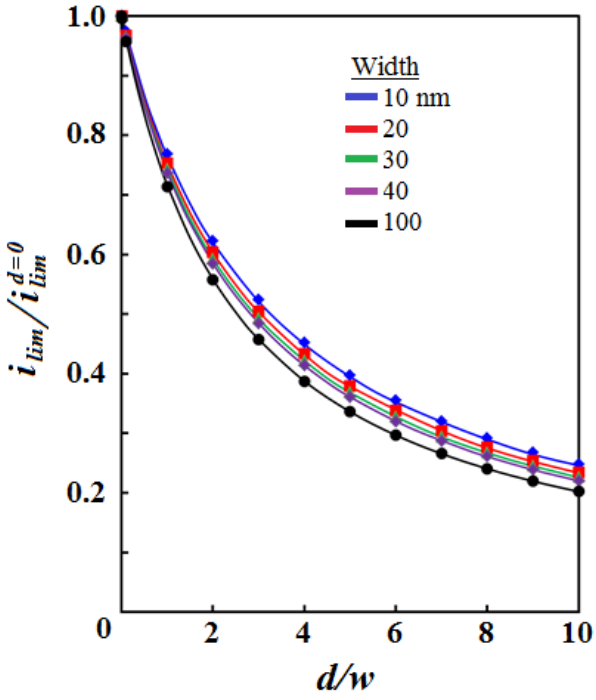

Figure 5.5 Simulated versus calculated limiting current of nanotrench electrodes. Comparison of finite-element simulation data (points) to theoretical calculations using Equation 4 (lines) for the normalized limiting current, $i_{lim}/i_{lim}^{d=0}$, of recessed nanoband electrodes as a function of width, *w* and normalized depth, *d/w*. $D = 2.47 \times 10^{-5}$ cm^2/s, $C^* = 5$ mM, $n = 1$, $v = 0.05$ V/s.

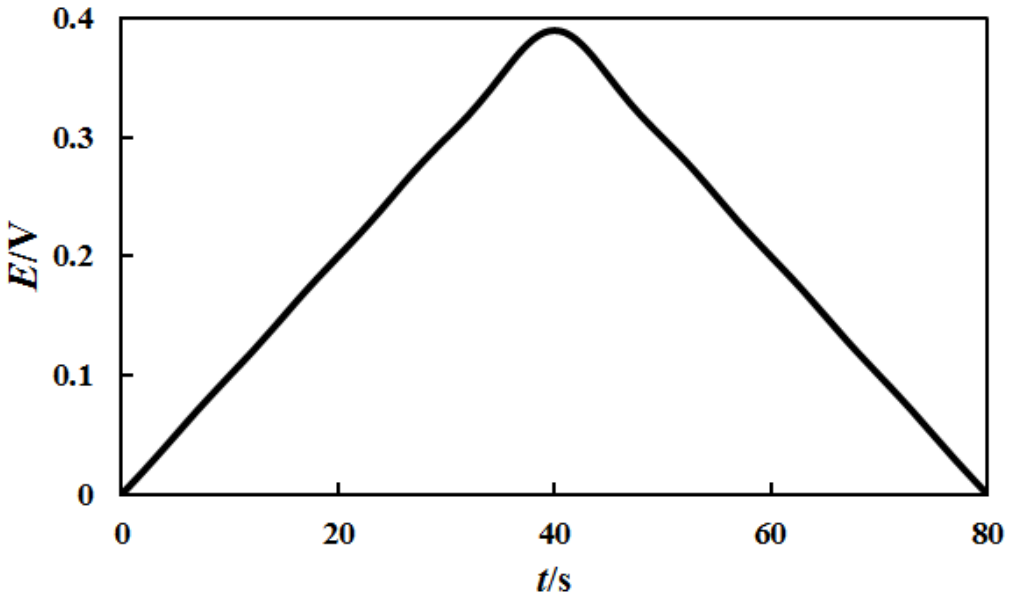

Figure 5.6 Triangle potential wave function.
Voltage-time plot prepared using equation 6 with k values from 0 to 7. E_{range} was set equal to 0.4V and a scan-rate of 0.01V/s was used.

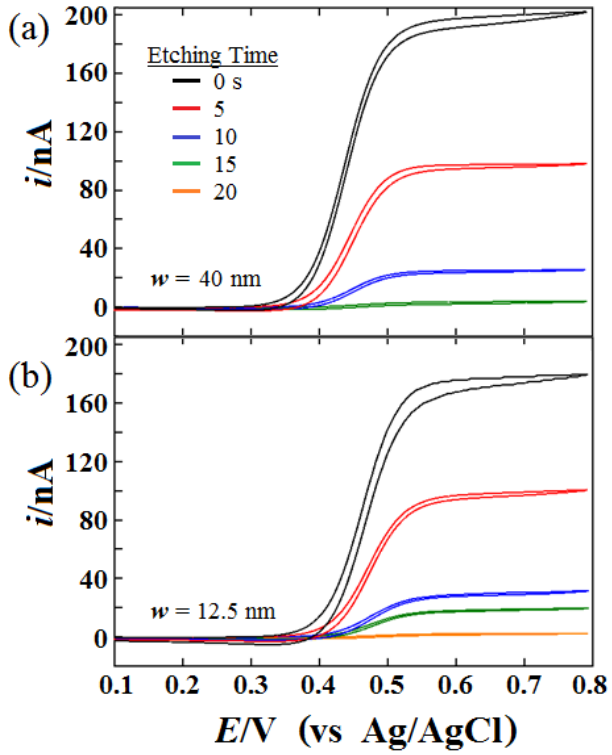

Figure 5.7 CVs of Au nanotrench electrodes.
Cyclic voltammograms of two gold nanoband electrodes (w = 40 nm (a) and 12.5 nm (b)) in 5mM Ferrocene, 0.1M $TBAPF_6$ in MeCN before (black), after 5s (red), 10s (blue), 15s (green) and 20s (orange, (b) only) total time of electrochemical etching in 3M NaCl.

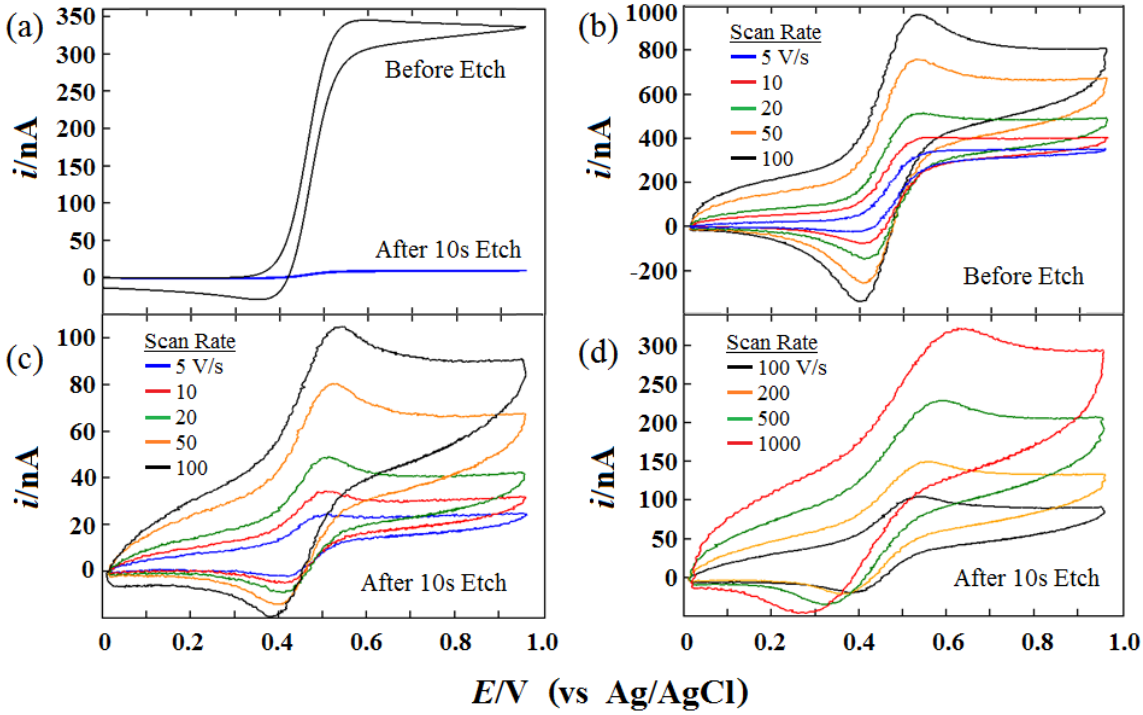

Figure 5.8 Scan-rate dependent CV response of Au nanotrench electrode.
Cyclic Voltammograms of a gold nanoband electrode (w = 12.5 nm, l = 0.96 mm) in 5mM Ferrocene, 0.1M $TBAPF_6$ in MeCN (a) before (black) and after (blue) electrochemical etching in 3M NaCl, (b) and (c) show the scan-rate dependence of the voltammetric response of the inlaid and etched band, respectively, at intermediate scan rates, and (d) of the etched band at fast scan rates. CVs in (a) were recorded at a scan-rate of 50 mV/s, all other CVs (b) – (d) scan-rates are noted on figure.

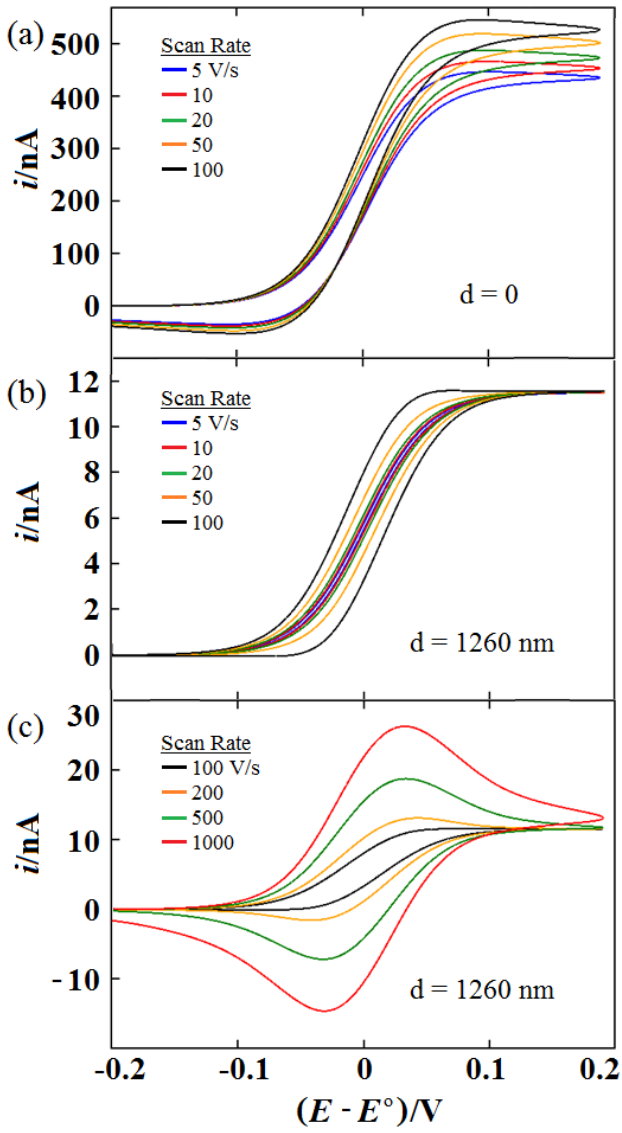

Figure 5.9 Simulated scan-rate dependent CV response of Au nanotrench electrode. Simulated cyclic voltammograms of an inlaid nanoband (a) and a recessed nanotrench (b) and (c) electrode (w = 12.5 nm, l = 1.0 mm). The same scan-rates as Figure 5.8 and the corresponding color scheme is presented here for ease of comparison.

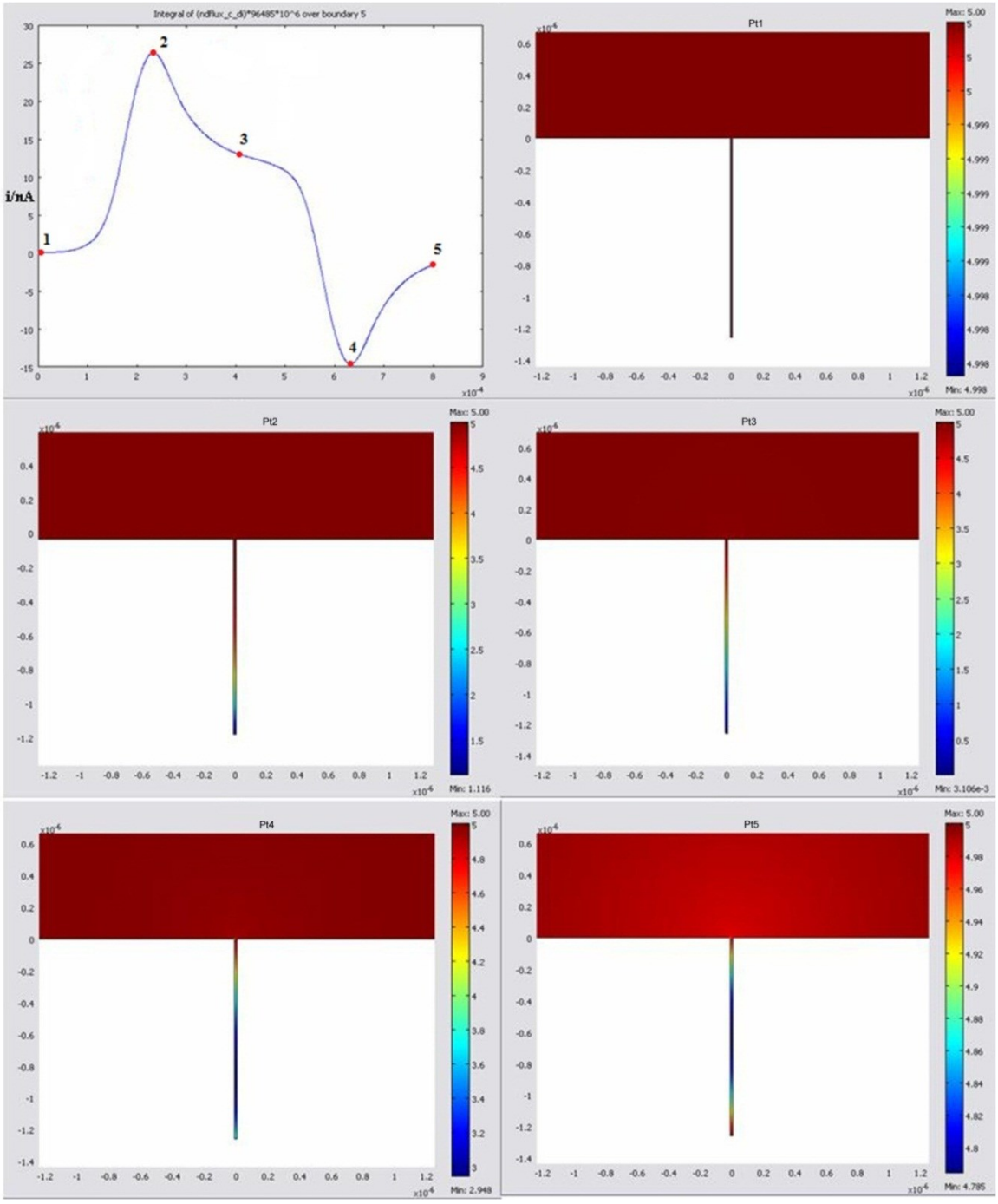

Figure 5.10 Transient COMSOL simulation concentration profiles.
Concentration profiles obtained from transient finite element simulations at five points (indicated as red dots) for a nanotrench electrode (w = 12.5 nm, d = 1260 nm, l = 1.0 mm). Dimensions are shown below in meters and concentration of reduced species in mol/L is shown in false color. The data presented here is from the same simulated response shown in Figure 5.9c for 1000V/s.

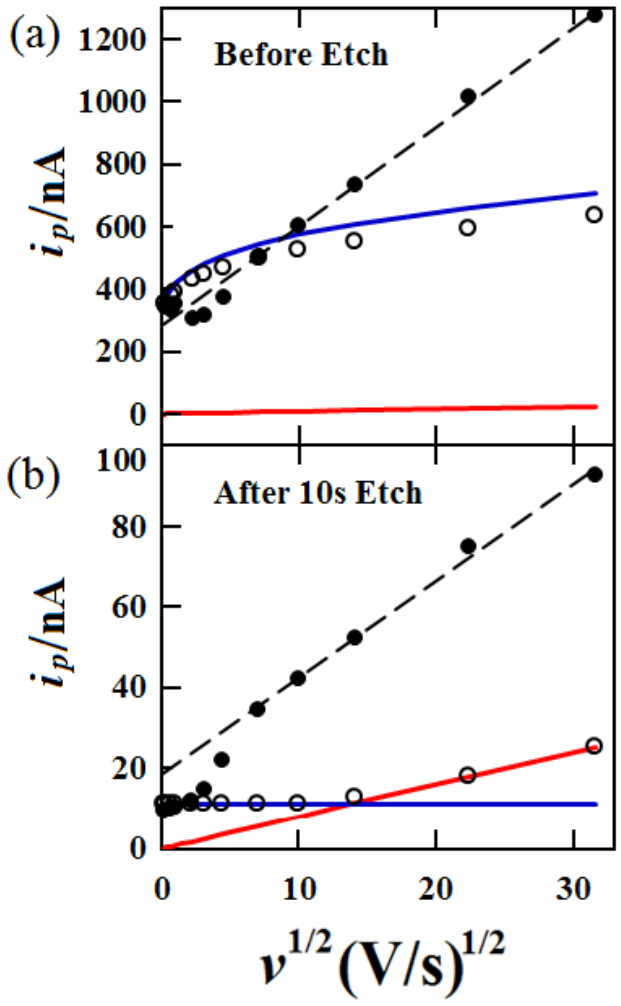

Figure 5.11 Experimental, simulated and theoretical nanotrench CV response.
Peak current as a function of square root of scan rate for the same inlaid (a) gold nanoband electrode (w = 12.5 nm, l = 0.96 mm) and etched nanotrench (b) electrode shown in Figure 5.8. The red solid line indicates theoretical peak current calculated based upon equation 8 and the blue lines are calculated using equations 1 and 4 assuming a depth of 1260 nm is accurate for (b). Open circles are maximum current from simulated voltammograms obtained from transient finite-element simulations. The black solid points and dashed lines represent baseline corrected experimental peak current and linear portion of experimental data at fast scan-rates, > 50 V/s.

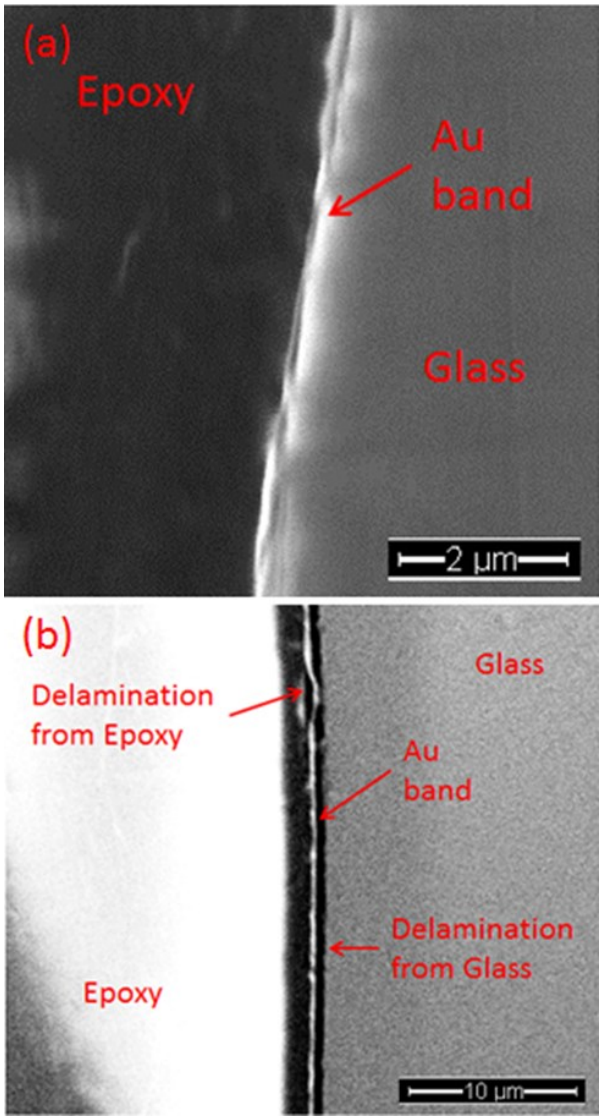

Figure 5.12 SEM micrographs of nanoband electrodes.
SEM images of 40nm inlaid nanoband electrodes showing that delamination is a contributing factor with the uncertainty in electrode geometry and therefore voltammetric response. In order to achieve higher contrast between Au band and insulating substrates these samples were not sputter coated prior to imaging.

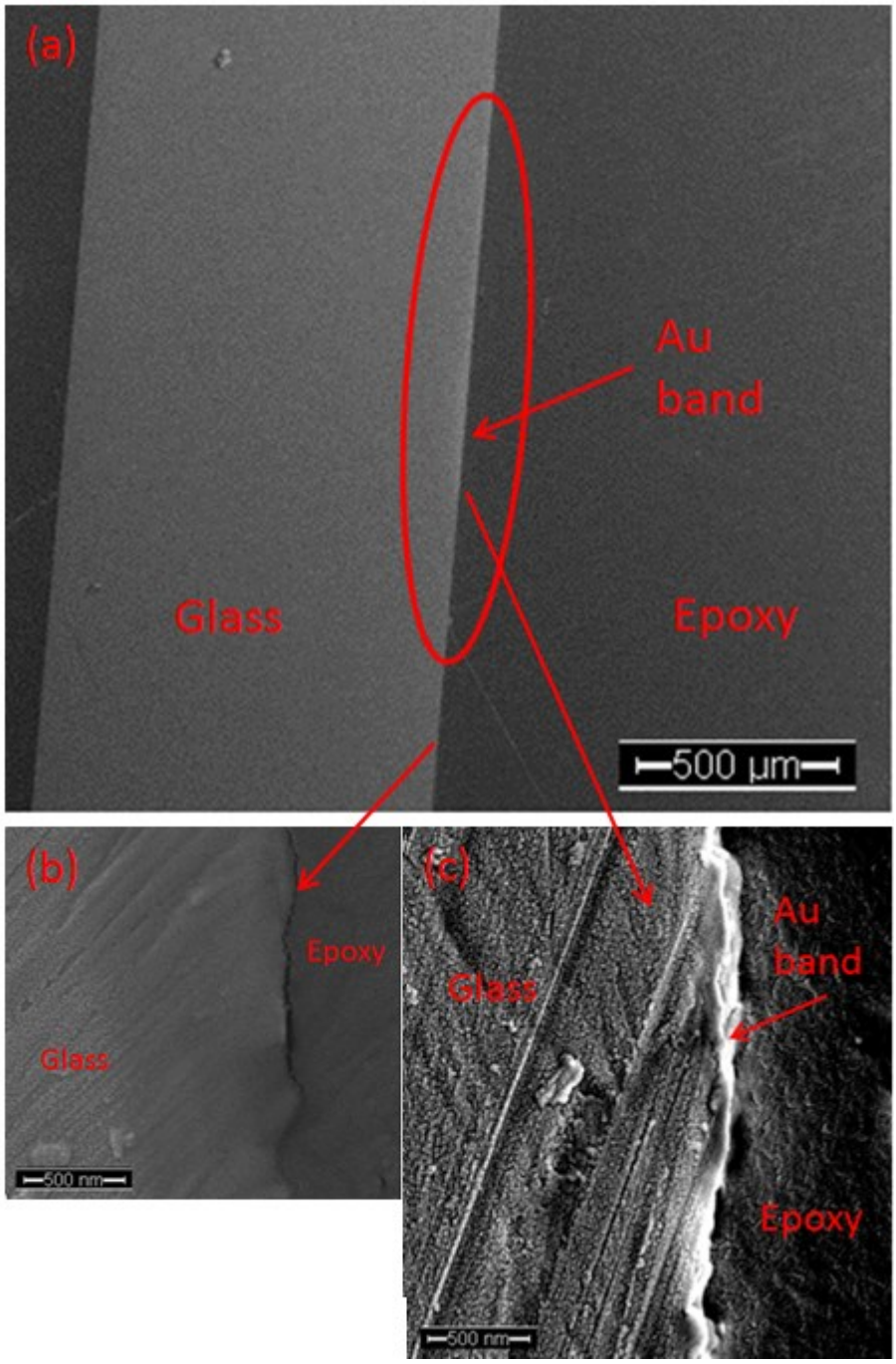

Figure 5.13 SEM images of Au nanoband electrode.
Scanning Electron Microscopy image of 40nm inlaid gold band electrode (a) showing a wide field of view. A section of glass/epoxy contact shown in (b) appears to have a tighter seal with less delamination than the glass/Au/epoxy section shown in (c). These samples were sputter coated prior to imaging.

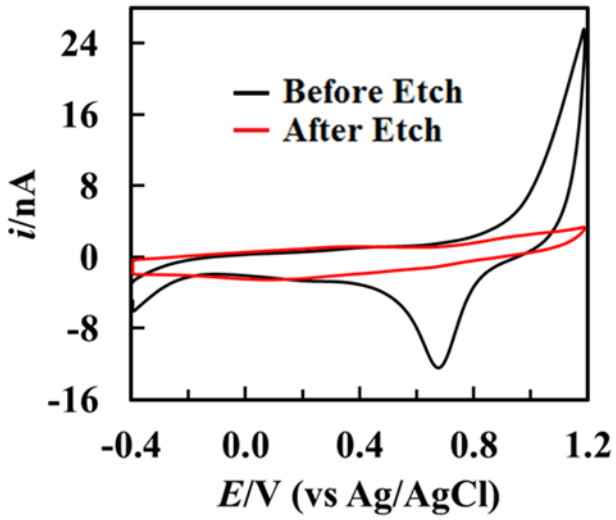

Figure 5.14 Nanoband/trench cycling in H_2SO_4.
Cyclic Voltammograms of a gold nanoband electrode (w = 12.5 nm, l = 0.68 mm) in 0.5M H_2SO_4 before (black) at 100 mV/s and after (red) at 500 mV/s electrochemical etching in 3M NaCl to a calculated depth of approximately 550nm. The depth of the trench was calculated using equation 5 from the extent of the decrease in limiting current from the voltammograms presented in Figure 5.15.

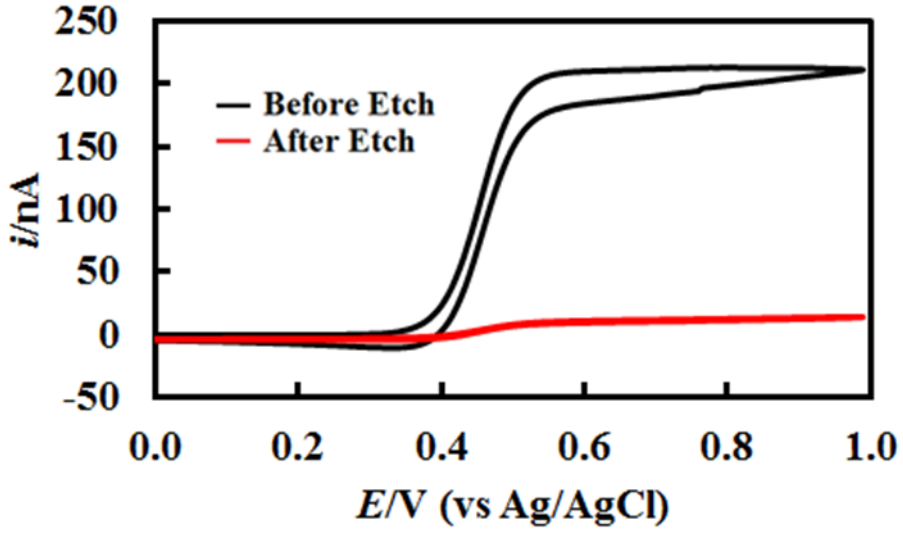

Figure 5.15 CV response of nanoband/trench electrode used in H_2SO_4 scans.
Cyclic Voltammograms of the gold nanoband electrode (w = 12.5 nm, l = 0.68 mm) in 5mM Ferrocene, 0.1M $TBAPF_6$ in MeCN before (black) and after (red) electrochemical etching in 3M NaCl. The extent of the decrease in current after etching corresponds to a trench depth of approximately 550nm calculated using equation 5. This is the same band/trench electrode presented in Figure 5.14.

5.6 References

(1) Zhang, B.; Zhang, Y. H.; White, H. S. *Anal. Chem.***2004,** *76*, 6229-6238.
(2) Sun, P. *Anal. Chem.* **2010,** *82*, 276-281.
(3) Li, Y. X.; Ito, T. *Anal. Chem.* **2009,** *81*, 851-855.
(4) Zhang, B.; Galusha, J.; Shiozawa, P. G.; Wang, G. L.; Bergren, A. J.; Jones, R. M.; White, R. J.; Ervin, E. N.; Cauley, C. C.; White, H. S. *Anal. Chem.* **2007,** *79*, 4778-4787.
(5) Wang, G. L.; Bohaty, A. K.; Zharov, I.; White, H. S. *J. Am. Chem. Soc.* **2006,** *128*, 13553-13558.
(6) Zhang, B.; Zhang, Y. H.; White, H. S. *Anal. Chem.* **2006,** *78*, 477-483.
(7) Wehmeyer, K. R.; Deakin, M. R.; Wightman, R. M. *Anal. Chem.* **1985,** *57*, 1913-1916.
(8) Nagale, M. P.; Fritsch, I. *Anal. Chem.* **1998,** *70*, 2902-2907.
(9) Wang, J.; Brennsteiner, A.; Sylwester, A. P.; Renschler, C. L. *Electroanalysis* **1991**, *3*, 505-509.
(10) Kim, Y. T.; Scarnulis, D. M.; and Ewing, A. G. *Anal. Chem.* **1986**, *58*, 1782-1786.
(11) Macpherson, J. V., Jones, C. E.; Unwin, P. R. *J. Phys. Chem. B*, **1998**, *102*, 9891-9897.
(12) Morris, R. B.; Franta, D. J.; White, H. S. *J. Phys. Chem.* **1987**, *91*, 3559-3564.
(13) Aguilar, Z. P.; Vandaveer, W. R.; Fritsch, I. *Anal. Chem.* **2002,** *74*, 3321-3329.
(14) Kovach, P. M.; Caudill, W. L.; Peters, D. G.; Wightman, R. M. *J. Electroanal. Chem.* **1985,** *185*, 285-295.
(15) Weiland, J. D.; Anderson, D. J.; Pogatchnik, C. C.; Boogaard, J. J. *Proc. 19th Annu. Int. Conf. IEEE EMBS* **1997**, 2273–2276.
(16) Rubinstein, J. T.; Spelman, F. A.; Soma, M.; Suesserman, M. F. *IEEE Trans. Biomed. Eng.***1987,** *34*, 864-875.
(17) Lanyon, Y. H.; Arrigan, D. W. M. *Sens. Actuators B* **2007,** *121*, 341-347.
(18) Menke, E. J.; Thompson, M. A.; Xiang, C.; Yang, L. C.; Penner, R. M. *Nat. Mater.* **2006,** *5*, 914-919.
(19) Xiang, C. X.; Kung, S. C.; Taggart, D. K.; Yang, F.; Thompson, M. A.; Guell, A. G.; Yang, Y. A.; Penner, R. M. *ACS Nano* **2008,** *2*, 1939-1949.
(20) Davies, T. J.; Hyde, M. E.; Compton, R. G. *Angew. Chem. Int. Ed.* **2005,** *44*, 5121-5126.
(21) Liu, H. Y.; Fan, F. R. F.; Bard, A. J. *J. Electrochem. Soc.* **1985,** *132*, 2666-2668.
(22) Maeda, M.; White, H. S.; McClure, D. J. *J. Electroanal. Chem.* **1986,** *200*, 383-387.
(23) Samuelsson, M.; Armgarth, M.; Nylander, C. *Anal. Chem.* **1991,** *63*, 931-936.
(24) Lee, C. Y.; Tan, Y. J.; Bond, A. M. *Anal. Chem.* **2008,** *80*, 3873-3881.

(25) Bard, A. J.; Faulkner, L. R. *Electrochemical Methods*. 2nd ed.; John Wiley & Sons: New York, 2001.
(26) Nagale, M. P.; Fritsch, I. *Anal. Chem.* **1998,** *70*, 2908-2913.
(27) Henry, C. S.; Fritsch, I. *J. Electrochem. Soc.* **1999,** *146*, 3367-3373.
(28) Caston, S. L.; McCarley, R. L. *J. Electroanal. Chem.* **2002,** *529*, 124-134.
(29) Seibold, J. D.; Scott, E. R.; White, H. S. *J. Electroanal. Chem.* **1989,** *264*, 281-289.
(30) Cadle, S. H.; Bruckenstein, S. *Anal. Chem.* **1974,** *46,* 16-20.

CHAPTER 6
Scan-Rate-Dependent Current Rectification of Cone-Shaped Silica Nanopores*

6.1 Introduction

The nonlinear current-voltage (*i*-*V*) response of both biological and artificial nanopores has received considerable interest in the past decades[1-5] due to its importance in many areas such as micro-/nanofluidics[6] and protein biophysics. The nonlinear *i*-*V* response, or current rectification, has been generally assumed to originate from the asymmetric distribution of surface charges on the pore walls.[3] There have been numerous reports in recent literature concerning both the origin of the current rectification of nanopores[1,3,7-9]and the control of the ionic/molecular transport properties of nanopores by studying their rectification behavior.[6]

We have recently been interested in studying the voltammetric response of cone-shape silica nanopores as a function of scan rate, ν. As recently reported by White and Bund, [4] the current rectification behavior of a cone-shape glass nanopore is mainly due to a change in the ionic conductivity in the vicinity of the pore mouth at varying bias voltages. We therefore believe that such a change in the ionic conductivity at the pore mouth should involve a process of dynamic reorganization of the ionic species at different bias voltages. Normally, this reorganization process is fast and unnoticeable under conventional experimental conditions, such as measurements with discrete voltages or low voltage scan

---

* This chapter is adapted with permission from Guerrette, J. P. & Zhang, B. Scan-Rate-Dependent Current Rectification of Cone-Shaped Silica Nanopores in Quartz Nanopipettes. *J. Am. Chem. Soc.* **2010**, 132, 17088-17091. Copyright (2010) American Chemical Society.

rates. Under these conditions, the *i*-*V* response of a cone-shaped nanopore shows the most significant rectification behavior, which is normally independent of ν and the initial voltage. It can be described as a "steady-state" response. However, we have found that at very high scan rates (e.g., V > 200 V/s), the *i*-*V* response of a cone-shaped silica nanopore starts to show a strong dependence on both the scan rate and the initial voltage. In fact, the resulting *i*-*V* response under such conditions shows considerable ohmic behavior. A clear transition from strong rectification behavior to a nearly ohmic response with increasing scan rate has been observed. Furthermore, we have found that the *i*-*V* response is strongly dependent on the initial bias voltage of the voltage scan. The overall slope of the nearly linear *i*-*V* response is close to the slope at the starting voltage when the scan rate is above ~200 V/s. These results strongly suggest that current rectification of a cone-shaped silica nanopore could originate from a dynamic ionic reorganization process in the vicinity of the pore orifice under the influence of a changing bias voltage.

6.2 Experimental Section

6.2.1 Preparation of cone-shape silica nanopores by laser pulling.

The cone-shape silica nanopores were fabricated using a CO_2 laser puller (Sutter Instrument Co., Model P-2000). A 7.5-cm-length quartz capillary (Sutter Instrument Co., 1.0 mm outer diameter, 0.70 mm inner diameter w/ filament) was pulled into two sharp tips using the P-2000. The following program was used: heat = 750, filament = 4, delay = 145, pull = 175 and velocity was varied from 35 to 90 in order to produce pores of different size. The slower pulling program (velocity = 35) achieved pore with diameters of approximately 20-nm while pulls with velocity = 90 achieved pores with diameters in the 4 to 8-nm range. The pores were then filled with the corresponding electrolyte solution using a MicroFil

pipette filler (World Precision Instruments Inc., MF34G-5). Nanopores were set aside and allowed to completely fill by capillary action for a minimum of 10 minutes before use. The presence of a filament within the capillary aided in the filling process.

6.2.2 Electrochemical recording of the *i-V* response of individual silica nanopores.

All potentials reported herein are with respect to a Ag/AgCl electrode inside the capillary versus a Ag/AgCl electrode in the bulk solution on the exterior of the pore. The determination of nanopore diameter was achieved by recording the *i-V* response of each pore for a potential sweep between +500 and -500 mV at a scan rate of 500 mV/s in a 1M KCl solution containing 10 mM NaCl, 10 mM Tris and 1 mM EDTA. The *i-V* response was recorded by using a EG&G PAR Model 175 Universal Programmer and a Dagan Chem-Clamp Voltameter/Amperometer as a potentiostat interfaced to a PCI-6251 data acquisition system (National Instruments) and a Dell computer with in-house LabView software (National Instruments). Once characterized, both inside and outside of the pores were flushed with copious amounts of water and the pores were refilled using the desired electrolyte solution. Fast-scan current-time traces were recorded using a Digidata 1440A low noise data acquisition system with AxoScope 10.2 software (Molecular Devices) as the potential was swept between +1 and -1 V at scan rates between 5 and 1000 V/s. These current-time traces were then converted into current-potential responses accordingly.

6.3 Results and Discussion

Individual cone-shaped silica nanopores with diameters in the range of 4-25 nm were prepared by a laser-pulling process.[10] Both the diameter and the half-cone angle can be approximately adjusted in the laser pulling process. Depending on the pulling process, a

silica nanopore can have a half-cone angle usually between 5^o to 10^o. The size of a cone-shape silica nanopore was determined by measuring its ionic resistance in an electrolyte solution (e.g., 1 M KCl).[11] Figure 6.1a shows a scanning electron microscopy (SEM) image of a typical silica nanopore prepared using a laser puller. Figure 6.1b shows the *i-V* response of a 4.6-nm silica nanopore at ν = 10 mV/s in three different KCl solutions. The rectification factor, which is defined by the ratio between the current at -0.5 V and that at +0.5 V, has been measured to be 4.9, 3.6, and 1.8, for the 10, 100, and 1000 mM KCl solutions, respectively. The smaller rectification factor in the 1 M KCl solution can be qualitatively explained by the absence of overlap in the electrical double layer in the vicinity of the nanopore mouth due to the sufficiently high concentration of electrolyte.

In order to study the scan-rate-dependent voltammetric response of a cone-shape silica nanopore, a triangle voltage waveform was applied across the nanopore using a pair of Ag/AgCl electrodes and a functional generator. The nanopore pipette was filled with the same electrolyte solution as in the bulk. A voltage scan range of 2 V (-1 $\leftrightarrow$ +1 V) has been used in all cases. Representative *i-V* responses can be found in Figure 6.2. It is important to mention that at high scan rates, the *i-V* response of a cone-shaped silica nanopore typically involves a large capacitance charging current that is mainly due to the system capacitance. This results in a capacitance charging current of ~2.7 nA at a scan-rate of 200 V/s, corresponding to a capacitance of the system, C_{sys}, equal to ~13 pF. The measured ion current sits on top of this capacitance current. When a scan is initiated or the scan direction is changed, this capacitance charging current increases rather quickly and reaches a steady state. In the case of Figure 6.2, for example, it takes less than 0.5 ms for the capacitance charging current to reach the steady state, which corresponds to <100 mV on the voltage

scan. In order to make better comparisons between different scan rates avoiding interference from the increasing charging current, all of the *i-V* responses have been plotted over a 1 V scan range (from -0.5 to +0.5 V).

Figure 6.3a-c shows the *i-V* responses between -0.5 and +0.5 V of a 10 nm silica nanopore in Tris buffer solutions containing KCl of three different concentrations (10, 100, and 1000 mM, respectively). The concentration of buffer has been kept at 1% of the KCl concentration in all solutions. The same voltage waveform (0 → +1 V → -1 V → 0 V) was applied in all cases. It is worth mentioning that no significant difference in the *i-V* responses was observed for $\nu < 5$ V/s. Thus, only the scan rates between 5 and 1000 V/s have been displayed in Figure 6.3. At low scan rates, the nanopore showed the greatest current rectification effect. As ν was increased, a clear transition from a strongly rectifying response to a nearly ohmic *i-V* response was observed at 10 and 100 mM (Figure 6.3a,b). Interestingly, the rectification response of the same nanopore in the 100 mM KCl solution was found to be similar to that of the 10 mM solution. A similar transition was observed in the 100 mM solution, as shown in Figure 6.3b. The nanopore showed nearly linear *i-V* response in 1 M KCl at all scan rates as a result of the smaller double-layer thickness ($\kappa^{-1} \approx 0.3$ nm[12]). Figure 6.3d summarizes the results shown in Figure 6.3a-c as a plot of the rectification factor as a function of ν for three KCl solutions. As shown in Figure 6.3d, the rectification factor decreased as the scan rate increased in the first two solutions. The decrease in the rectification factor was more obvious for the 10 mM KCl solution (from 3.8 to 1.2) than for the 100 mM solution (from 4.0 to 1.7). The rectification factor remained nearly constant at ~1.0 for the 1000 mM KCl solution, indicating nearly ohmic behavior.

More interestingly, the *i-V* response of a silica nanopore has been found to be strongly dependent on the initial voltage of the waveform at high scan rates. For example, Figure 6.4a,b shows the *i-V* responses of a 10 nm silica nanopore in 10 mM KCl for two different voltage waveforms. A starting voltage of -0.8 V was used in Figure 6.4a, which shows that as ν was increased, the overall *i-V* response was nearly ohmic with a slope very close to that at -0.5 V. However, as shown in Figure 6.4b, when an initial voltage of +0.8 V is used, the overall *i-V* response at high scan rates was also nearly linear but with a slope very close to that at +0.5 V. In fact, one can see that the effective conductance of the nanopore in Figure 6.4a was significantly higher than that in Figure 6.4b, although the only difference between the two conditions was a different starting voltage. We believe that at very high scan rate, the *i-V* response of a charged conical nanopore is likely determined by the distribution of freely moving ions at the mouth of the nanopore *at the initial voltage*. Because the voltage perturbation is applied in an ultrashort time, the distribution of the freely moving ions may not have sufficient time to change, which would produce a nearly constant ionic resistance at all voltages in the scan (an ohmic response). A schematic has been given in Figure 6.5 to further explain the above two cases. When the voltage is scanned from a negative voltage, there should be fewer K^+ ions at the pore mouth, corresponding to a smaller ionic resistance. Therefore, a greater slope in the *i-V* response would be expected, as illustrated in Figure 6.5 with the green curve. However, when the voltage scan starts from a positive value, where the density of K^+ is at its maximum over the entire scan, a smaller slope should be obtained in the *i-V* curve because of a greater ionic resistance, as depicted with the red curve in Figure 3. Such nearly linear responses, however, can only be observed if the entire voltage scan is

finished within an ultrashort time in which the redistribution of the ionic species is minimized in the vicinity of the nanopore mouth.

Since the slope of the nearly linear *i-V* curve of a silica nanopore is believed to reflect the ionic distribution at the initial voltage, it should change after the voltage perturbation is removed. It was thus interesting to study the *i-V* response of silica nanopores under continuous voltage scans. Figure 6.6 shows comparisons between the *i-V* curves for the first and 5000^{th} scan at ν = 1000 V/s of an 8.7 nm silica nanopore in 10 mM KCl at pH 7.4 with three different initial voltages. First, no significant difference between the first and 5000^{th} scan was observed when the scan was started at 0 V. This is because the distribution of ions is not shifted with a starting voltage of 0 V. When the scan was started at +0.8 V, however, the slope of the *i-V* response increased to that of the 0 V starting voltage, indicating that the distribution of ions in the nanopore had returned to its "natural" state within 5000 scans. In the case of a starting voltage of -0.8 V, the slope of the *i-V* response was observed to decrease with time, as expected. However, the rate of the slope change is significantly lower than that of the +0.8 V case. This slower transition is not fully understood but could be due to a slower building-up process of the excess K^+ back to the vicinity of the nanopore orifice when the negative voltage is removed, as compared to the quick diffusion of K^+ out of the pore mouth from a higher concentration when a positive voltage is removed.

We have studied cone-shape silica nanopores of other diameters in the range of 4-25 nm (Figure 6.7). No attempts were made in this study to investigate nanopores smaller than 4 nm or greater than 25 nm in diameter. A decrease in the rectification factor was observed in all of the nanopores in 10 mM KCl as the scan rate was increased. In addition, we have studied scan rate dependent current rectification of cone-shaped silica nanopores in other

electrolyte solutions and found that the decrease in the rectification factor with increasing scan rate is not limited to KCl. For example, Figure 6.8a shows the *i-V* response of a 4.2-nm silica nanopore in a 0.1mM Tris buffer solution at pH 7.4 containing 10 mM $CaCl_2$ at scan rates from 10 to 1000 V/s. Figure 6.8b is the rectification factor corresponding to the data in Figure 6.8a plotted as a function of the scan rate. The rectification factor has been found to decrease from 2.5 at 10 V/s to 1.1 at 1000 V/s.

On the basis of the recent simulation results of White and Bund[4] and our experiments, we believe that a dynamic ionic redistribution could be responsible for the change in ionic conductivity and the observed current rectification behavior for cone-shape silica nanopores. There have been numerous reports showing that the local concentration of an ionic species can be dramatically regulated in a cone-shaped glass nanopore even by a small voltage bias.[13-15] For example, Clarke et al.[13] showed that the concentration of a charged fluorescent dye in a glass nanopore can be increased by ~3000 times under a small bias voltage. Using fluorescent microscopy, they also showed that these charged molecules are in fact loosely localized at the pore mouth: a region of 8 μm from the pore mouth was measured under a 2 V bias voltage.[13]

The fact that a smaller rectification factor was observed under high ν suggests that the redistribution of such concentrated ionic species in the nanopore can be sluggish relative to a quickly changing voltage perturbation. The redistribution process of ionic species can be driven by diffusion, migration, and electroosmosis, the rates of all of which are proportional to the diffusivity of the ionic species, *D*. The length that K^+ ions ($D \approx 2 \times 10^{-9}$ m^2/s[16]) can diffuse in the time duration of a voltage scanning experiment at 100 V/s was estimated to be $\delta \approx 1.0$ μm, as determined using the Einstein relationship $\delta = (2Dt_{exp})^{1/2}$, where t_{exp} is the time

duration of the voltammetric experiment.[17] In fact, a smaller diffusion coefficient of K^+ and therefore a smaller diffusion length δ can be anticipated in the vicinity of the nanopore mouth because of the high concentration. Without considering migration and electroosmosis, however, this simple calculation indicates that the distribution of the freely moving K^+ ions could be largely unchanged at the nanopore mouth, assuming the excess K^+ occupies a similar region as reported by Clarke et al.[13] On the other hand, when a low scan rate (e.g., 0.1 V/s) is used, these ions would have sufficient time to redistribute inside the nanopore during the voltage scan. Under such conditions, the silica nanopore would exhibit regular current rectification behavior.

6.4 Conclusions

In summary, we have studied the *i-V* response of cone-shaped silica nanopores in KCl solutions at high scan rates. Our results have shown that current rectification of a cone-shaped silica nanopore depends strongly on the rate of the voltage scan. At low scan rates, the nanopore exhibits strong rectification behavior. As the scan rate is increased, the *i-V* response shows nearly ohmic behavior. In addition, we have shown that at very high scan rates, the *i-V* response of a cone-shaped silica nanopore is largely determined by the initial voltage and has a slope close to that at the starting voltage. On the basis of these results, we believe that voltage-driven dynamic ion redistribution could be responsible for the current rectification behavior observed in cone-shaped silica nanopores. This redistribution can be slower than the rate of the voltage perturbation under ultrafast voltammetric conditions, which may explain the nearly ohmic behavior of silica nanopores.

6.5 Figures

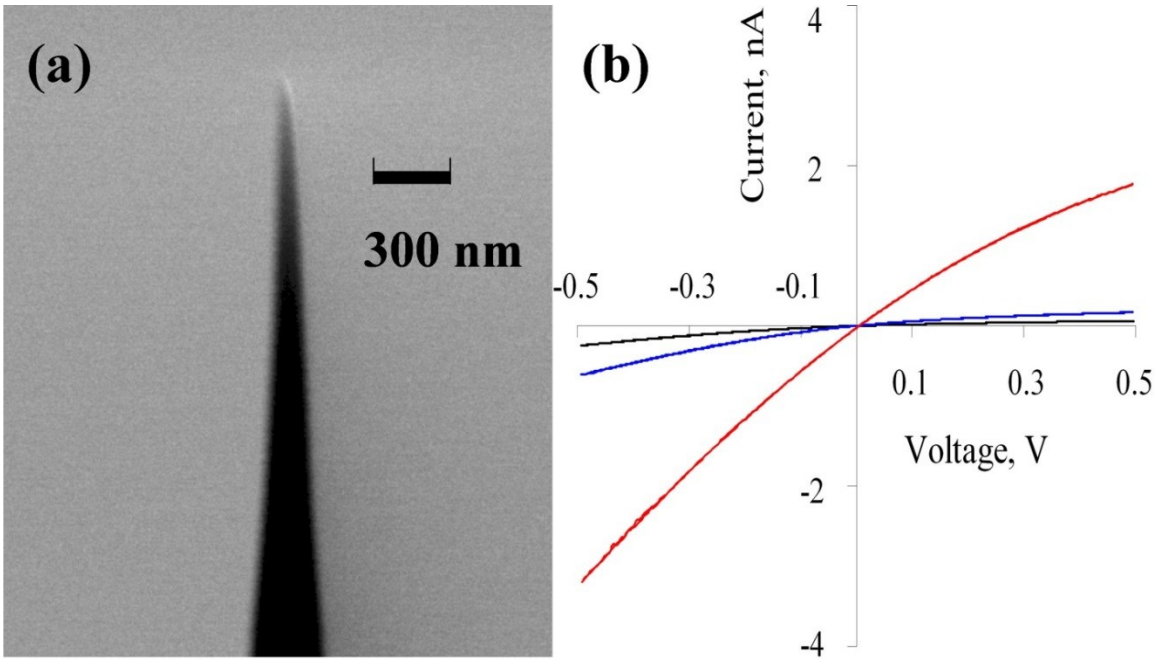

Figure 6.1 SEM image of representative nanopore.
(a) An SEM image of a typical silica nanopore pipette, and (b) *i*-*V* responses of a 4.6-nm nanopore at 10 mV/s in 0.1 mM Tris buffer (pH = 7.4) and 10 mM KCl (black), 1 mM Tris buffer (pH = 7.4) and 100 mM KCl (blue), 10 mM Tris buffer (pH = 7.4) and 1000 mM KCl (red) solutions.

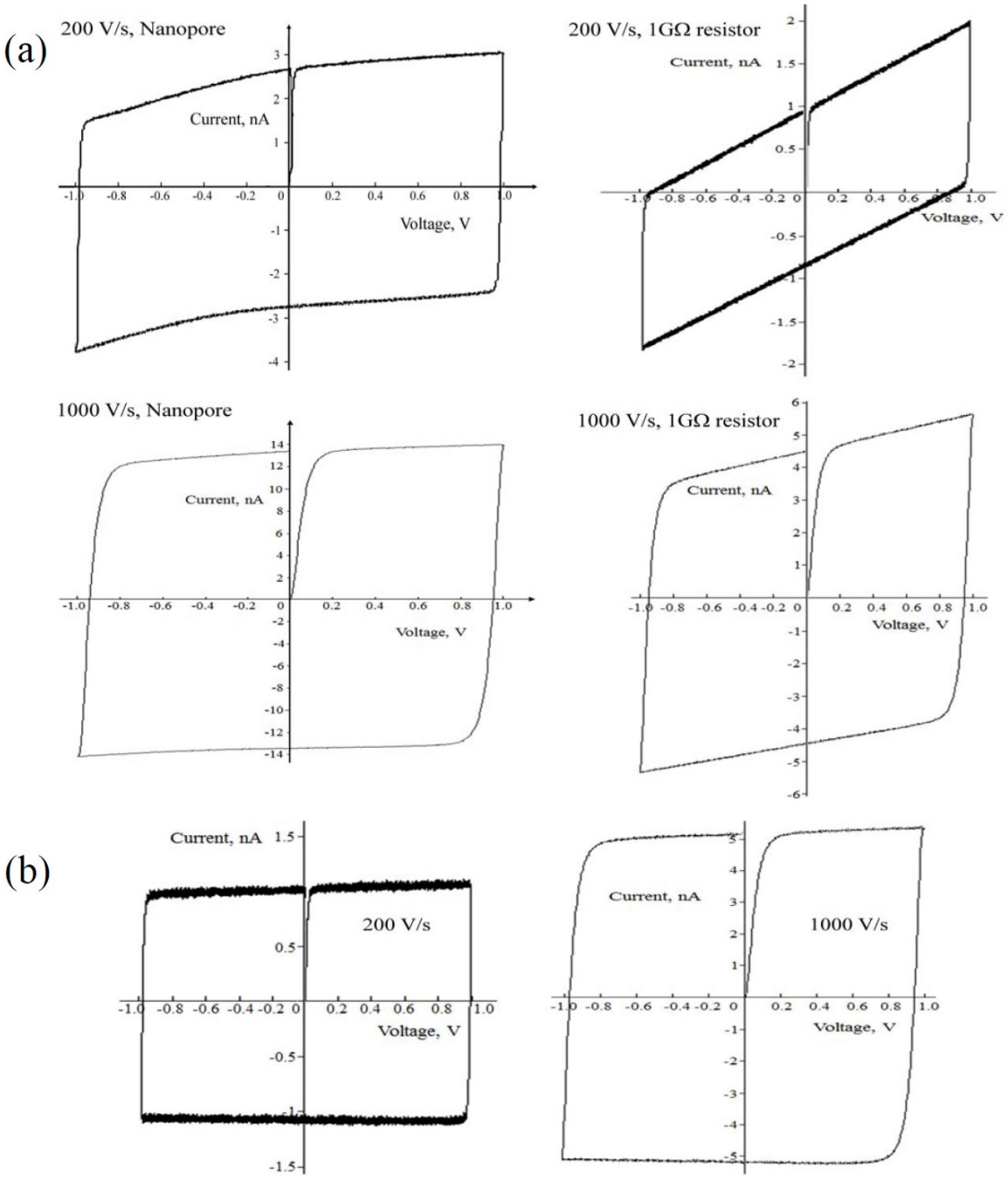

Figure 6.2 Comparison of cell response with pore, resistor and at open circuit.
(a) *i-V* response at 200 V/s and 1000V/s of a 10-nm nanopore in a 10-mM KCl solution containing 0.1 mM Tris buffer at pH 7.4 and a 1 GΩ resistor. (b) *i-V* response at 200 V/s and 1000V/s of the electrochemical cell at open circuit.

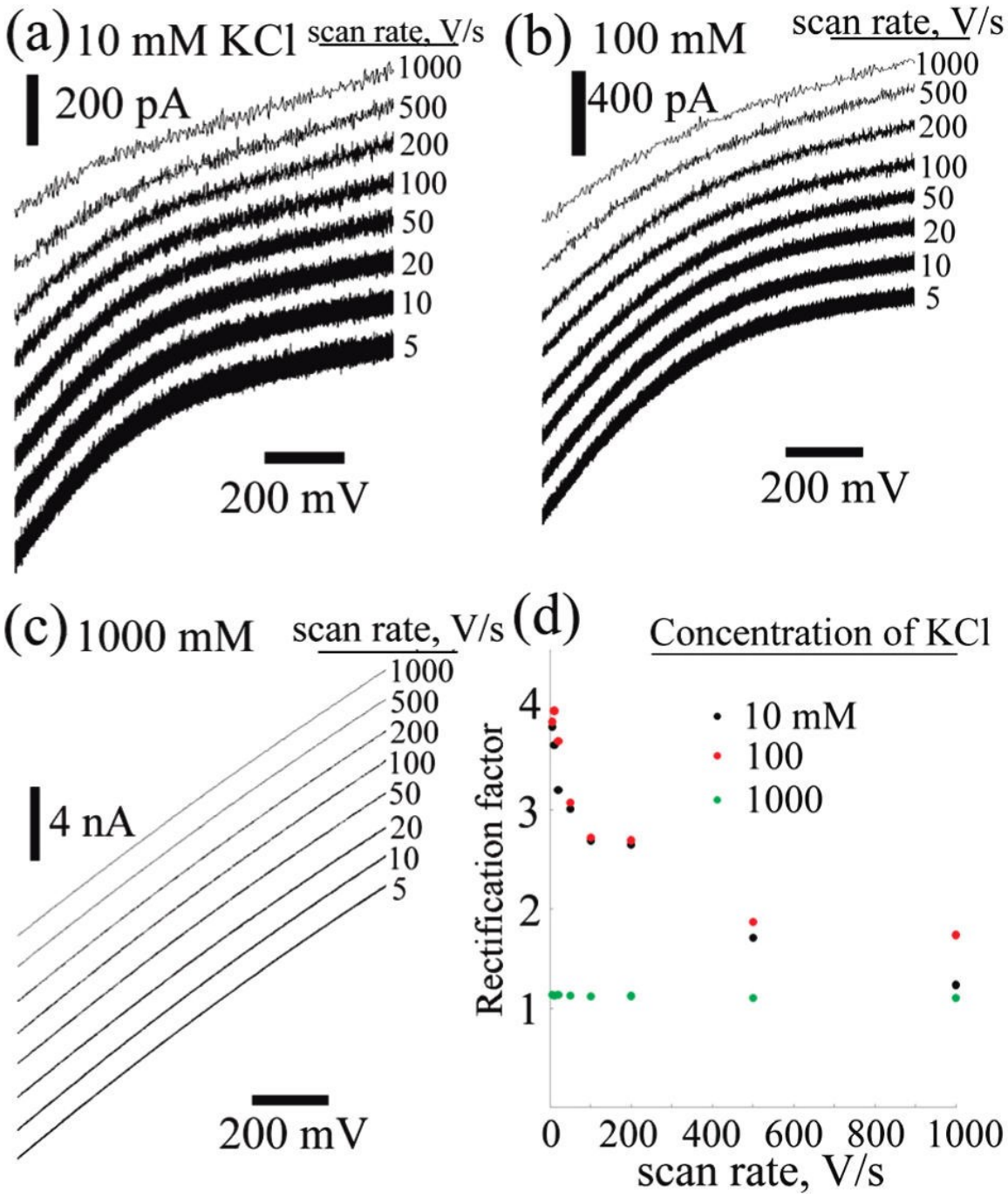

Figure 6.3 Scan-rate dependence at various KCl concentrations.
(a) – (c), scan-rate dependent *i-V* responses of a 10 nm diameter silica nanopore in (a) 0.1 mM Tris buffer (pH = 7.4) containing 10 mM KCl, (b) 1 mM Tris buffer (pH = 7.4) containing 100 mM KCl, and (c) 10 mM Tris buffer (pH = 7.4) containing 1000 mM KCl. (d) Rectification factors for (a-c) plotted as functions of the scan rate. The pore diameter was calculated from the conductance in 1M KCl assuming a half-cone angle of 5°.

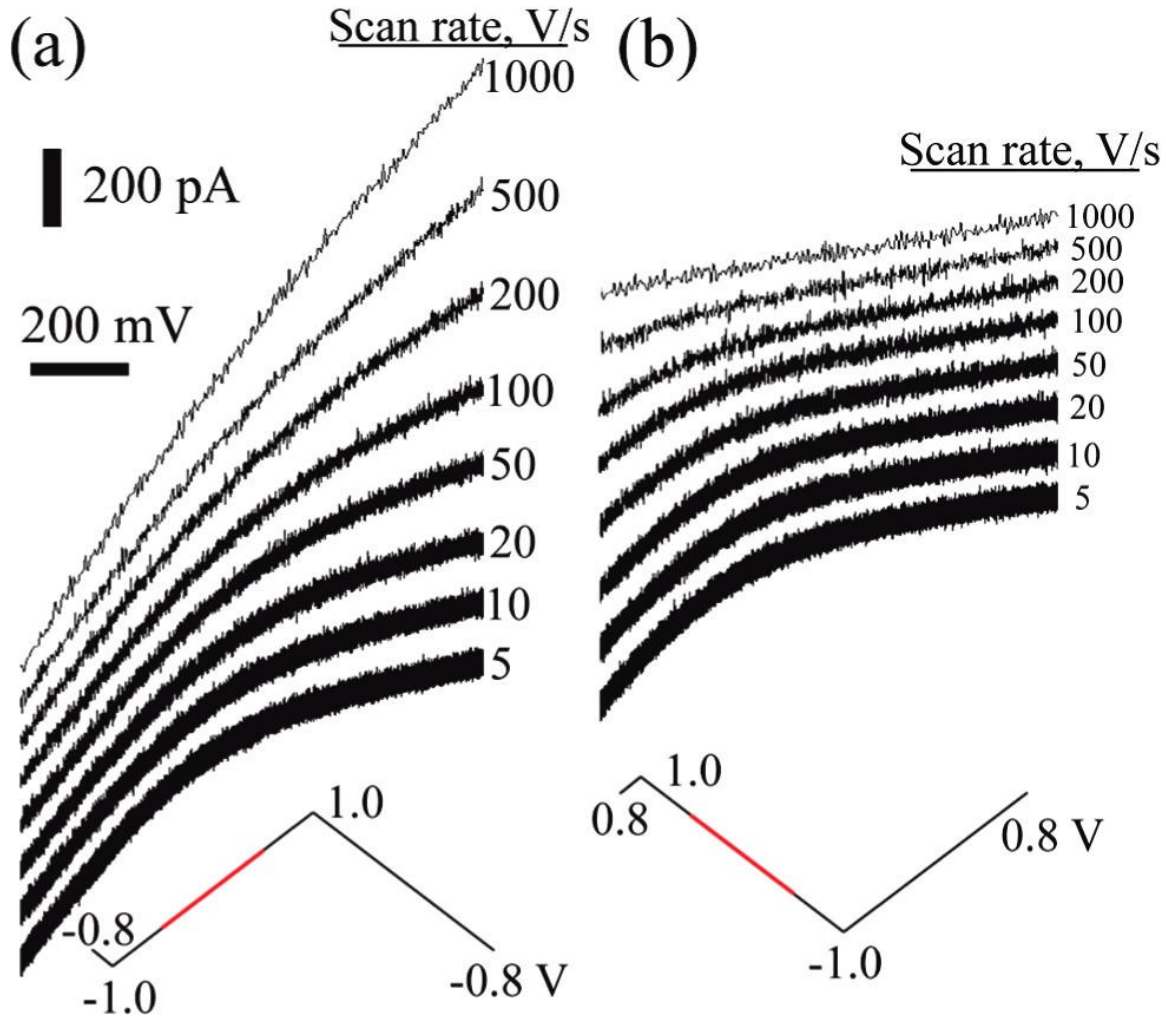

Figure 6.4 The effect of starting potential on scan-rate dependent current rectification. (a) Scan-rate dependent *i-V* responses of a 10 nm diameter silica nanopore in a 0.1 mM Tris buffer solution at pH 7.4 containing 10 mM KCl as the voltage is scanned from -0.8 V. (b) Scan-rate dependent *i-V* responses of the same nanopore in the same solution as the voltage is scanned from +0.8 V. The pore diameter was calculated from the conductance in 1M KCl assuming a half-cone angle of 5°.

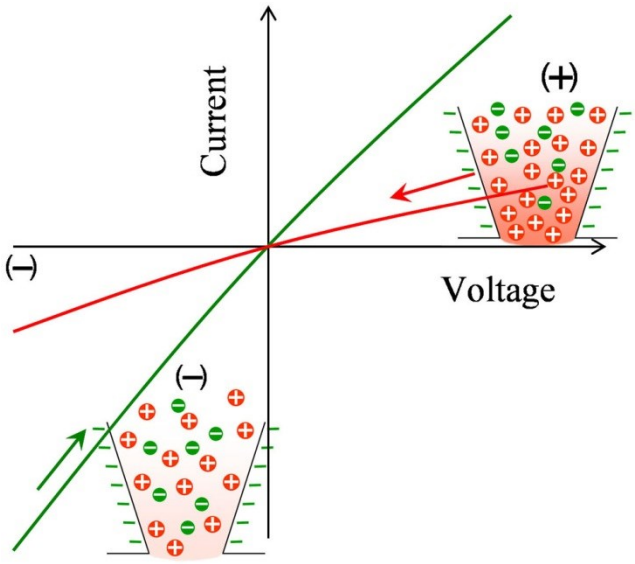

Figure 6.5 Schematic showing ionic distribution and current rectification.
Schematic illustration of the *i*-*V* responses at high scan rates when two different initial voltages are employed. Two different possible ionic distributions are shown to help explain the difference in ionic resistance.

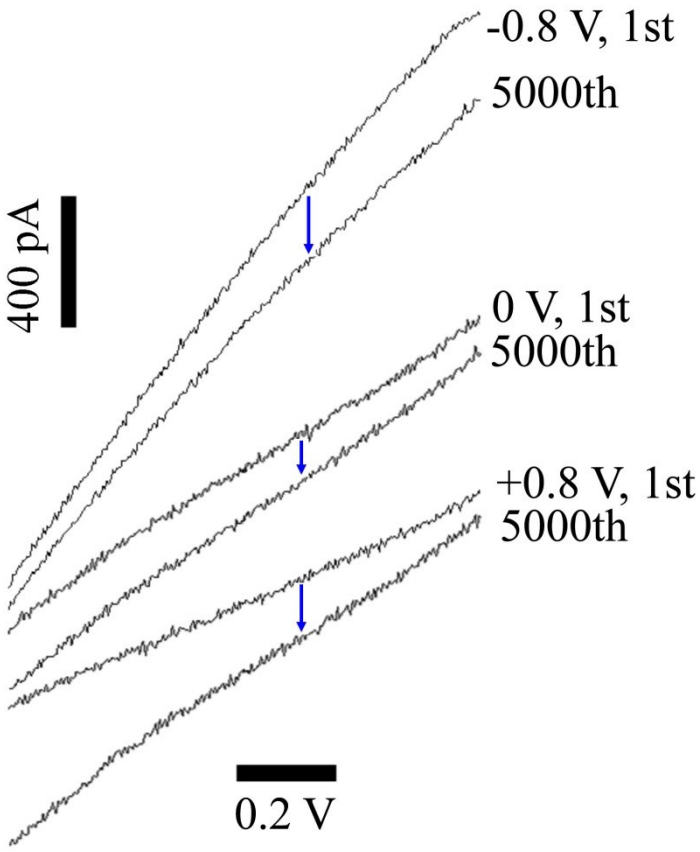

Figure 6.6 Long term *i-V* response.
A comparison of the *i-V* responses at 1000 V/s of the 1st and the 5000th scan of a 8.7 nm nanopore in a 10 mM KCl solution containing 0.1mM Tris buffer at pH 7.4 at three different starting voltages, -0.8 V, 0 V, and +0.8 V.

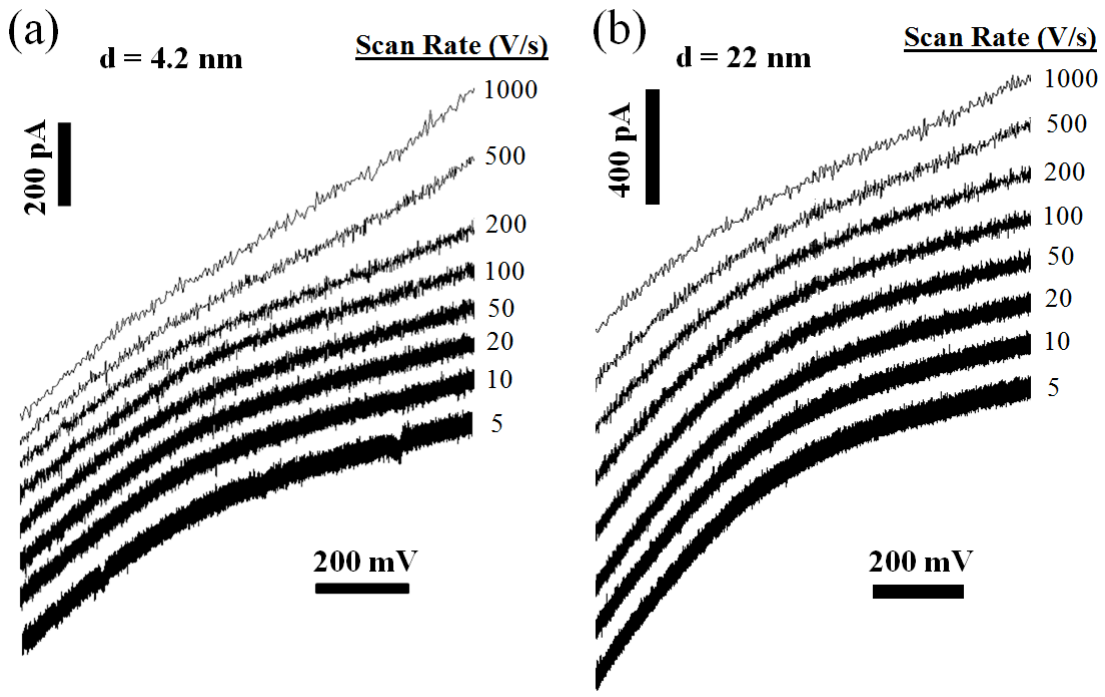

Figure 6.7 Response of different size pores.
The *i-V* responses of nanopores of two different sizes in a 10 mM KCl solution containing 0.1mM Tris buffer at pH 7.4.

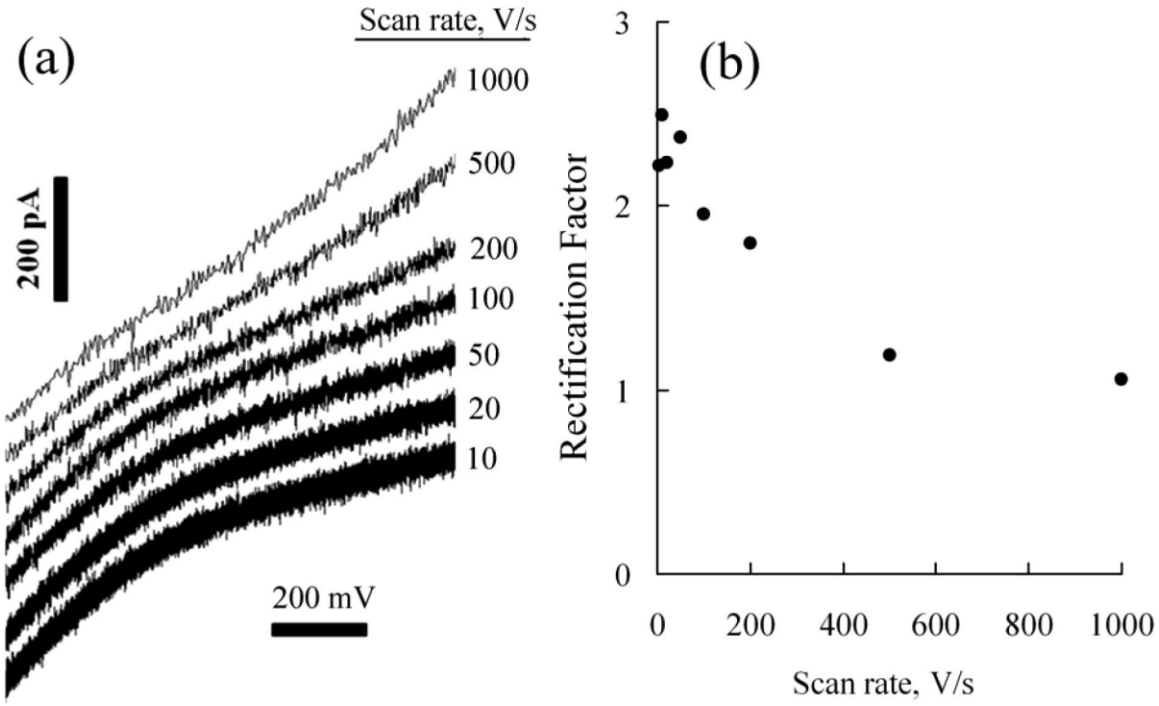

Figure 6.8 Scan-rate dependent current rectification with $CaCl_2$.
(a) Scan-rate dependent *i-V* responses of a 4.2-nm diameter silica nanopore in a 0.1mM Tris buffer solution at pH 7.4 containing 10 mM $CaCl_2$. (b) Rectification factor in (a) plotted as a function of the scan rate. The pore diameter was calculated from the conductance in 1M KCl assuming a half-cone angle of 5°.

6.6 References

(1) Wei, C.; Bard, A. J.; Feldberg, S. W. *Anal. Chem.* **1997,** *69*, 4627-4633.

(2) Siwy, Z.; Heins, E.; Harrell, C. C.; Kohli, P.; Martin, C. R. *J. Am. Chem. Soc.,* **2004**, *126*, 10580-10581.

(3) Siwy, Z. S. *Adv. Funct. Mater.,* **2006**, *16*, 735-746.

(4) White, H. S.; Bund, A. *Langmuir*, **2008**, *24*, 2212-2218.

(5) Jin, P.; Mukaibo, H.; Horne, L. P.; Bishop, G. W.; Martin, C. R. *J. Am. Chem. Soc.* **2010**, *132*, 2118-2119.

(6) Kovarik, M. L.; Zhou, K.; Jacobson, S. C. *J. Phys. Chem. B.* **2009**, *113*, 15960-15966.

(7) Woermann, D. *Phys. Chem. Chem. Phys.* **2003**, *5*, 1853-1858.

(8) Cervera, J.; Schiedt, B.; Ramirez, P. *Europhys. Lett.* **2005**, *71*, 35-41.

(9) Rischel, C.; Flyvbjerg, H.; *Phys. Rev. Lett.* **2003**, *91*, 179801.

(10) Fu, Y. Q.; Tokuhisa, H.; Baker, L. A. *Chem. Commun.* **2009**, *32*, 4877-4879.

(11) Zhang, B.; Galusha, J.; Shiozawa, P. G.; Wang, G.; Bergren, A. J.; Jones, R. M.; White, R. J.; Ervin, E. N.; Cauley, C. C.; White, H. S. *Anal. Chem.* **2007**, *79*, 4778-4787.

(12) Bard, A. J.; Faulkner, L. R. *Electrochemical Methods*, 2nd ed.; John Wiley & Sons: New York, **2001.**

(13) Clarke, R. W.; White, S. S.; Zhou, D. J.; Ying, L. M.; Klenerman, D. *Angew. Chem. Int. Ed.* **2005**, *44*, 3747 –3750.

(14) Calander, N. *Anal. Chem.* **2009**, *81*, 8347–8353.

(15) Wang, Y. C.; Stevens, A. L.; Han, J. Y. *Anal. Chem.* **2005**, *77*, 4293-4299.

(16) Snijder, E. D.; te Riele, M. J. M.; Versteeg, G. F.; van Swaaij, W. P. M. *J. Chem. Eng. Data* **1993**, *38*, 475-480.

(17) Zhang, B.; Zhang, Y. H.; White, H. S. *Anal. Chem.* **2004**, *76*, 6229-6238.

Bibliography

Adams, K. L.; Jena, B. K.; Percival, S. J.; Zhang, B. *Anal. Chem.* **2011**, *83*, 920–927.

Adams, K. L.; Puchades, M.; Ewing, A. G. *Annu. Rev. Anal. Chem.* **2008**, *1*, 329–355.

Aguilar, Z. P.; Vandaveer, W. R.; Fritsch, I. *Anal. Chem.* **2002,** *74*, 3321-3329.

Amatore, C.; Arbault, S.; Bouret, Y.; Guille, M.; Lemaitre, F.; Verchier, Y. *Anal. Chem.* **2009**, *81*, 3087– 3093

Amemiya, S., Bard, A.J., Fan, F.-R.F., Mirkin, M.V.; Unwin, P.R. *Annu.Rev. Anal. Chem.* **2008,** *1,* 95-131.

Anicet, N.; Bourdillon, C.; Moiroux, J.; and Saveant, J-M. *J. Phys. Chem. B* **1998,** *102*, 9844–9849.

Arora, A.; Eijkel, J. C. T.; Morf, W. E.; Manz, A. *Anal. Chem.* **2001,** *73*, 3282-3288.

Bard, A. J. *J. Am. Chem. Soc.* **2010**, *132*, 7559-7567.

Bard, A. J.; Fan, F. R. F.; Kwak, J.; Lev, O. *Anal. Chem.* **1989,** *61,* 131-138.

Bard, A. J.; Faulkner, L. R. *Electrochemical Methods*. 2nd ed.; John Wiley & Sons: New York, 2001.

Bard, A. J.; Li, X.; Zhan, W. *Biosens. & Bioelectron.* **2006**, *22*, 461-472.

Bard, A. J.; Zoski, C. G. *Anal. Chem.* **2000**, *72*, 346A-352A.

Basame, S. B.; White, H. S. *Anal. Chem.* **1999**, *71*, 3166-3170.

Bond, A. M.; Henderson, T. L. E.; Mann, D. R.; Mann, T. F.; Thormann, W.; and Zoski, C. G. *Anal. Chem.* **1988**, *60*, 1878-1882.

Bruns, D. *Methods* **2004**, *33*, 312-321.

Cadle, S. H.; Bruckenstein, S. *Anal. Chem.* **1974,** *46,* 16-20.

Caston, S. L.; McCarley, R. L. *J. Electroanal. Chem.* **2002**, *529*, 124-134.

Chang, B. Y.; Mavre, F.; Chow, K. F.; Crooks, J. A.; Crooks, R. M. *Anal. Chem.* **2010,** *82*, 5317-5322.

Chow, K. F.; Chang, B. Y.; Zaccheo, B. A.; Mavre, F.; Crooks, R. M. *J. Am. Chem. Soc.* **2010,** *132*, 9228-9229.

Chow, K. F.; Mavre, F.; Crooks, R. M. *J. Am. Chem. Soc.* **2008,** *130*, 7544-7545.

Comstock, D. J.; Elam, J. W.; Pellin, M. J.; Hersam, M. C. *Anal. Chem.* **2010**, *82*, 1270-1276.

Cortes-Salazar, F.; Momotenko, D.; Lesch, A.; Wittstock, G.; Girault, H. H. *Anal. Chem.* **2010**, *82*, 10037-10044.

Coulter, W. H. US Patent #2,656,508 **1953**.

Cox, J. T.; Guerrette, J. P.; Zhang, B. *Anal. Chem*. **2012**, *84*, 8797-8804.

Cox, J. T.; Zhang, B. *Annu. Rev. Anal. Chem.* **2012**, *5,* 253-272.

Damjanovic, A.; Hudson, P. G., *J. Electrochem. Soc.* **1988,** *135*, 2269-2273.

Davies, T. J.; Hyde, M. E.; Compton, R. G. *Angew. Chem. Int. Ed.* **2005**, *44*, 5121-5126.

Dhopeshwarkar, R.; Hlushkou, D.; Nguyen, M.; Tallarek, U.; and Crooks, R. M. *J. Am.*

Chem. Soc. **2008**, *130*, 10480–10481.

Eckhard, K., Chen, X., Turcu, F.; Schuhmann, W. *Phys. Chem. Chem. Phys.* **2006,** *8,* 5359-5365.

Fernandez, J. L.; Walsh, D. A.; Bard, A. J. *J. Am. Chem. Soc.* **2005**, *127*, 357-365.

Foley, K. J.; Shan, X.; Tao, N. J. *Anal. Chem.* **2008**, *80*, 5146-5151.

Fosdick, S. E.; Crooks, R. M. *J. Am. Chem. Soc.* **2012**, *134*, 863-866.

Friend, J. A. N.; Smirles, W. N. *J. Chem. Soc*. **1928**, 2242–2245.

Gardner, C. E.; Macpherson, J. V. *Anal. Chem.* **2002**, *74*, 576A-584A.

Ge, S.; White, G. J.; Haynes, C. L. *Anal. Chem.* **2009**, *81*, 2935-2943.

Gesquiere, A. J.; Park, S. J.; Barbara, P. F., *J. Phys. Chem. B* **2004**, *108,* 10301-10308.

Graham, M. D. *J. Lab Autom.* **2003**, *8*, 72–81.

Guerrette, J. P.; Oja, S. M.; Zhang, B. *Anal.Chem.,* **2012**, *84*, 1609-1616.

Guerrette, J. P.; Percival, S. P.; Zhang, B. *J. Am. Chem. Soc.* **2013**, *135*, 855-861.

Guerrette, J. P.; Percival, S. P.; Zhang, B. *Langmuir* **2011**, *27*, 12218-12225.

Guerrette, J. P.; Zhang, B. *J. Am. Chem. Soc.* **2010**, *132*, 17088-17091.

Han, K. S.; Liu, G. K.; Zhou, X. C.; Medina, R. E.; Chen, P. *Nano Lett.* **2012**, *12*, 1253-1259.

Heien, M.; Johnson, M.; Wightman, R. *Anal. Chem.* **2004**, *76*, 5697–5704.

Henry, C. S.; Fritsch, I. *J. Electrochem. Soc.* **1999**, *146*, 3367-3373.

Hickling, A. *Trans. Faraday Soc.* **1942**, 38, 27-33.

Hiddleston, J. N.; Douglas, A. F. *Nature* **1968**, *218*, 601–602.

Hlushkou, D., Perdue, R. K., Dhopeshwarkar, R., Crooks, R. M., and Tallarek, U. *Lab on a Chip* **2009**, *9*, 1903–1913.

Hotta, H.; Akagi, N.; Sugihara, T.; Ichikawa, S.; Osakai, T. *Electrochem. Comm.* **2002,** *4*, 472-477.

Hsieh, S.; Jorgenson, J.W. *Anal. Chem.* **1996**, *68,* 1212–1217.

Huffman, M. L.; Venton, B. J. *Analyst* **2009**, *134*, 18–24.

Ikeuchi, H.; Hayafuji, M.; Aketagawa, Y.; Taki, J.; Sato, G. P., *J. Electroanal. Chem.* **1995**, *396*, 553-556.

Jin, P.; Mukaibo, H.; Horne, L. P.; Bishop, G. W.; Martin, C. R. *J. Am. Chem. Soc.* **2010**, *132*, 2118-2119.

Kazdobin, K.; Shvab, N.; Tsapakh, S. *Chem. Eng. J.* **2000**, *79*, 203–209.

Keithley, R. B.; Carelli, R. M.; and Wightman, R. M. *Anal. Chem.* **2010**, *82*, 5541-5551.

Kim, Y. T.; Scarnulis, D. M.; and Ewing, A. G. *Anal. Chem.* **1986**, *58*, 1782-1786.

Klett, O.; and Nyholm, L. *Anal. Chem.* **2003**, *75*, 1245–1250.

Kovach, P. M.; Caudill, W. L.; Peters, D. G.; Wightman, R. M. *J. Electroanal. Chem.* **1985**, *185*, 285-295.

Kurulugama, R. T.; Wipf, D. O.; Takacs, S. A.; Pongmayteegul, S.; Garris, P. A.; Baur, J. E. *Anal. Chem.* **2005**, *77*, 1111-1117.

Lanyon, Y. H.; Arrigan, D. W. M. *Sens. Actuators B* **2007**, *121*, 341-347.

Laws, D. R.; Hlushkou, D.; Perdue, R. K.; Tallarek, U.; and Crooks, R. M. *Anal. Chem.* **2009**, *81*, 8923–8929.

Lee, C. Y.; Tan, Y. J.; Bond, A. M. *Anal. Chem.* **2008**, *80*, 3873-3881.

Lei, C.; Hu, D.; Ackerman, E. J. *Chem. Commun.* **2008**, 5490-5492.

Lescha, A.; Momotenkob, D.; Cortés-Salazarb, F.; Wirthc, I.; Tefashea, U. M.; Meinersa, F.; Vaskea, F.; Giraultb, H. H.; Wittstock. G. *J. Electroanal. Chem.* **2012**, *666*, 52-61.

Li, Y. X.; Ito, T. *Anal. Chem.* **2009**, *81*, 851-855.

Li, Y.; Bergman, D.; Zhang, B. *Anal. Chem.* **2009**, *81*, 5496– 5502.

Li, Y.; Cox, J. T.; and Zhang, B. *J. Am. Chem. Soc.* **2010**, *132*, 3047-3052.

Lin, Y.; Trouillon, R.; Svensson, M. I.; Keighron, J. D.; Cans, A-S.; Ewing, A. G. *Anal. Chem.* **2012**, *84*, 2949-2954.

Liu, H. Y.; Fan, F. R. F.; Bard, A. J. *J. Electrochem. Soc.* **1985**, *132*, 2666-2668.

Loget, G.; Kuhn, A. *Anal. Bioanal.Chem.* **2011,** *400,* 1691-1704.

Macpherson, J. V., Jones, C. E.; Unwin, P. R. *J. Phys. Chem. B* **1998**, *102*, 9891-9897.

Maeda, M.; White, H. S.; McClure, D. J. *J. Electroanal. Chem.* **1986**, *200*, 383-387.

Mavre, F.; Anand, R. K.; Laws, D. R.; Chow, K. F.; Chang, B. Y.; Crooks, J. A.; Crooks, R. M. *Anal.Chem.* **2010,** *82*, 8766-8774.

Mavre, F.; Chow, K. F.; Sheridan, E.; Chang, B. Y.; Crooks, J. A.; Crooks, R. M. *Anal. Chem.* **2009,** *81*, 6218-6225.

McKelvey, K.; Snowden, M. E.; Peruffo, M.; Unwin, P. R. *Anal. Chem.* **2011**, *83*, 6447-6454.

Menke, E. J.; Thompson, M. A.; Xiang, C.; Yang, L. C.; Penner, R. M. *Nat. Mater.* **2006,** *5*, 914-919.

Morris, C. A.; Friedman, A. K.; Baker, L. A. *Analyst* **2010**, 135, 2190-2202.

Morris, R. B.; Franta, D. J.; White, H. S. *J. Phys. Chem.* **1987**, *91*, 3559-3564.

Nagale, M. P.; Fritsch, I. *Anal. Chem.* **1998,** *70*, 2902-2907.

Nagale, M. P.; Fritsch, I. *Anal. Chem.* **1998,** *70*, 2908-2913.

Ndungu, P. G. Ph.D. Thesis, Drexel University, Philadelphia, PA, 2004.

Oja, S. M.; Wood, M.; Zhang, B. *Anal. Chem.* **2013**, *85*, 473-476.

Ordeig, O.; Godino, N.; del Campo, J.; Munoz, F. X.; Nikolajeff, F.; and Nyholm, L. *Anal. Chem.* **2008**, *80*, 3622–3632.

Palacios, R. E.; Fan, F. R. F.; Bard, A. J.; Barbara, P. F., *J. Am. Chem. Soc.* **2006**, *128*, 9028-9029.

Palacios, R. E.; Fan, F. R. F.; Grey, J. K.; Suk, J.; Bard, A. J.; Barbara, P. F., *Nature Mater.* **2007**, *6*, 680-685.

Perdue, R. K.; Laws, D. R.; Hlushkou, D.; Tallarek, U.; Crooks, R. M. *Anal. Chem.* **2009,** *81*, 10149-10155.

Plana, D.; Jones, F. G. E.; Dryfe, R. A. W. *J. Electroanal. Chem.* **2010,** *646*, 107-113

Plana, D.; Shul, G.; Stephenson, M. J.; Dryfe, R. A. W. *Electrochem. Comm.* **2009,** *11*, 61-64.

Rubinstein, J. T.; Spelman, F. A.; Soma, M.; Suesserman, M. F. *IEEE Trans. Biomed. Eng.***1987,** *34*, 864-875.

Saito, Y. *Rev. Polarogr*. **1968**, *15*, 177-182.

Samuelsson, M.; Armgarth, M.; Nylander, C. *Anal. Chem.* **1991**, *63*, 931-936.

Sanchez-Sanchez, C. M.; Bard, A. J. *Anal. Chem.* **2009**, *81*, 8094-8100.

Schulte, A.; Nebel, M.; Schuhmann, W. *Annual Rev. Anal.Chem.* **2010,** *3*, 299-318.

Scott, E. R.; White, H. S.; Phipps, J. B. *Anal. Chem.* **1993**, *65*, 1537-1545.

Seibold, J. D.; Scott, E. R.; White, H. S. *J. Electroanal. Chem.* **1989**, *264*, 281-289.

Shan, X., Wang, S., Wang, W. & Tao, N. *Anal. Chem.,* **2011**, *83*, 7394-7399.

Shan, X.; Díez-Pérez, I.; Wang, L.; Wiktor, P.; Gu, Y.; Zhang, L.; Wang, W.; Lu, J.; Wang, S.; Gong, Q.; Li, J. H.; Tao, N. J. *Nat. Nanotech.* **2012**, *7*, 668-672.

Shan, X.; Patel, U.; Wang, S.; Iglesias, R.; Tao, N. J. *Science* **2010**, *327*, 1363-1366.

Shen, M.; Ishimatsu, R.; Kim, J. and Amemiya, S. *J. Am. Chem. Soc.* **2012**, *134*, 9856-9859.

Shiguro, Y.; Inagi, S.; Fuchigami, T. *Langmuir* **2011**, *27*, 7158–7162.

Siwy, Z. S. *Adv. Funct. Mater.* **2006**, *16*, 735-746.

Siwy, Z.; Heins, E.; Harrell, C. C.; Kohli, P.; Martin, C. R. *J. Am. Chem. Soc.* **2004**, *126*, 10580-10581.

Smotkin, E. S.; Diaz-Morales, R. R. *Annu. Rev. Mater. Res.* **2003**, *33*, 557-579.

Sombers, L. A.; Hanchar, H. J.; Colliver, T. L.; Wittenberg, N.; Cans, A.; Arbault, S.; Amatore, C.; and Ewing, A. G. *J. Neurosci.* **2004**, *24*, 303-309.

Song, C. J.; Zhang, J. *PEM Fuel Cell Electrocatalysts and Catalyst Layers Fundamentals and Applications* (Ed.) Zhang, J., **2008**, Vol. XXII.

Stackelberg, M. von; Pilgram, M.; and Toome, W. Z. *Elektrochem.* **1953**, *57*, 342-350.

Stewart, A. A.; Campbell, J. A.; Girault, H. H.; Edddowes, M. *Ber. Bunsen Phys. Chem.* **1990,** *94*, 83-87.

Sun, P. *Anal. Chem.* **2010**, *82*, 276-281.

Takahashi, Y.; Shevchuk, A. I.; Novak, P.; Murakami, Y.; Shiku, H.; Korchev, Y. E.; Matsue, T. *J. Am. Chem. Soc.* **2010**, *132*, 10118-10126.

Takmakov, P.; Zachek, M. K.; Keithley, R. B.; Walsh, P. L.; Donley, C.; McCarty, G. S.; Wightman, R. M. *Anal. Chem.* **2010**, *82*, 2020-2028.

Uitto, O. D.; White, H. S. *Anal. Chem.* **2001**, *73*, 533-539.

Ulrich, C., Andersson, O., Nyholm, L., and Björefors, F. *Anal. Chem.* **2009**, *81*, 453–459.

Wang, G. L.; Bohaty, A. K.; Zharov, I.; White, H. S. *J. Am. Chem. Soc.* **2006**, *128*, 13553-13558.

Wang, J.; Brennsteiner, A.; Sylwester, A. P.; Renschler, C. L. *Electroanalysis* **1991**, *3*, 505-509.

Wang, W.; Foley, K.; Shan, X.; Wang, S.; Eaton, S.; Nagaraj, V. J.; Wiktor, P.; Patel, U.; Tao, N. J. *Nature Chem.* **2011**, *3*, 249-253.

Wang, Y.; Hernandez, R. M.; Bartlett, D. J.; Bingham, J. M.; Kline, T. R.; Sen, A.; and Mallouk, T. E. *Langmuir* **2006**, *22*, 10451–10456.

Wanunu, M. *Phys. Life Rev.* **2012**, 9, 125–158.

Warakulwit, C.; Nguyen, T.; Majimel, J.; Delville, M. H.; Lapeyre, V.; Garrigue, P.; Ravaine, V.; Limtrakul, J.; and Kuhn, A. *Nano Lett.* **2008**, *8*, 500–504.

Watkins, J. J.; Chen, J.; White, H. S.; Abruna, H. D.; Maisonhaute, E.; Amatore, C. *Anal. Chem.* **2003**, *75*, 3962-3971.

Wehmeyer, K. R.; Deakin, M. R.; Wightman, R. M. *Anal. Chem.* **1985**, *57*, 1913-1916.

Wei, C.; Bard, A. J.; Feldberg, S. W. *Anal. Chem.* **1997**, *69*, 4627-4633.

Weiland, J. D.; Anderson, D. J.; Pogatchnik, C. C.; Boogaard, J. J. *Proc. 19th Annu. Int. Conf. IEEE EMBS* **1997**, 2273–2276.

White, H. S.; Bund, A. *Langmuir* **2008**, *24*, 2212-2218.

Xiang, C. X.; Kung, S. C.; Taggart, D. K.; Yang, F.; Thompson, M. A.; Guell, A. G.; Yang, Y. A.; Penner, R. M. *ACS Nano* **2008**, *2*, 1939-1949.

Xu, W.; Kong, J. S.; Yeh, Y. T. E.; Chen, P. *Nature Mater.* **2008**, *7*, 992-996.

Xu, W.; Shen, H.; Kim, Y. J.; Zhou, X. C.; Liu, G. K.; Park, J.; Chen, P., *Nano Lett.* **2009**, *9*, 3968-3973.

Zhan, W.; Alvarez, J.; and Crooks, R. M. *J. Am. Chem. Soc.* **2002**, *124*, 13265–13270.

Zhang, B.; Adams, K. L.; Luber, S. J.; Eves, S. J.; Heien, M. L.; Ewing, A. G. *Anal. Chem.* **2008**, *80*, 1394-1400.

Zhang, B.; Galusha, J.; Shiozawa, P. G.; Wang, G. L.; Bergren, A. J.; Jones, R. M.; White, R. J.; Ervin, E. N.; Cauley, C. C.; White, H. S. *Anal. Chem.* **2007**, *79*, 4778-4787.

Zhang, B.; Heien, M. L. A. V.; Santillo, M. F.; Mellander, L.; Ewing, A. G. *Anal. Chem.* **2011**, *83*, 571-577.

Zhang, B.; Zhang, Y. H.; White, H. S. *Anal. Chem.* **2006**, *78*, 477-483.

Zhang, B.; Zhang, Y. H.; White, H. S. *Anal. Chem.* **2004**, *76*, 6229-6238.

Zoski, C. G.; Fernandez, J. L.; Imaduwage, K.; Gunasekara, D.; Vadari, R., *J. Electroanal. Chem.* **2011,** *651*, 80-93.

Vita

Joshua Pierre Guerrette was born and raised in Auburn, NY. After high school Josh joined the US Army and was stationed at Fort Bragg, NC in the 82nd Airborne Division as an infantry paratrooper deploying to Kosovo and Albania in 1999. While in NC Josh fell in love with and married Jinger Sara Thies. The two of them moved to NY in 2000 where Josh attended Cayuga Community College and continued to serve, this time in the NY Army National Guard. After graduating magna cum laude with an A.S. in liberal arts and science Josh was hired as a firefighter/EMT with Auburn Fire Department and subsequently attended the New York State Academy of Fire Science. Although Josh found his career as a firefighter to be very rewarding, several factors including the desire to continue his education led Josh and Jinger to move to Honolulu, HI. There Josh finished his undergraduate degree at the University of Hawai`i at Manoa earning a B.S. in chemistry with a 4.0 GPA. Next up was graduate school at the University of Washington, Seattle. Since 2009 Josh has worked in the research group of Prof Bo Zhang studying electroanalytical chemistry. This dissertation covers most of those missing years.